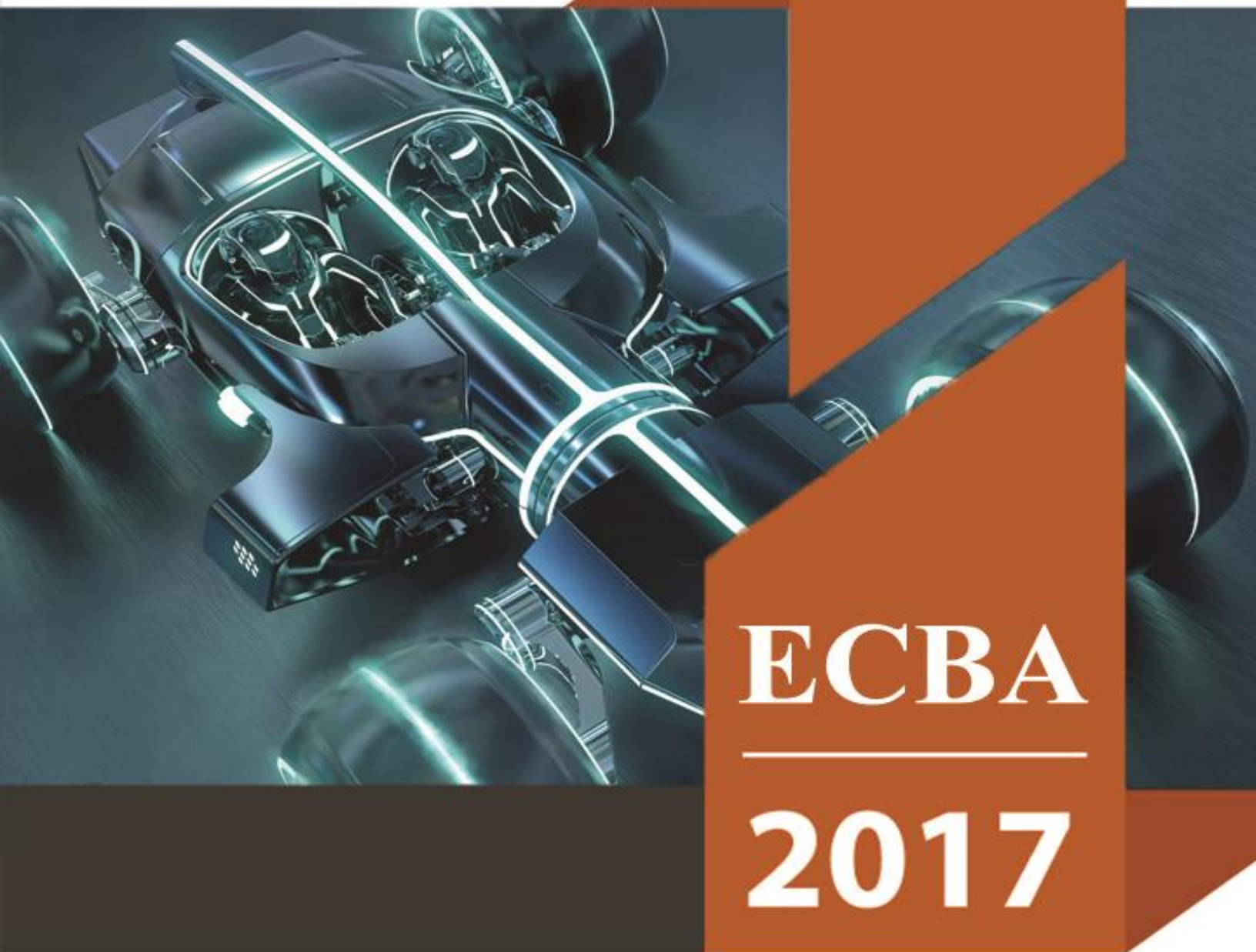




Volume 402, Issue 01



ECBA

2017

January 20-21, 2017

Macao, China

CONFERENCE
PROCEEDINGS

BOOK OF FULL PAPERS

ECBA-2017

**International Conference on
“Engineering & Technology, Computer, Basics & Applied Sciences”
(ECBA-2017), Macao, China**

Book of Full Paper Proceedings
International Conference on
“ENGINEERING & TECHNOLOGY, COMPUTER, BASICS & APPLIED
SCIENCES
(ECBA-2017)
Macao, China

Office Address:

M2-17-01 Tower 2, Level 17 8trium

Bandar Sri Damansara,

52200 Kuala Lumpur, Malaysia

CONTACT: (+6) 03 6735 6566

EMAIL: contact@academicfora.com

All rights reserved. No part of this publication may be reproduced, stored in a retrieval system, or transmitted in any form or by any means, electronic, mechanical, photocopying, recording or otherwise, without the prior written permission of the publisher. Applications for the copyright holder's written permission to produce any part of this publication should be addressed to the publisher.

Proceedings of the International Conference on
**“Engineering & Technology, Computer, Basics & Applied Sciences
(ECBA-2017)”**

ISBN: 978-969-683-188-4

Disclaimer

Every reasonable effort has been made to ensure that the material in this book is true, correct, complete, and appropriate at the time of writing. Nevertheless the publishers, the editors, and the authors do not accept responsibility for any omission or error, or for any injury, damage, loss, or financial consequences arising from the use of the book. The views expressed by the contributors do not necessarily reflect those of the Academic Fora.

Conference Review Board

Academic Fora

Engineering & Applied Sciences Review Board

1. D Makovicka, Czech Technical University in Prague, Czech Republic
2. M Phocas, University of Cyprus, Cyprus
3. M C Porcu, University of Cagliari, Italy
4. A D Tsonos, Aristotle University of Thessaloniki, Greece
5. Wahiba Ben Abdesslem, High Institute of Management of Tunis, Tunisia
5. Hafez Fouad, Electronics Research Institute, Egypt
6. Hong Yu, Capitol Technology University, USA
7. Bela Genge, Petru Maior University, Romania
8. David Wyld, Southeastern Louisiana University, USA
9. Jacques Demerjian, Lebanese University, Lebanon
10. Tran Dinh Que, Post and Telecommunication Institute of Technology (PTIT), Vietnam
11. Wu Deng, Dalian Jiaotong University, China
12. Zonggdeng, Qufu Normal University, China
13. Joey Wu, University of Pretoria, South Africa
14. Jasrul Nizam Ghazali, MARA University of Technology
15. B. Kannan, Cochin University of science and technology
16. Prof. Michel Plaisent, GSMI Fellow, University of Quebec in Montreal, Canada
17. Dr. Joseph Ofori Dankwa, GSMI Fellow, Saginaw Valley State University, USA
18. Dr. Abdullah Aldakhil, GSMI Fellow, King Saud University, Saudi Arabia
19. Dr. Stephen Wayne Pilgrim, University of the West Indies, Barbados, West Indies
20. Dr. Aye Mengistu Alemu, SolBridge International School of Business, South Korea
21. Dr. Mukhtar Halliru, GSMI Fellow, Bayero University Kano, Nigeria
22. Prof. P.S. P. Swamy, GSMI Fellow, Bangalore University, India
23. Dr. Ali Serhan Koyuncugil, Capital Markets Board of Turkey, Turkey
24. Dr. Faisal B. Al-khateeb, New York Institutes of Technology-Abu Dhabi Campus, UAE
25. Dr. Samuel Andoh, Southern Connecticut State University, USA
26. Dr. Anli Suresh, Madras Christian College, India
27. Dr. Hasan Bulent Kantarci, Kocaeli University, Turkey
28. Amar Faiz Bin Zainal Abidin, University Of Burgundy, Malaysia
29. Dr. Balhassn SM Ali, Department of Mechanical Engineering, Bursa Orhangazi University, Turkey
30. Dr. Shahed Mohammadi Dehnavi, Head of Biometric Identification Research team, Registration center, Ministry of Interior, Tehran, Iran
31. Dr. Moneruzzaman Khandaker, Senior Lecturer UniSZA, Malaysia, Terengganu
32. Ali Sarrafi Nik, PhD- Architect, Islamic Azad University Tabriz, Iran

International Conference on
“Engineering and Technology, Computer, Basics and Applied Sciences
Macao, China”

Venue: Grandview Hotel Macau, China

ORGANIZING COMMITTEE

1. Ms. Grace Ooi

Program Coordinator

Email: grace@academicfora.com

2. Mr. Metin Gurani

Conference coordinator

Email: metingurani@academicfora.com

3. Mr. Metha Shahi

Conference coordinator

Email: Metha@academicfora.com

4. Ms. Petrel Qiu

Conference coordinator

Email: Petrel@academicfora.com

CONFERENCE CHAIR MESSAGE

Dr. Malika Ait Nasser

International Conference on “Engineering & Technology, Computer, Basic & Applied Sciences” serves as platform that aims to help the scholarly community across nations to explore the critical role of multidisciplinary innovations for sustainability and growth of human societies. This conference provides opportunity to the academicians, practitioners, scientists, and scholars from across various disciplines to discuss avenues for interdisciplinary innovations and identify effective ways to address the challenges faced by our societies globally. The research ideas and studies that we received for this conference are very promising, unique, and impactful. I believe these studies have the potential to address key challenges in various sub-domains of social sciences and applied sciences.

I am really thankful to our honorable scientific and review committee for spending much of their time in reviewing the papers for this event. I am also thankful to all the participants for being here with us to create an environment of knowledge sharing and learning. We the scholars of this world belong to the elite educated class of this society and we owe a lot to return back to this society. Let's break all the discriminating barriers and get free from all minor affiliations. Let's contribute even a little or single step for betterment of society and welfare of humanity to bring prosperity, peace and harmony in this world. Stay blessed.

Thank you.

Malika Ait Nasser

Conference Chair

Email: Chair2017@academicfora.com

ECBA-2017

CONTENTS

Articles

Effect of Electrostatic Voltage on NOx Emission from Propane Diffusion Flame	1
S.M.Kim, B.V.S.Jyoti, SeungWook Baek, Young Chul Ghim, Dimitrios. C. Kyritsis	
Operation Strategy of Jeju Power System by using Frequency Regulation Energy Storage System	7
Seong Hoon Lee, Sang Heon Chae, Ngoc-Thanh Quach, Eel-Hwan Kim, Ho Chan Kim	
A Study on Operation of Home ESS under Fault Condition	20
Gi Hoon Kim, Ngoc-Thanh Quach, Sang Heon Chae, Eel-Hwan Kim, And Seong Bo Oh	
Analyzing the Effect of Offshore Wind Farm to Onshore Power Grid based on MMC-HVDC System	27
Min Hyeok Kang, Ngoc-Thanh Quach, Sang Heon Chae, Young Gyu Jin, Eel-Hwan Kim	
Status of High Temperature Superconducting Motor for Electric Ship Propulsion	35
Jae Hyung Moon, Chang Ju Hyeon, Seho Kim, Ho Min Kim	
The Plan and the Present Status Constructing Chargers to Promote Ev Penetration in the Jeju Island	42
Hee-Jeong Ko, Su-Wan Kim, Ankhzayabaatarbileg, Kyu-Ho Park, Hoonkwon, Gae-Myoung Lee	
Status of High Temperature Superconducting Motor for Electric Vehicles Propulsions	47
Kyu Seong Song, Ji Hyung Kim, Ho Min Kim, Se Ho Kim	
Contributiveness of PV Plants on Electric Power during Sumer Peak Times in the Jeju Island	55
Suk-Young Ko, Su-Wan Kim, Ankhzaya Baatarbileg, Gae-Myoung Lee	
Power Generation Characteristics of MW Photovoltaic Power Plants in the Jeju Island	62
Hyeon-seong Yoon, Seung-beom Kim, Su-wan Kim, Ankhzaya Baatarbileg, Hoon Kwon, Gae-myung Lee	
An Experimental Study on the Mechanical Properties of Lightweight Aggregate Concrete Using Ultra High Performance Concrete and Expanded Polystyrene Beads	69

Yujin Ha, Sung-gul Hong	
Punching Shear Strengthening of RC Interior Flat Plate-Column Connections with UHPFRC Overlay on Concentric Loading	73
Hyunsoo Youn, Sunggul Hong	
RC Column Retrofit with Ultra High Performance Concrete	81
In Yeong Koo	
Analysis of the PV Module's Output According to Cloud Moving	86
Ankhzaya Baatarbileg, Su-wan Kim, Gae-myoung Lee	

ECBA-17

Effect of Electrostatic Voltage on NOx Emission from Propane Diffusion Flame

S.M.Kim¹, B.V.S.Jyoti², SeungWook Baek^{3*}, Young Chul Ghim⁴, Dimitrios. C. Kyritsis⁵

^{1,2,3,4}KAIST, Daejeon, South Korea

⁵KHALIFA University, Abu Dhabi, UAE

Abstract

The effect of the DC electric field on the diffusion swirling flame was investigated experimentally on NOx formation. It was observed that with increase in voltage, change in polarity, and electrode position (radial and axial position) flame profile changes as a result considerable effect on NOx emission. The result showed that the applied electric field reduced the flame temperature, and thereby lowering thermal NOx formation is obtained. For both the polarities and electrode position, NOx (ppm) formation recorded for lean mixture is decreasing and quite low at higher applied voltage. The minimum NOx recorded was between 28 to 26 ppm (for axial electrode) and 26 to 18 ppm (for radial electrode) at 2kV and the percent reduction in NOx was around 24 ~ 48%.

© 2017 The Authors. Published by Academic Fora. This is an open access article under the CC BY-NC-ND license (<http://creativecommons.org/licenses/by-nc-nd/4.0/>)

Peer-review under responsibility of the Scientific & Review committee of ECBA- 2017.

Keywords— Voltage, Temperature, NOx emission, Combustor, Polarity

Introduction

Research on the combustion behavior in the field of science, technology and engineering continues to the present. Recently, the effect of the electric field on the combustion phenomenon has also become an issue [1-4]. The NOx generation in the combustion is a problem that must be considered. Generally, there are two methods for NOx formation. The fuel NOx and the thermal NOx. The fuel NOx is produced by the reaction between hydrocarbon radicals and nitrogen contained in the fuel generate fuel NOx. Fuel NOx levels are high in coal and mineral oil combustion. The thermal NOx is produced when a fuel burns at a high temperature, atmospheric nitrogen reacts with the dissociated oxygen. So when the flame temperature is low, the NOx generation is reduced.

Varying the applied voltage and polarity to the electrode in the flame, a variation of flame temperature and NOx emission can be obtained. Furthermore, electrically controlled combustion can help to make a air-fuel mixture and can spread out a flame [1-7].

Based on these effects, in this experimental study, NOx formation of the propane diffusion flame with applying DC voltage is discussed.

Experimentation



Figure 1: Radial Electrode

*All correspondence related to this article should be directed to SeungWook Baek, KAIST, Daejeon, South Korea
Email: sm0226@kaist.ac.kr

© 2017 The Authors. Published by Academic Fora. This is an open access article under the CC BY-NC-ND license

(<http://creativecommons.org/licenses/by-nc-nd/4.0/>)

Peer-review under responsibility of the Scientific & Review committee of ECBA-2017.



Figure 2: Axial Electrode

The burner with swirl was designed for diffusion flame. The experimental setup consists of following part; fuel inlet, air inlet, swirler, opening for electrode, combustor with water cooling jacket for constant wall temperature as in Fig. 3. K type thermocouples were used for temperature profile study along the combustor height with bead dia. 1.5mm. Thermocouple was calibrated before performing the experiment. The diffusion flame is made from an axial propane supply of 1.25 l/min and a constant dry air supply of 40 l/min, providing lean combustion conditions at the burner outlet. For combustion study, two type of electrode was used. A radial electrode of 26.5mm in inner diameter and 3.25mm in thickness was radially inserted. A axial electrode of 3.5 mm in diameter and 415 mm in length was axially inserted. A high DC voltage source (GLASSMAN HIGH VOLTAGE INC.) provides the required voltage to the axially inserted electrode and radially. The voltage of the electrode can be varied in the range of -2 to +2 kV. The combustion products were measured using a NO_x analyzer (EUROTRON Greenline Gas analyzer).

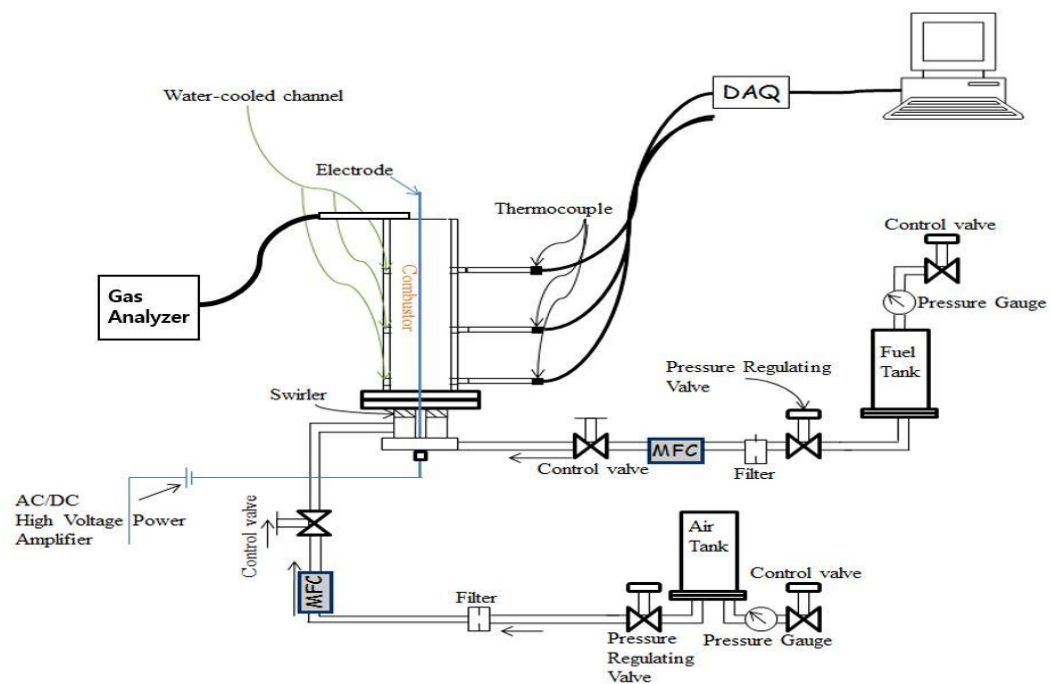


Figure 3: Experimental Setup

Result and Discussion

Temperature Profile

Temperature profile along the combustor height can be observed in figure 5 to 10 for both positive and negative polarity with varying applied voltage to both axial and radial electrode, while figure 4 gives the position of the thermocouples on the combustor.

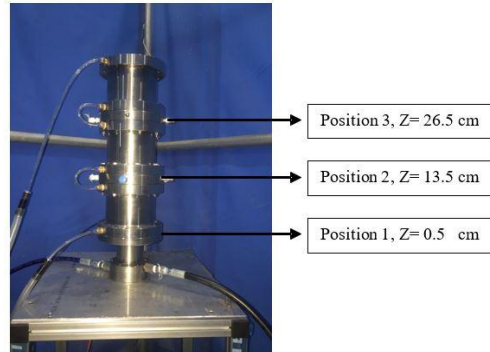


Figure 4: Positions of the Thermocouples

Axial position electrode

Positive polarity:

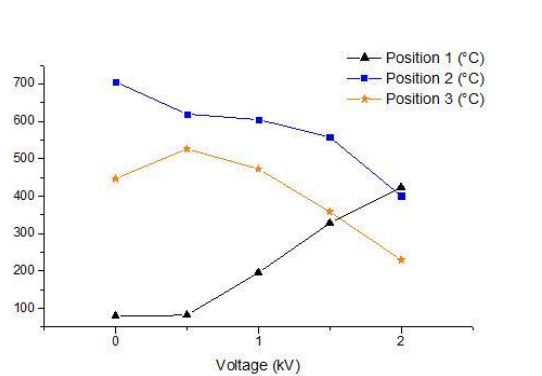


Figure 5: Temperature profile at positive polarity applied to axial position electrode

Lowest temperature profile is observed at bottom of the combustor (position 1). However, temperature is gradually increasing with applied voltage at position 1. For position 2 and 3, the temperature profile is gradually decreasing with voltage applied. The maximum temperature was recorded around 700°C at position 2 for 0kV, and 400°C at position 1 for 2kV.

Negative polarity:

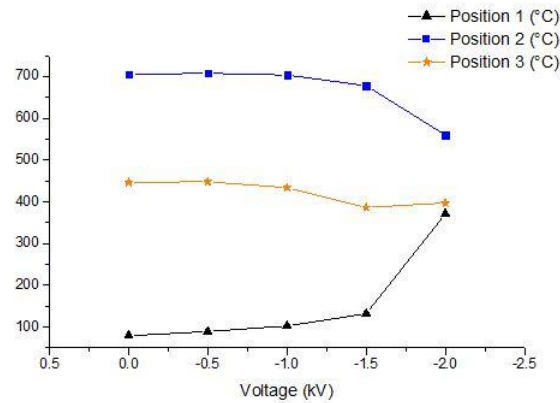


Figure 6: Temperature profile at negative polarity applied to axial position electrode

At position 1, the temperature recorded nearly constant values from 0 to -1.5kV then a rise in temperature from -1.5kV applied voltage. The maximum temperature was recorded around 700°C at position 2 for 0kV, and 600°C at position 2 for 2kV.

Radial Position Electrode Positive Polarity

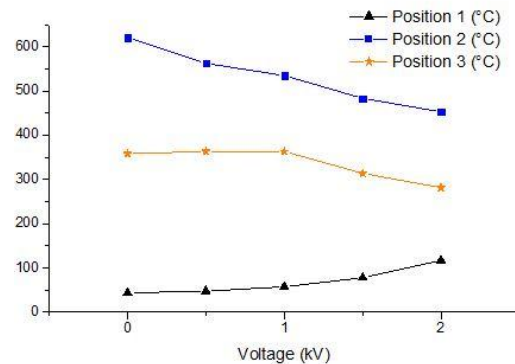


Figure 7: Temperature profile at positive polarity applied to radial position electrode

Temperature at all positions for using the radial electrode varies slowly compared with that of the axial electrode case as the voltage increases.

For this case, the flame peak temperature is around 500°C at position 2 for 2kV, but the position 1 of the combustor shows the lower temperature profile in comparison to other region of the combustor and other cases.

Negative Polarity:

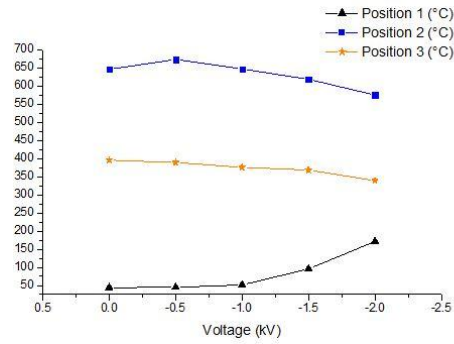


Figure 8: Temperature profile at negative polarity applied to radial position electrode

For this case the temperature profile trend is similar with result 1.1.2, but there is no rapid change when the voltage is applied to the radial electrode.

In all cases, as the voltage is applied, the temperature profile at each point tends to be uniform.

The results showed, when the electric field is applied to the electrode in the flame reaction zone, the field-induced ion wind effect results in the field-enhanced mixing of the flame species and in the homogenization of the flame reaction zone. Moreover, the homogenization of the flame reaction zone reduces the flame peak temperature and the rate of NO_x formation

NO_x Formation

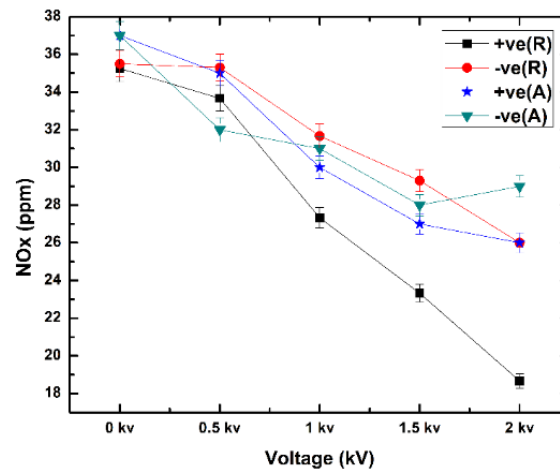


Figure 9: Effect of applied voltage on NO_x

where: +ve(R) – positive voltage, radial position

-ve(R) – negative voltage, radial position

+ve(A) – positive voltage, axial position

-ve(A) – negative voltage, axial position

The trend for NO_x formation is recorded gradually decreases as the voltage increases for all cases. The maximum NO_x was recorded approximately 37 ppm without voltage and the minimum NO_x was observed 19 ppm at +2 kV for the radial electrode. Effect of voltage on a reduction in NO_x formation is comparatively higher for the positive polarity and for the radial electrode as in Fig. 9. In the current experimental case the maximum NO_x reduction was about 48%.

Conclusion

The effect of the DC electric field on the propane diffusion swirling flame has been performed in this study. It

focused on the temperature variation, NO_x formation, when the electrode voltage is varied in the range of -2 to +2 kV. When the electric field is applied to the flame, there occurs an ion wind effect. No matter what position of electrode is used, when the positive and negative polarities are applied, the maximum flame temperature is decreased. Since the thermal NO_x is created at the hot spot region of the flame, a reduction in the flame temperature definitely results in NO_x reduction. The maximum reduction of NO_x was observed to be about 48%.

Acknowledgement

This research was financially supported by the seed money project of the KUSTAR-KAIST Institute, KAIST, South Korea.

References

- [1] Barmina, I., Descnickis, A., Meijere, A., & Zake, M. (2007). Active electric control of emissions from swirling combustion. In *Advanced Combustion and Aerothermal Technologies* (pp. 405-412). Springer Netherlands.
- [2] Heinsohn, R. J., Wilhelm, C. F., & Becker, P. M. (1970). Effect of electric fields on ducted diffusion flames. *Combustion and Flame*, 14(3), 341-349.
- [3] Fang, J., Wu, X., Duan, H., Li, C., & Gao, Z. (2015). Effects of electric fields on the combustion characteristics of lean burn methane-air mixtures. *Energies*, 8(4), 2587-2605.
- [4] Barmina, I., Kolmickovs, A., Valdmanis, R., & Zake, M. (2015). Control of combustion dynamics by an electric field, *Chemical Engineering Transaction*, 43, 973-978.
- [5] Barmina, I., Purmalis, M., Valdmanis, J., & Zake, M. (2010, September). Electric field effects on the combustion characteristics of renewable fuel. In *International Scientific Colloquium Modeling for Material Processing, Riga* (pp. 285-290).
- [6] Won, S. H., Ryu, S. K., Kim, M. K., Cha, M. S., & Chung, S. H. (2008). Effect of electric fields on the propagation speed of tribrachial flames in coflow jets. *Combustion and Flame*, 152(4), 496-506.
- [7] Afanas'ev, V. V. (1999). Active control of combustion stability by means of an electrical discharge. *Combustion, Explosion and Shock Waves*, 35(3), 252-260.
- [8] Berman, C. H., Grill, R. J., & Calcote, H. F. (1991, January). NO_x reduction in flames stabilized by an electric field. In *ASME Fossil Combs. Symposium. 3rd Energy-Sources Technology Conference*, 33, 71-76.

ECBA-17**Operation Strategy of Jeju Power System by using Frequency Regulation Energy Storage System**Seong Hoon Lee¹, Sang Heon Chae², Ngoc-Thanh Quach³, Eel-Hwan Kim⁴, Ho Chan Kim^{5*}^{1, 2, 3, 4, 5} *Department of Electrical Engineering, Jeju National University, South Korea***Abstract**

The local government of Jeju Island have a plan to install wind farms with the total capacity of 1.09 GW until 2020. In this case, the large scale of wind farm can cause frequency fluctuation. Thus, this paper proposes the installation of frequency regulation energy storage system (FR ESS) to Jeju power system. In study case, the FR ESS will control frequency and voltage in considering other generation sources and state of charge. In order to verify the effectiveness of FR ESS, the operation of high voltage direct current transmission system (HVDC) in Jeju power system will be assumed that its operation is constant power. The simulation results are carried out by using PSCAD/EMTDC simulation program.

© 2017 The Authors. Published by Academic Fora. This is an open access article under the CC BY-NC-ND license (<http://creativecommons.org/licenses/by-nc-nd/4.0/>)

Peer-review under responsibility of the Scientific & Review committee of ECBA- 2017.

Keywords— Energy Storage System, Frequency Regulation, Jeju Power System, Grid Stability, Voltage Control

Introduction

In order to solve the environmental problem from using fossil fuel, the use of renewable energies has promoted all over the world such as wind and solar energy. From this energy issue, the local government of Jeju Island in South Korea has a plan named ‘Carbon Free Island Jeju by 2030’. The objective is to make non-pollution island by using renewable energy until 2030. First goal of this plan is to install wind farms with the total capacity of 1.09 GW by 2020 [1]. The Jeju power system consists of thermal power plants, renewable energy sources, static synchronous compensators (STATCOM) and line-commutated converter high voltage direct current transmission system (LCC-HVDC) which can supply the power to Jeju power system by unidirectional operation. It means that the redundant power generated from renewable energy sources cannot be transferred to the power grid on mainland [2]-[4]. From this point, this paper proposes installation of frequency regulation energy storage system (FR ESS) with the capacity of 100 MW.

In order to verify the effectiveness of FR ESS, the operation of Jeju power system is assumed that the one of two LCC-HVDC will generate constant power. In this case, The Jeju power system will be in an unstable state.

When the FR ESS plays a role as grid frequency regulator instead of LCC-HVDC, the FR ESS must consider state of charge (SOC) of lithium ion battery. It means that the FR ESS must be charged from other generation sources according to SOC. Consequently, this paper also proposes not only the installation of FR ESS to the Jeju power system but also the operating strategy of FR ESS in accordance with SOC. For implementation of proposed method, the operation of FR ESS will be verified by using PSCAD/EMTDC simulation program. In study case, the actual parameters and measured data will be used for simulation model.

Overview of Jeju power system

The Jeju Island is located in the South area of Korean peninsula. The power grid on this island consists of distribution networks, transmission lines, substations, two LCC- HVDCs, two STATCOMs, thermal power plants and renewable energy sources as seen in Fig. 1. One of two LCC-HVDC named HVDC #1 is regulating grid frequency. The other LCC-HVDC, namely HVDC #2, also adjusts grid frequency but the response speed is slower than HVDC #1. Thus, the HVDC #2 seems to be operating as constant power. Table 1 shows the detail of generation sources in 2015. The nominal voltage of transmission lines and frequency of Jeju power system

*All correspondence related to this article should be directed to Ho Chan Kim, Jeju National University, Korea

Email: hckim@jeju.ac.kr

© 2017 The Authors. Published by Academic Fora. This is an open access article under the CC BY-NC-ND license

(<http://creativecommons.org/licenses/by-nc-nd/4.0/>)

Peer-review under responsibility of the Scientific & Review committee of ECBA-2017.

are 154 kV and 60 Hz, respectively.

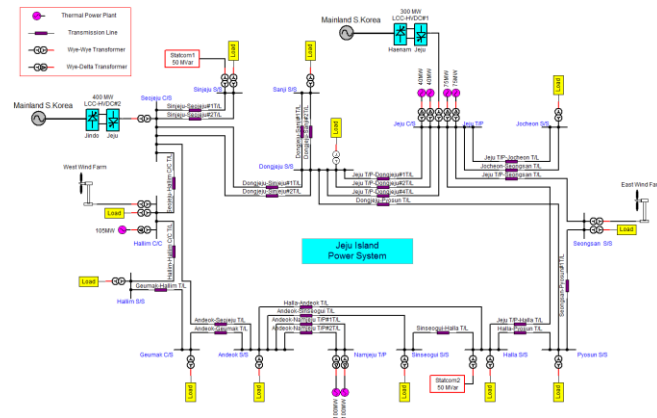


Figure 1: Configuration of Jeju power system in PSCAD/EMTDC

Table 1:

Power generating sources of Jeju power system

Items	Maximum operation capacity [MW]
Jeju T/P #2	79
Jeju T/P #3	79
Jeju D/P #1	40
Jeju D/P #2	40
Namjeju T/P #1	103
Namjeju T/P #2	103
Hallim C/C	90
HVDC #1	150
HVDC #2	250
Wind farm	140

Modeling of Jeju power system

The modeling of Jeju power system is made by using actual parameters such as line impedance and load data and so on. Fig. 2 shows the modeling of thermal power plants in PSCAD/EMTDC. They consist of synchronous generator, turbine, governor and exciter. The HVDC #1 is modeled from PSCAD/EMTDC library as illustrated as Fig. 3.

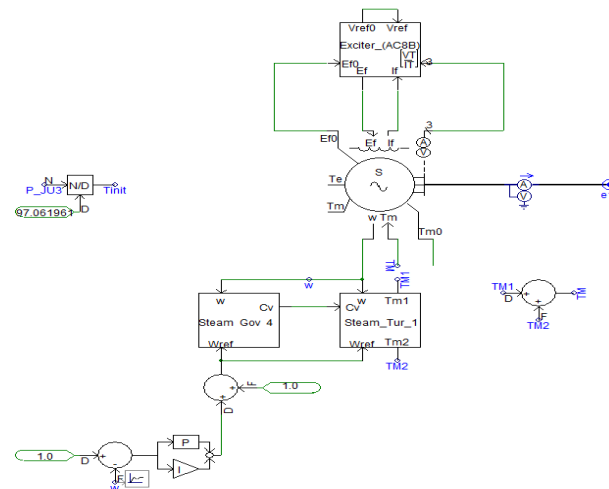


Figure 2: Modeling of thermal power plants in PSCAD/EMTDC

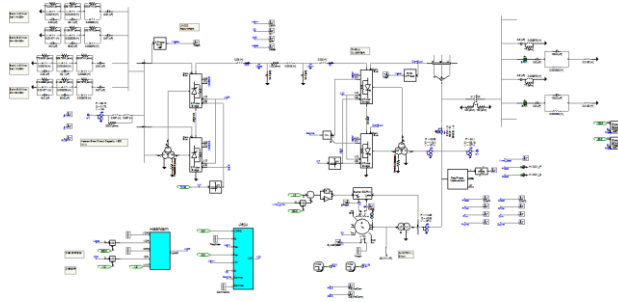


Figure 3: Modeling of HVDC #1 in PSCAD/EMTDC

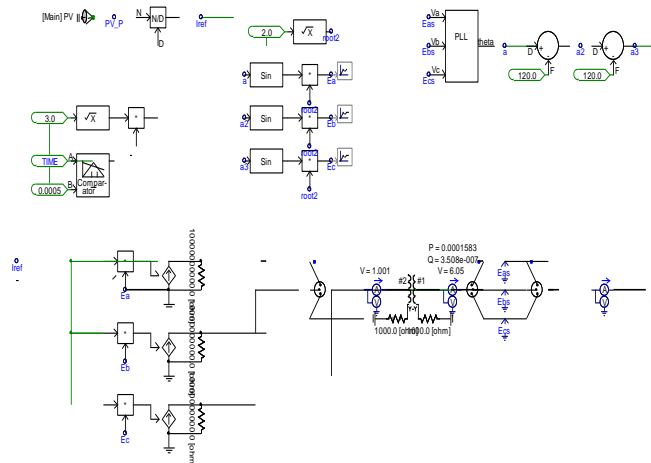


Figure 4: Modeling of controlled current source in PSCAD/EMTDC

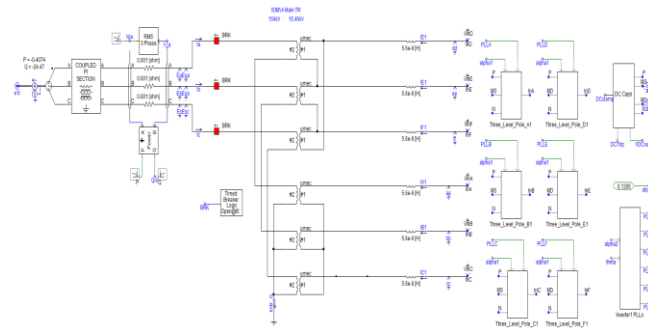


Figure 5: Modeling of STATCOM in PSCAD/EMTDC

Fig. 4 shows controlled current source in PSCAD/EMTDC. This model will be used for the HVDC #2 and the renewable energy sources in Jeju power system. In this case, the controlled current source will generate the active and reactive powers by using look-up-table from measured data [4].

Two STATCOMs are modeled by three-level voltage source converter with capacities of 50 MVar per each one as shown in Fig. 5. The STATCOMs play a role as grid voltage stabilizer [5].

Modeling of FR ESS

In this study, the FR ESS consists of lithium ion batteries and power conversion system (PCS). The modeling of the lithium ion battery consists of variable DC voltage source, inner resistor and current sensor as seen in Fig. 6. The lithium ion battery model, namely Shepherd nonlinear battery model, is calculated as [6].

$$V_{Charge} = E_0 + K \times Q / (Q - it) \times (it + iref) + A \exp(-B \times it) \quad (1)$$

$$V_{Discharge} = E_0 + K \times Q / (it - Q) \times iref - K \times Q / (Q - it) + A \exp(-B \times it) \quad (2)$$

where, V_{Charge} and $V_{Discharge}$ are charging and discharging voltages, E_0 is battery constant voltage, K is polarization constant, Q is battery capacity, A is exponential zone amplitude, B is exponential zone time constant inverse, it is actual battery charge and $iref$ is filtered current. The lithium ion battery has capacity of 100 MWh.

The topology of PCS is two-level voltage source inverter with the capacity of 100 MW. In this study case, the PCS will play a role as voltage and frequency regulators as shown in Fig. 7.

The droop controller of FR ESS has a dead band as ± 0.05 Hz and ± 5 kV. It means that the FR ESS will not respond in the dead band. The active power reference of FR ESS will be determined by not only P-f droop controller but also offset value according to SOC of battery. In this case, the SOC of FR ESS must be maintained around 0.8 for emergency situation. The output power of FR ESS must be adjusted in accordance with SOC. Therefore, if the SOC is lower than 0.75, the FR ESS will be charged energy. Then, if the SOC is higher than 0.85, the FR ESS will be discharged energy [8], [9].

According to the offset value of FR ESS, the demand load and generation sources will be different. It means that every generation source must support the FR ESS. Therefore, this paper proposes control strategy that the HVDC #2 supports active power in order to maintain SOC of FR ESS. Because the HVDC has the most rapid response in Jeju power system, it can support easier than any other sources.

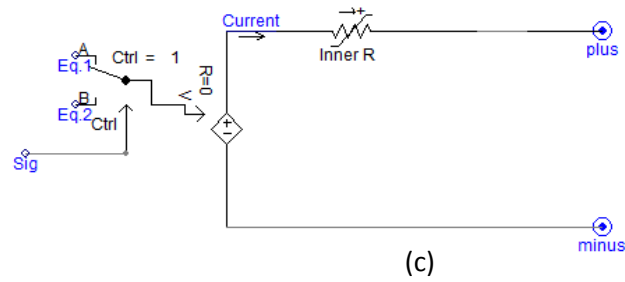


Figure 6: Modeling of lithium ion battery in PSCAD/EMTDC

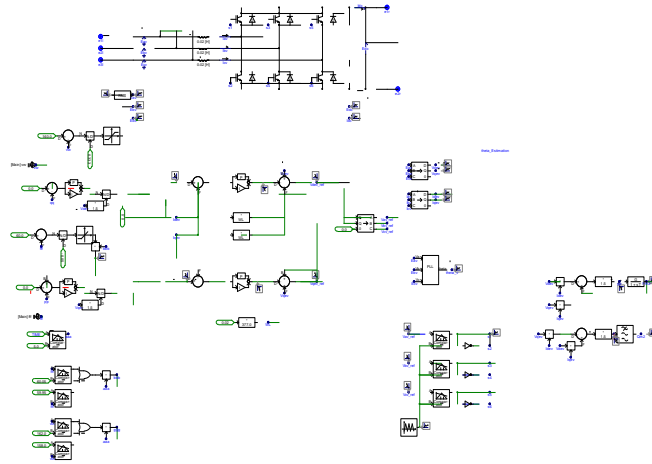
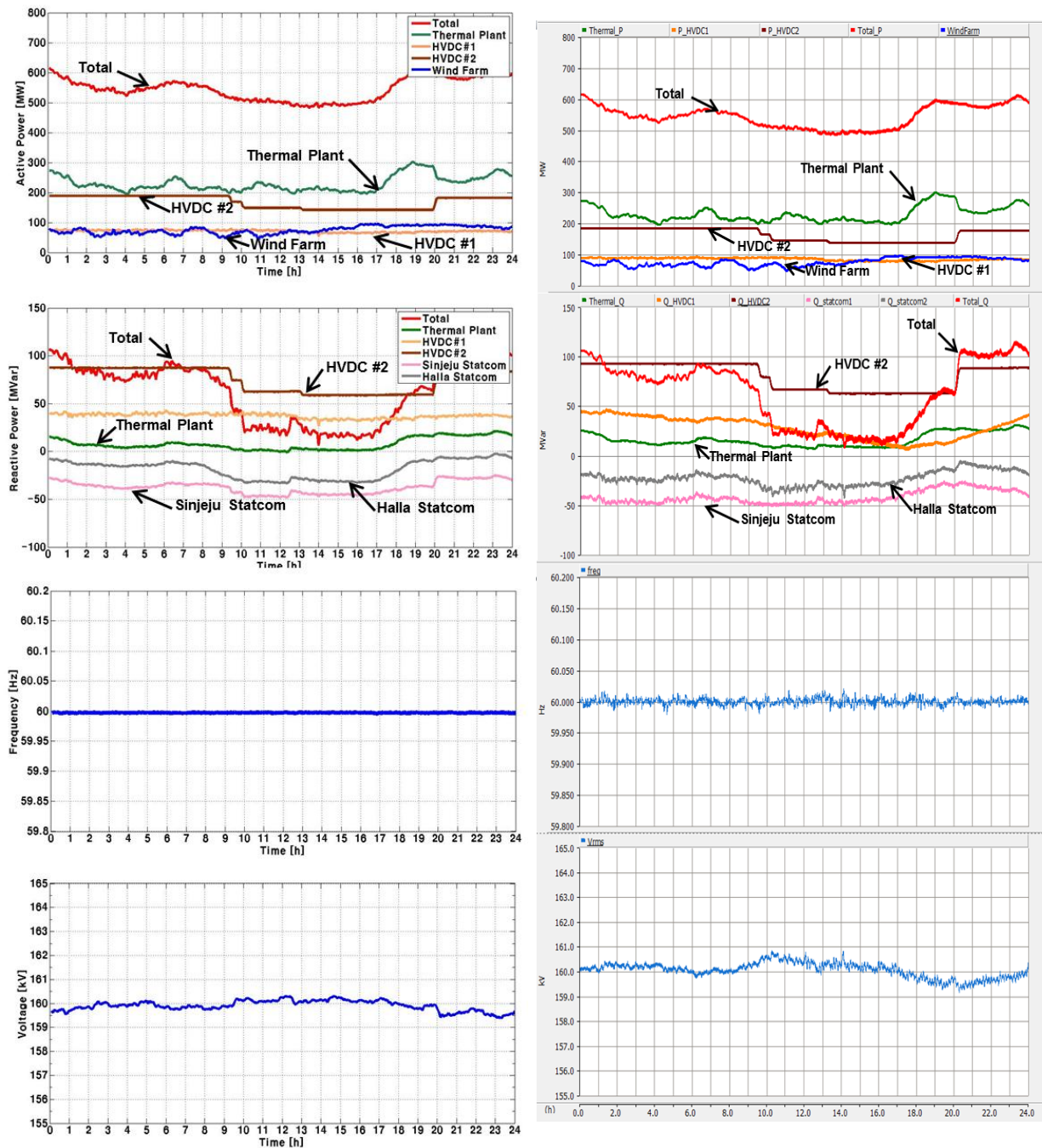


Figure 7: Modeling of PCS in PSCAD/EMTDC

Simulation Results

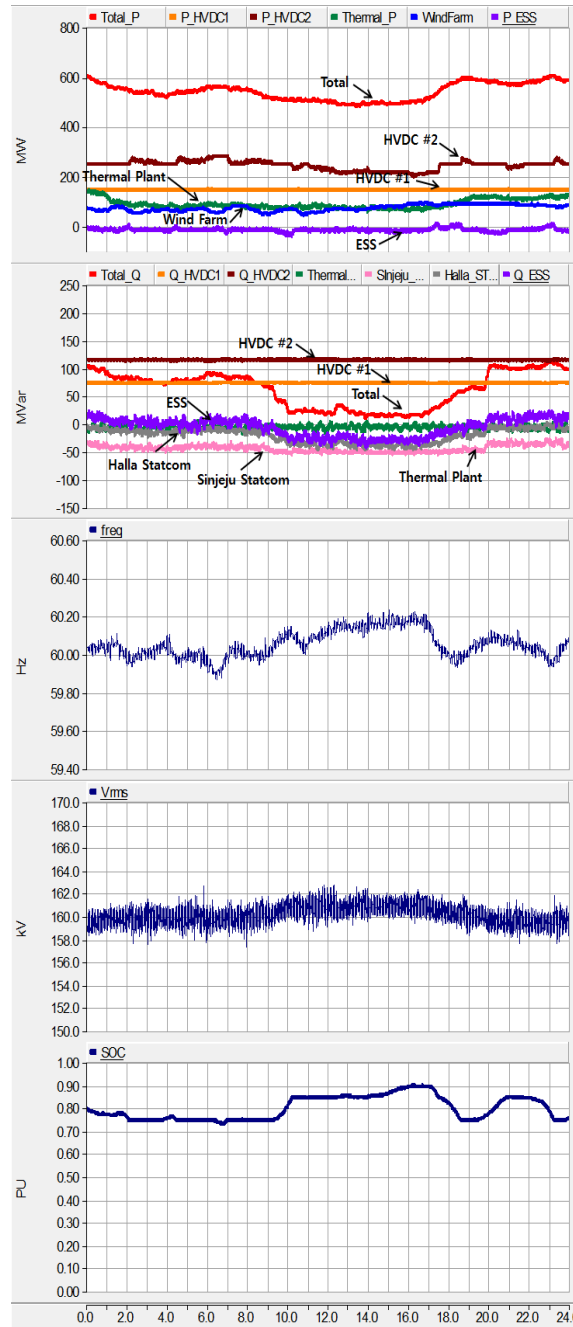
In order to verify the feasibility of simulation results, simulation results are compared with measured data in the normal operation of Jeju power system. Fig. 8 and Fig. 9 show measure data and simulation results of Jeju power

system on Feb, 18th 2015, respectively. The simulation results are quiet similar with measure data.



(a) Active power (b) Reactive power (c) Frequency (d) Voltage
Figure 9: Simulation results of Jeju power system on Feb. 18th 2016

Through the simulation model of Jeju power system, the effectiveness of installing FR ESS can be verified by modifying the operation of HVDC #1 as constant operation. In this case, the Jeju power system must be shut down because the grid frequency and voltage are in an unstable state. However, the FR ESS can solve this problem by regulating grid frequency and voltage. Fig. 10 shows the simulation results of Jeju power system with FR ESS. In this case, the HVDC #2 is operated according to SOC as illustrated Fig. 10 (a) and (e). Because the FR ESS regulates grid frequency, the reactive power of FR ESS is variable as shown in Fig. 10 (b). the grid frequency and voltage are almost achieved to standard of Korean government as ± 0.2 Hz and 4 kV as seen in Fig. 10 (c) and (d).



(a) Active power (b) Reactive power
(c) Frequency (d) Voltage (e) SOC

Figure 10: Simulation results of Jeju power system with FR ESS on Feb. 18th 2016

Conclusions

This paper has proposed installation and control strategy of FR ESS to the Jeju power system. Although the HVDC #1 is operated as a constant power source, the grid frequency and voltage are quiet stable by using the FR ESS. In addition, by using proposed control strategy of Jeju power system, the HVDC #2 can maintain the SOC of FR ESS around the standard value. Therefore, if the FR ESS is installed to Jeju power system, it will can support grid frequency and voltage at the same time.

Acknowledgement

This paper was financially supported by The Project Management Center Cultivating Smart Grid & Clean Energy Manpowers(CK-I), JNU

References

- [1] Jeju Special Self-Governing Province. (2012). *Carbon free Island Jeju by 2030*.
- [2] Kundur, P., Paserba, J., Ajarapu, V., Andersson, G., Bose, A., Canizares, C., Hatziargyriou, N., Hill, D., Stankovic, A., Taylor, C., Cutsem, T., V., & Vittal, V. (2004). Definition and classification of power system stability. *IEEE Trans. on Power System*, 19(3), 1387-1401.
- [3] Scott, N. C., Atkinson, D. J., & Morrell, J. E. (2002). Use of load control to regulate voltage on distribution networks with embedded generation. *IEEE Transactions on Power Systems*, 17(2), 510-515.
- [4] Quach, N. T., Lee, D. H., Kim, H. C., & Kim, E. H. (2015). Analyzing stability of jeju island power system with modular multilevel converter based HVDC system. *Journal of Electrical Engineering & Technology*, 10(1), 47-55.
- [5] Wang, L., & Hsiung, C. T. (2011). Dynamic stability improvement of an integrated grid-connected offshore wind farm and marine-current farm using a STATCOM. *IEEE Transactions on power systems*, 26(2), 690-698.
- [6] Tremblay, O., & Dessaint, L. A. (2009). Experimental validation of a battery dynamic model for EV applications. *World Electric Vehicle Journal*, 3(1), 1-10.
- [7] Holmes, D. G., & Lipo, T. A. (2003). *Pulse width modulation for power converters: principles and practice* (Vol. 18). John Wiley & Sons.
- [8] Delille, G., Francois, B., & Malarange, G. (2012). Dynamic frequency control support by energy storage to reduce the impact of wind and solar generation on isolated power system's inertia. *IEEE Transactions on Sustainable Energy*, 3(4), 931-939.
- [9] Oudalov, A., Chartouni, D., & Ohler, C. (2007). Optimizing a battery energy storage system for primary frequency control. *IEEE Transactions on Power Systems*, 22(3), 1259-1266.

ECBA-17

A Study on Operation of Home ESS under Fault Condition

Gi Hoon Kim¹, Ngoc-Thanh Quach², Sang Heon Chae³, Eel-Hwan Kim⁴, And Seong Bo Oh^{5*}

^{1, 2, 3, 4, 5} *Department of Electrical Engineering, Jeju National University, S. Korea*

Abstract

Nowadays, there are demands of using home energy storage system (ESS) in order to reduce electricity cost and uninterruptible operation. The ESS must maintain constant frequency and voltage in order to protect home appliances under fault condition. After the fault is removed, the ESS must be operated as the load shift controller depending on grid frequency and load angle. Therefore, this paper analyzes the operation of home ESS under fault condition and synchronized operation. The simulation results are carried out by using PSCAD/EMTDC simulation program.

© 2017 The Authors. Published by Academic Fora. This is an open access article under the CC BY-NC-ND license (<http://creativecommons.org/licenses/by-nc-nd/4.0/>)

Peer-review under responsibility of the Scientific & Review committee of ECBA- 2017.

Keywords— Energy Storage System, Home Energy Management, Fault Condition, Load Angle, Voltage Stability

Introduction

In the industrial site and even home, uninterruptible operation of electric device is very important. Thus, many people are using uninterruptible power supply (UPS) nowadays. The UPS can be only operated in the black-out situation. However, the energy storage system (ESS) can be operated as an uninterruptible controller and a load shift controller [1]. Therefore, the demands of home ESS is increasing all over the world. If the circuit breaker is opened in the black-out or fault condition, the home ESS should supply the active and reactive powers for home appliances which means demand load [2]. In this case, the home ESS must generate nominal frequency and voltage which are 60 Hz and 380 V/220 V in South Korea, respectively. After the black-out or fault is removed, the home ESS must be reconnected the main grid through the synchronization control. It means that voltage, frequency and phase angle of the home ESS must be the same as those of main grid. In order to synchronize operation, the phase angle must be regulated slowly [3]. Consequently, this paper analyzes the operation of home ESS under fault condition and synchronized operation. The home ESS will be operated in three cases. Firstly, the home ESS operates under normal condition. In this case, the home ESS is charged energy and operates as the load shift controller. Secondly, the ground fault occurs at grid side. The circuit breaker will be opened. Thus, the home ESS is operated independently and discharges energy for demand load. In order to supply electricity power in isolated operation, the home ESS must supply power to demand load according to nominal frequency and voltage. Thirdly, after ground fault is removed, the ESS will control frequency and voltage for synchronization. If the synchronization conditions are achieved, the circuit breaker will be closed. In order to evaluate the proposed method, the operation of home ESS will be verified by using PSCAD/EMTDC simulation program.

Modelling of Home ESS

Generally, configuration of the home ESS is the same with a typical ESS which consists of lithium ion battery and power conversion system (PCS). In this study case, the output of the lithium ion battery is determined by using Shepherd nonlinear battery model which is made by variable DC voltage source, inner resistor and current sensor as seen in Fig. 1. The output voltage of battery model is calculated as [4].

$$V_{Charge} = E_0 + K \times Q / (Q - it) \times (it + iref) + A \exp(-B \times it) \quad (1)$$

$$V_{Discharge} = E_0 + K \times Q / (it - Q) \times iref - K \times Q / (Q - it) + A \exp(-B \times it) \quad (2)$$

*All correspondence related to this article should be directed to Seong Bo Oh, Jeju National University, Korea

Email: sboh@jeju.ac.kr

© 2017 The Authors. Published by Academic Fora. This is an open access article under the CC BY-NC-ND license

(<http://creativecommons.org/licenses/by-nc-nd/4.0/>)

Peer-review under responsibility of the Scientific & Review committee of ECBA-2017.

where, V_{Charge} and $V_{Discharge}$ are charging and discharging voltage, E_0 is battery constant voltage, K is polarization constant, Q is battery capacity, A is exponential zone amplitude, B is exponential zone time constant inverse, i_t is actual battery charge and i_{ref} is filtered current. It will have capacity of 7 kWh.

The PCS is modeled by two-level voltage source converter with the capacity of 3 kW [5]-[7]. In this study case, the PCS will be operated as a load shift controller in normal condition and a constant voltage constant frequency (CVCF) controller under fault condition [8], [9].

The overall configuration of simulation model consists of home ESS, load, transformer, main grid, circuit breaker and fault logic as illustrated in Fig. 3. In this simulation, the fault logic can make ground or short faults on grid.

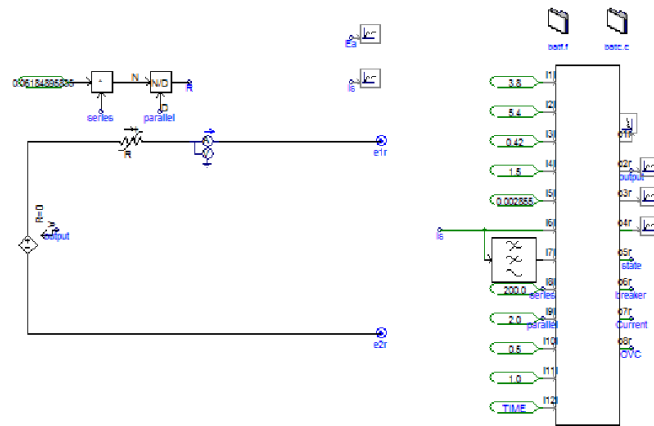


Figure 1: Modeling of lithium ion battery in PSCAD/EMTDC

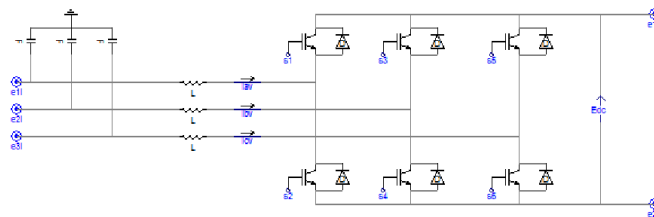


Figure 2: Modeling of PCS in PSCAD/EMTDC

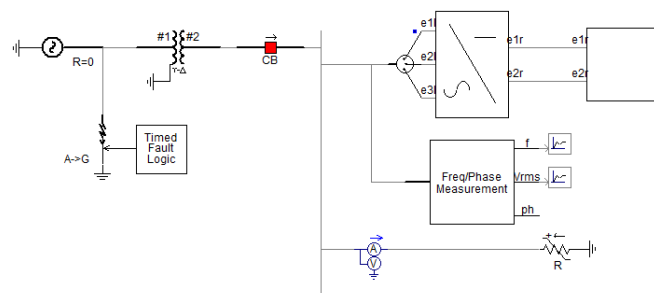


Figure 3: Overall configuration of simulation model in PSCAD/EMTDC

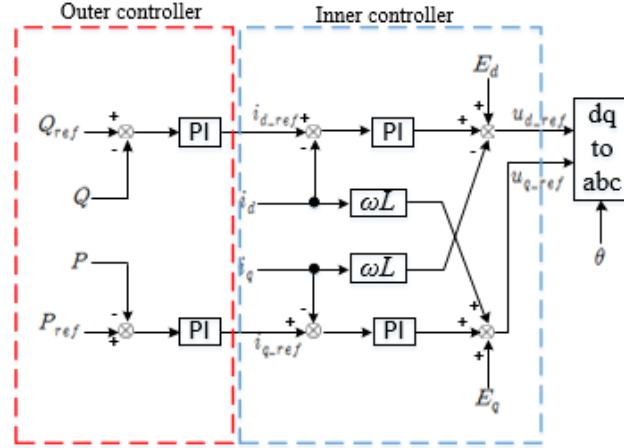


Figure 4: Schematic diagram of active and reactive power controller

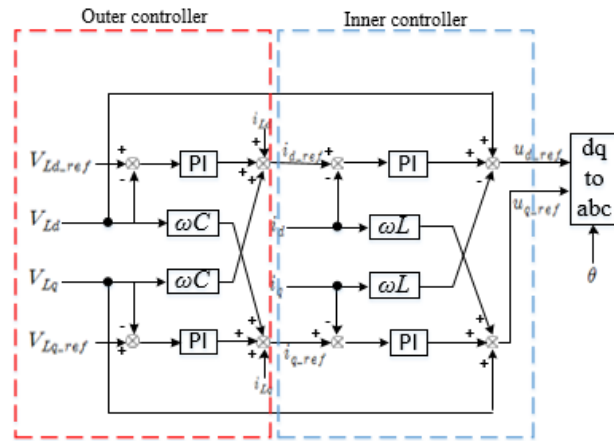


Figure 5: Schematic diagram of CVCF controller

Operation of Home ESS

The objective of installing home ESS is to save electricity cost. Therefore, the home ESS charges the active power in the time of the cheapest electricity cost like daybreak. Then, the home ESS will discharge the active power in peak time for demand load. It means that the PCS operates as the active and reactive power controllers as seen in Fig. 4. It means that grid connected operation. The controller of PCS consists of outer and inner controllers. The outer controller makes dq axis current reference in accordance by using information of active and reactive power. the inner controller determines dq axis voltage reference. Then, the dq-axis voltage reference will be transformed to three-phase voltage reference by using dq transformation method [5]-[7].

Fig. 5. shows schematic diagram of CVCF controller. It consists of outer and inner controllers. The outer controller can make dq axis current reference by using information of load voltage. The inner controller is able to generate dq-axis voltage reference. Then, the voltage reference will be transformed to three-phase voltage reference. In this case, there is no phase angle from main grid. Thus the three-phase voltage reference will be transformed by using load angle or synchronized angle generated by itself. Fig. 6 shows the PLL depend on control scheme. When the active power and reactive power controller is changed to CVCF controller at 1.5 s, it generates PLL by itself [8], [9].

In order to synchronize, there are three conditions. First and second condition are the amplitude of voltage and the frequency, respectively. Because every home appliance must use nominal voltage and frequency, those conditions are already achieved. However, third condition which is the phase angle is different from main grid. Thus, the home ESS must adjust phase angle by using PLL in order to achieve third condition. When the fault is removed, the home ESS can detect stable grid voltage. In this case, the home ESS will adjust load side PLL 1% per 2π as seen in Fig. 7. Then, if the error between grid and load side PLL is less than 0.1 radian, the circuit breaker will be closed.

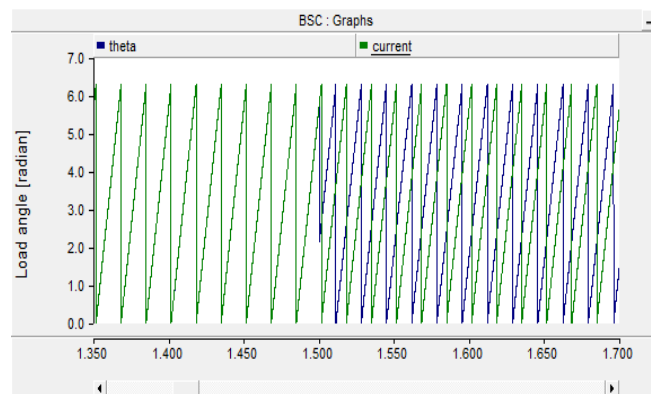


Figure 6: Load angle under fault condition

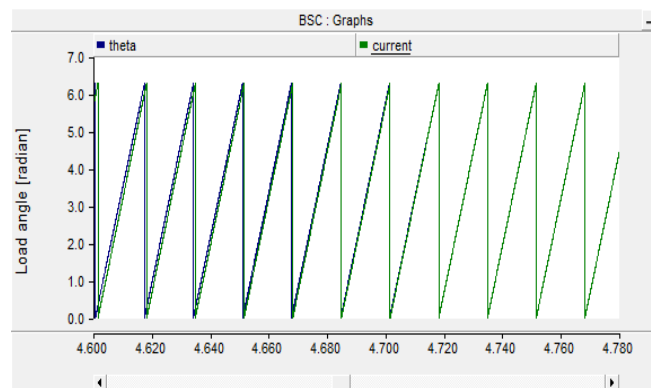
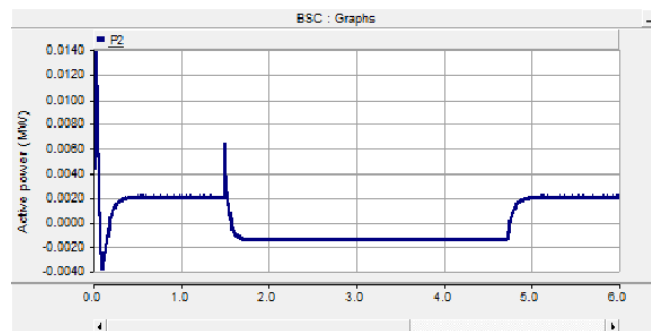
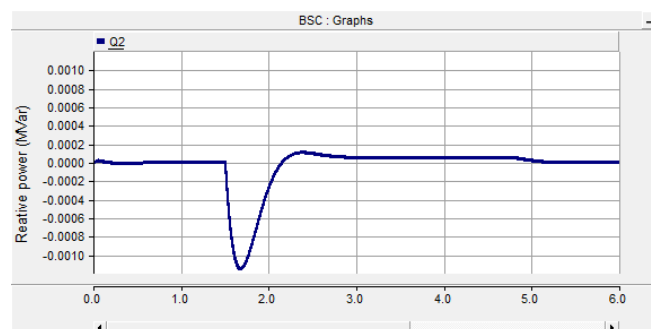


Figure 7: Synchronous operation of load angle

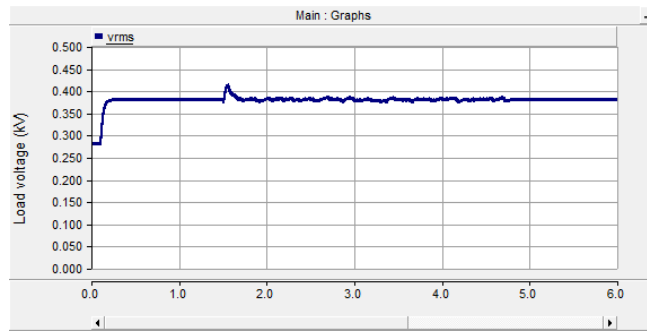
Simulation Results



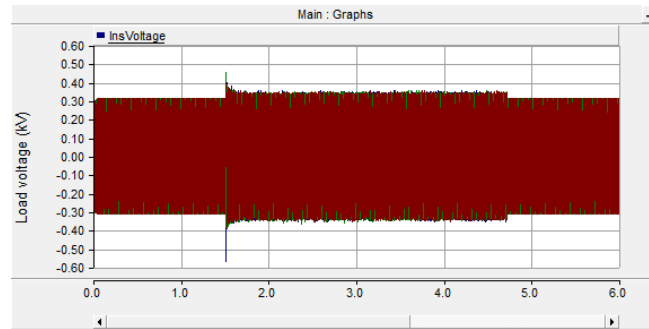
(a) Active power



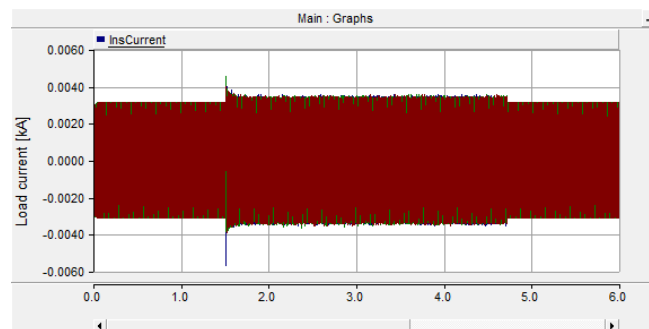
(b) Reactive power



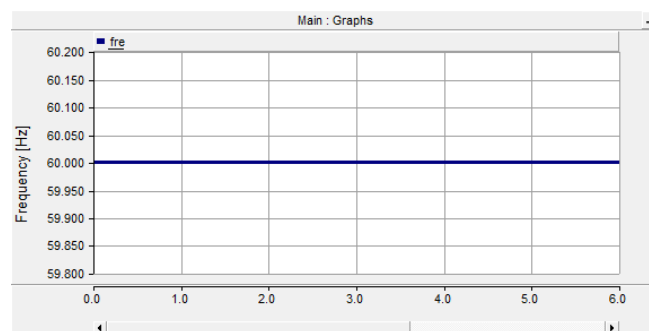
(c) RMS voltage



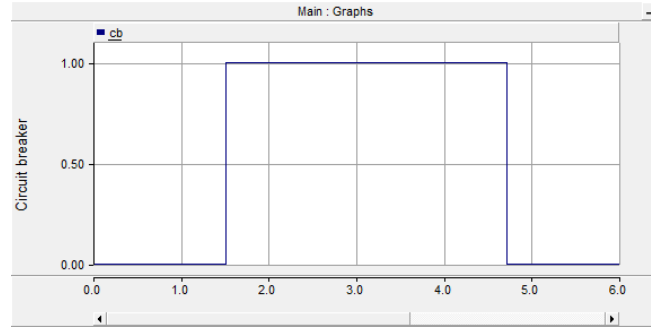
(d) Instantaneous voltage



(e) Instantaneous current



(f) Frequency



(g) Operation of circuit breaker

Figure 8: Total simulation results in PSCAD/EMTDC

In order to analyze the operation of home ESS, there are three cases of operation. In first case, the home ESS charge active power for load shift controller from $t = 0$ s to $t = 1.5$ s. In second case, the single line to ground fault occurs at $t = 1.5$ s and remains until $t = 4.5$ s. In third case, the fault is removed at $t = 4.5$ s. The overall simulation results are seen in Fig. 7.

Fig 8 (a) is the active power. From 0 s to 1.5 s, the ESS is charging energy with the constant value of 2 kW. However, after fault occurs on grid at 1.5 s, the ESS will discharge energy for demand load. Fig. 8 (b) shows the reactive power. In this case, the load is only resistor load. Therefore, the reactive power is always zero excepting at the transient time when the fault occurs. Figs. 8 (c) and (d) present the load voltage. In this study case, both RMS (Root mean square) and instantaneous voltages almost achieve the nominal value of 380 V. Especially, when the circuit breaker is closed, the transient voltage is quiet stable because the synchronous operation can improve the transient state. In this case, the phase angles of main grid and ESS are synchronized at $t = 4.68$ s as shown in Fig. 8. If there is no synchronous operation, the circuit breaker will be closed at $t = 4.5$ s. However, the circuit breaker is closed at $t = 4.68$ s as seen in Fig. 8 (g). Fig. 8 (f) shows the grid frequency. It always achieves the nominal frequency of 60 Hz.

Conclusion

This paper has analyzed the operation of home ESS under fault condition. From the simulation results, when the fault occurs on main grid, the demand load can be supplied the energy from the home ESS. After the fault is removed, the home ESS is operated for synchronization. Although the circuit breaker is closed and controller are changed from CVCF to active and reactive power controller, the load can be supplied power constantly.

Acknowledgement

This paper was financially supported by The Project Management Center Cultivating Smart Grid & Clean Energy Manpowers(CK-I), JNU

References

- [1] Yao, L., Lai, C. C., & Lim, W. H. (2015, December). Home energy management system based on photovoltaic system. In *Data Science and Data Intensive Systems (DSDIS), 2015 IEEE International Conference on* (pp. 644-650). IEEE.
- [2] Erdinc, O., Paterakis, N. G., Mendes, T. D., Bakirtzis, A. G., & Catalão, J. P. (2015). Smart household operation considering bi-directional EV and ESS utilization by real-time pricing-based DR. *IEEE Transactions on Smart Grid*, 6(3), 1281-1291.
- [3] Quan, X., Wu, Z., Dou, X., Hu, M., & Zhang, J. (2016, October). Discrete time optimal design for voltage prefilter in grid synchronization system from control perspective. In *Industrial Electronics Society, IECON 2016-42nd Annual Conference of the IEEE* (pp. 3360-3365). IEEE.
- [4] Tremblay, O., & Dessaint, L. A. (2009). Experimental validation of a battery dynamic model for EV applications. *World Electric Vehicle Journal*, 3(1), 1-10.
- [5] Oudalov, A., Chartouni, D., & Ohler, C. (2007). Optimizing a battery energy storage system for primary frequency control. *IEEE Transactions on Power Systems*, 22(3), 1259-1266.
- [6] Scott, N. C., Atkinson, D. J., & Morrell, J. E. (2002). Use of load control to regulate voltage on distribution networks with embedded generation. *IEEE Transactions on Power Systems*, 17(2), 510-515.

- [7] Holmes, D. G., & Lipo, T. A. (2003). *Pulse width modulation for power converters: principles and practice* (Vol. 18). John Wiley & Sons.
- [8] Wang, Y., Lu, Z., Min, Y., & Shi, S. (2010, June). Comparison of the voltage and frequency control schemes for voltage source converter in autonomous microgrid. In *Power Electronics for Distributed Generation Systems (PEDG), 2010 2nd IEEE International Symposium on* (pp. 220-223). IEEE.
- [9] Li, F., Shen, C., Wu, X., Zhao, M., & Huang, X. (2014, July). A comparison of different control strategies in inverter connected micro-grids. In *Control Conference (CCC), 2014 33rd Chinese* (pp. 3563-3567). IEEE.

ECBA-17**Analyzing the Effect of Offshore Wind Farm to Onshore Power Grid based on MMC-HVDC System**Min Hyeok Kang¹, Ngoc-Thanh Quach², Sang Heon Chae³, Young Gyu Jin⁴, Eel-Hwan Kim^{5*}^{1, 2, 3, 4, 5} *Department of Electrical Engineering, Jeju National University, S. Korea*

Abstract

This paper proposes an analysis on the effect of offshore wind farm (OWF) to onshore power grid based on modular multilevel converter - high voltage direct current (MMC-HVDC) system. To transfer the active power from the OWF to the onshore power grid, a MMC-HVDC system is used. However, the output power of wind farm is often variable because of the intermittence of the wind velocity. Thus, the grid voltage at the point of common coupling (PCC), where the MMC-HVDC system is connected, will be fluctuated according to the output power of OWF. To overcome this problem, onshore MMC will be designed in order to eliminate the fluctuation as well as supporting for the grid voltage at the PCC by injecting the reactive power into the power system. The effectiveness of the proposed method is verified by the simulation results based on PSCAD/EMTDC simulation program.

© 2017 The Authors. Published by Academic Fora. This is an open access article under the CC BY-NC-ND license (<http://creativecommons.org/licenses/by-nc-nd/4.0/>)

Peer-review under responsibility of the Scientific & Review committee of ECBA- 2017.

Keywords— Offshore Wind Farm, Fluctuation, Mmc-Hvdc, Voltage Control, Point of Common Coupling

Introduction

In fact, the capacity of the fossil fuel resources such as oil, coal, and natural gas is finite, while the nuclear energy can supply a huge amount of energy. However, both fossil fuel and nuclear energy cause the problems of environmental pollution. The renewable energies including wind and solar energies are known as clean and infinite energy resources. During the last decades, many countries have used the wind energy such as China, USA, Germany, India, Denmark, South Korea, etc. [1]. Recently, offshore wind farms (OWF) have emerged as a new technology for the wind power generation. The advantages of the OWF over the onshore wind farm are higher and smoother wind velocities, and more suitable onshore sites, etc. [1, 2]. The output power of OWF is fluctuated according to the wind velocity and may cause the fluctuation of voltage at the point of common coupling (PCC), where the OWF is connected [3, 4]. The technologies to connect between the OWF and the onshore power grid consist of the high voltage alternative current (HVAC) and high voltage direct current (HVDC) transmission systems. The HVDC transmission system has been demonstrated to be more economical than the HVAC transmission system when the transmission distance is over 100 km [5]. Moreover, the OWF will not be directly affected by the disturbances of the onshore power grid because of the decoupling control of converters in the HVDC system. Among the HVDC topologies, the voltage source converter-HVDC (VSC-HVDC) system is more attractive than the others because of the ability of controlling active power and reactive power independently. Besides, the VSC-HVDC system can also support for the grid voltage and frequency by using auxiliary controllers [6]. The modular multilevel converter (MMC) is a new type of the VSC topologies [7, 8]. It has some advantages such as low total harmonic distortion (THD), low switching frequency, high capacity, and high availability. Because of these dominant advantages, the MMC is one of the promising topologies for the HVDC transmission applications [9]. Recently, the MMC-HVDC system has been developed for the OWF in order to transfer the power from the OWF to the onshore power grid. The operation and control strategies of the MMC-HVDC system have been researched by many authors over the world [10, 11]. However, there is still no full research on the OWF applications yet. Thus, this paper proposes an analysis on the effect of OWF to the onshore power grid based on MMC-HVDC system. Normally, the grid voltage at the PCC will be fluctuated due to the fluctuation of the output power of OWF. To overcome this problem, the onshore MMC is designed to support for the grid voltage by injecting the reactive power into the power system at the PCC. Besides, the onshore MMC can also compensate for the sag voltage at the PCC that is caused by the voltage drop on the impedance of transmission lines and transformers.

Offshore Wind Farm and Mmc-Hvdc System

The single-line diagram of an OWF connected the onshore power grid through a MMC-HVDC system is shown

*All correspondence related to this article should be directed to Eel-Hwan Kim, Jeju National University, Korea

Email: ehkim@jeju.ac.kr

© 2017 The Authors. Published by Academic Fora. This is an open access article under the CC BY-NC-ND license

(<http://creativecommons.org/licenses/by-nc-nd/4.0/>)

Peer-review under responsibility of the Scientific & Review committee of ECBA-2017.

in Fig. 1. An OWF is assumed to include several wind turbine generators (WTGs). To collect the active power from individual WTGs into the offshore power grid, a string or star cluster configuration is often used [5]. The string cluster configuration requires a step-up transformer for each WTG, while the star cluster configuration requires a large platform for installing a high power transformer. In this study, the string cluster configuration is used because each WTG system usually uses a step-up transformer and thus an extra transformer is not necessary. After collecting the active power from the individual WTGs, the total output power of OWF is injected into the MMC-HVDC system and this amount of

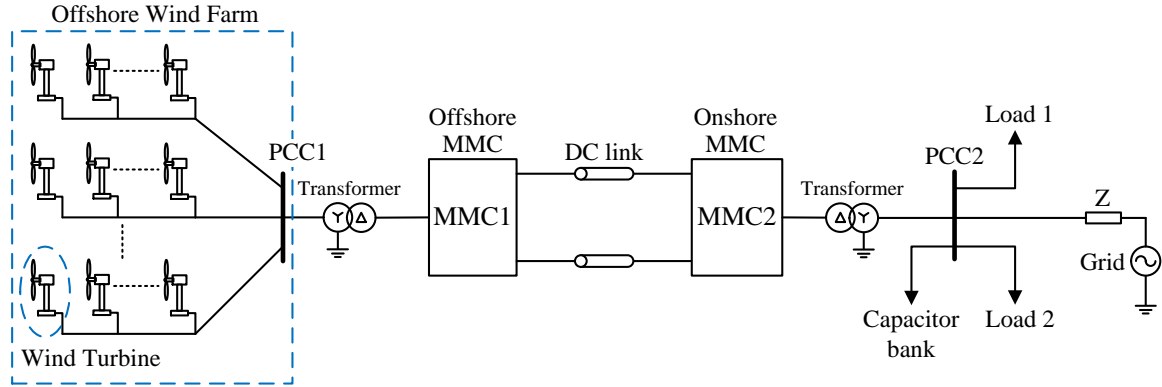


Fig. 1. Configuration of the power system. The power will be then transferred to the onshore power grid at the PCC. Thus, the OWF can be modelled by the current sources. Although the OWF can support the reactive power for the AC bus, this capability is not considered in the study. The modelling of the OWF is expressed in Fig. 2.

The configuration of the MMC is shown in Fig. 3. It is created by six arms. Each arm includes N submodules (SMs) which are arranged in series and a series arm inductor. The MMC is linked to the AC power grid through a wye-delta (Y- Δ) transformer. A MMC-HVDC system consists of two MMC which are connected back-to-back together as seen in Fig. 1. Normally, one MMC is employed to control the active and reactive powers. The other one is used to maintain the DC-link voltage constant.

Proposed Control Strategy

In this study, the MMC-HVDC system not only play a role of intermediate transmission device, but also support the grid voltage at the PCC. The output power of wind farm is very difficult to determine because the OWF is composed by several WTGs. Thus, the offshore MMC (MMC1), which is located at the offshore side, will be operated as a voltage source. The onshore MMC (MMC2) will be responsible for controlling the DC-link voltage and supporting the grid voltage at the PCC.

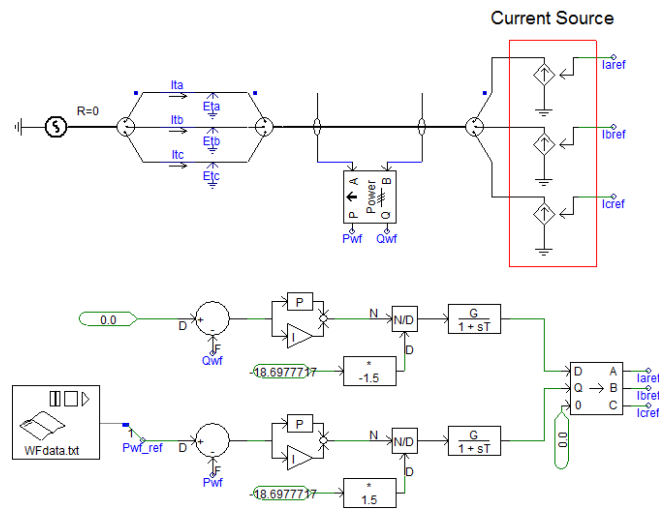


Figure 2: Modelling of the offshore wind farm

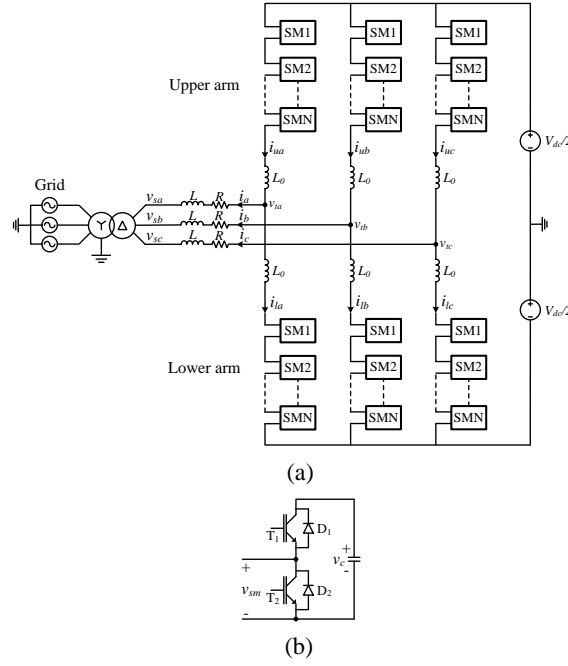


Figure 3: MMC configuration

In the power transmission system, there is a voltage drop at the receiver side because the impedance of the transmission lines and transformers. From Fig. 3, the voltage drop on the reactor RL is calculated as [12]

$$\begin{aligned} \Delta v_2 &= v_{t_2} - v_{s_2} \\ &= \frac{RP_2 - XQ_2}{v_{s_2}} + j \frac{XP_2 + RQ_2}{v_{s_2}} \end{aligned} \quad (1)$$

where Δv_2 is the voltage drop on the reactor RL. v_{t_2} and v_{s_2} are the terminal and grid voltages of the MMC2, respectively. P_2 and Q_2 are the active power and the reactive power of the MMC2.

Because the phase shift angle between the grid voltage and terminal voltage is small, the imaginary part in (1) is very small in comparing to the real part. Besides, the value of reactance, X , is assumed to be very high to the value of the resistance, R ($X \gg R$). Thus, the voltage drop can be rewritten as

$$\Delta v_2 \approx -\frac{XQ_2}{v_{s_2}} \quad (2)$$

Consequently, the voltage controller of the onshore MMC can be designed as

$$Q_2^* = \left(k_p + \frac{k_i}{s} \right) (v_{pcc_2}^* - v_{pcc_2}) \quad (3)$$

where k_p and k_i are the proportional and integral gains of the PI controller. * denotes the reference value.

The overall control strategy of the MMC-HVDC system is shown in Fig. 4. The operations of the “ S_a ” and “ S_b ” are as follows.

- ✓ $S_a \rightarrow a_1, S_b \rightarrow b_1$: MMC1 operates as a voltage source and controls the dq-axis voltage.
- ✓ $S_a \rightarrow a_2, S_b \rightarrow b_2$: MMC2 controls the voltage at the PCC and DC-link voltage.

Simulation Results and Discussion

In this study, a 200 MW OWF is connected to the onshore power grid through a 200 MW MMC-HVDC system. The parameters of power system are shown in Table 1. The simulation results are carried out in two cases of operation. First case is the operation of the power system without controlling the grid voltage at the PCC2. Second case is the control of grid voltage at the PCC2. The electric load is assumed as RL series loads which are connected at the PCC2, and they are the same in two cases.

Because of the decoupling control between the MMC1 and the MMC2, the operations of the OWF and the MMC1 in two cases are almost similar together as shown in Fig. 5. The MMC1 operates as a voltage source. It means that the MMC1 controls the dq-axis voltage at the AC side. As a result, the dq-axis voltage is maintained at the reference value as seen in Fig. 5(a). This study assumes that the active power transferred

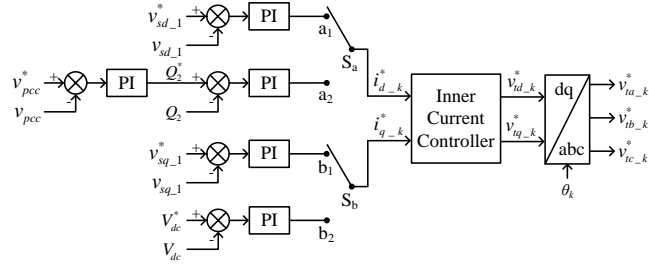
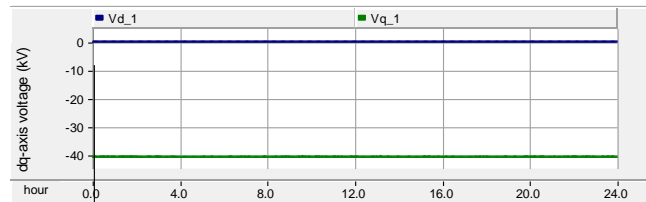


Figure 4: Control diagram of the MMC-HVDC system

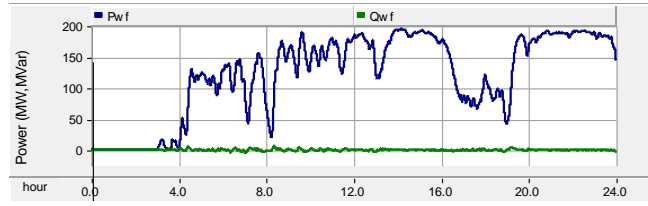
Table 1:

Parameter of the power system

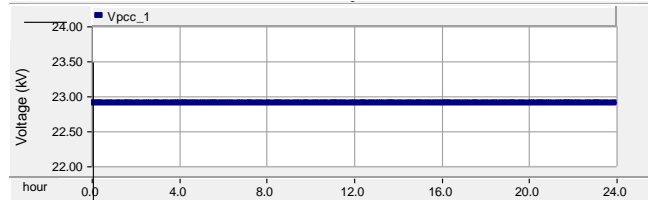
Offshore Wind Farm	
Nominal power	200 MW
AC voltage	22.9 kV
MMC-HVDC System	
Active power	200 MW
Reactive power	100 MVar
AC system voltage	154 kV
Nominal frequency	60 Hz
Transformer ratio	154 kV/50 kV
Dc-link voltage	±50 kV
Number of SMs per arm	20
Arm inductance	3.5 mH
Submodule capacitance	7800 μF



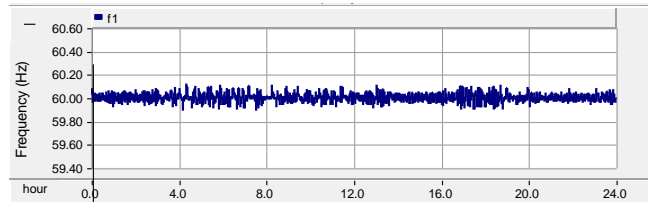
(a) dq-axis voltage



(b) Output power of offshore wind farm



(c) Grid voltage at PCC1

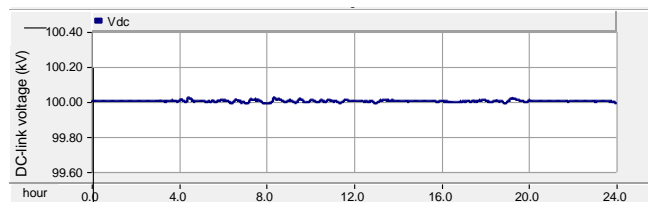


(d) Grid frequency at PCC1

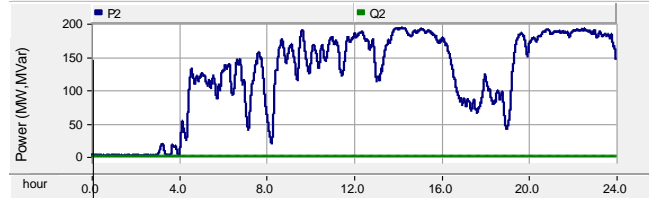
Figure 5: Operations of the MMC1 and the offshore power grid

by MMC-HVDC system is equal to the output power of the OWF. The output power of the OWF is fluctuated because the intermittence of the wind velocity as seen in Fig. 5(b). The reactive power from the OWF is set to zero. The grid voltage and grid frequency at the offshore power grid is almost constant during operating time (Figs. 5(c) and (d)) due to this voltage is actually controlled by the MMC1.

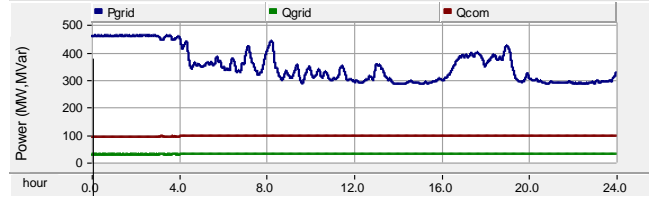
The operations of the MMC2 and the onshore power grid in the First case is shown in Fig. 6. The MMC2 is responsible for controlling the DC-link voltage that is almost constant as illustrated in Fig. 6(a). If the power losses are ignored, the active power received at the onshore power grid will be equal to the input power of the MMC1 as seen in Fig. 6(b). In this case, the MMC2 does not control the grid voltage. It means that the reactive power from the MMC-HVDC system is equal to zero. Therefore, the reactive power required from the electric load (Fig. 6(d)) will be supplied from the onshore power grid and the capacitor bank as shown in Fig. 6(c). It can be seen that the grid voltage at the PCC2 is dropped below the nominal value of 154 kV because of the losses on the transmission lines and transformers as shown in Fig. 6(e). Besides, the grid voltage is also fluctuated because it is affected by the fluctuation of the active power from the OWF. Although such voltage fluctuation, the grid frequency is still stable as seen in Fig. 6(f).



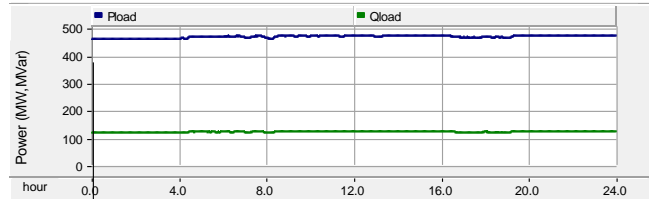
(a) DC-link voltage



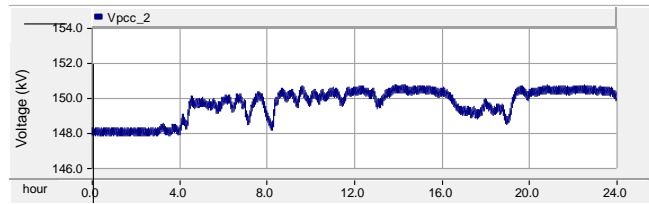
(b) Active and reactive powers of MMC2



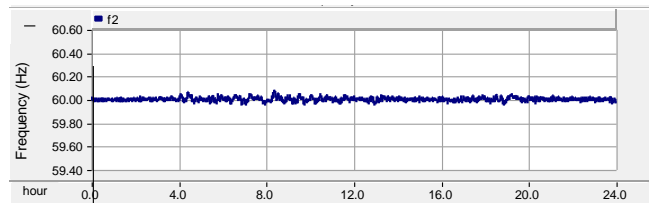
(c) Active and reactive powers of onshore power grid



(d) Load demand



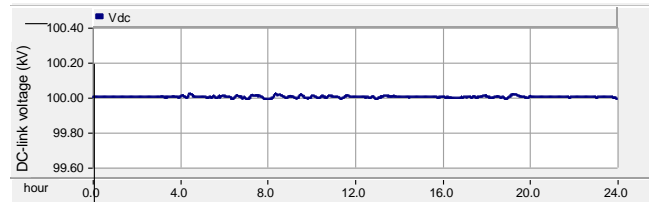
(e) Grid voltage at PCC2



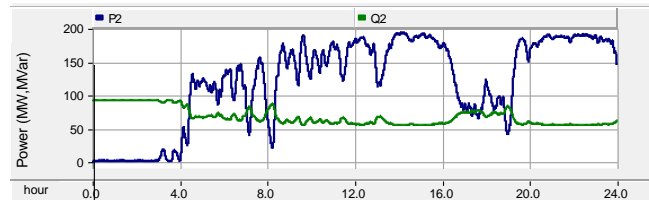
(f) Grid frequency at PCC2

Figure 6: Operations of the MMC2 and the onshore power grid – First case

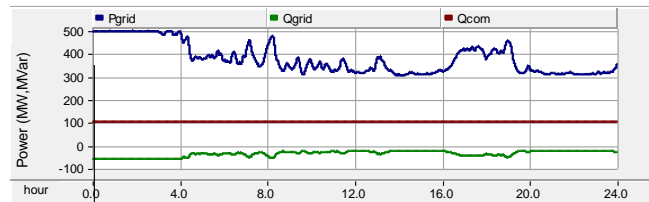
In order to solve these problems, the MMC2 is designed to support for the grid voltage at the PCC2. The operations of the MMC2 and the onshore power grid in the Second case are shown in Fig. 7. The DC-link voltage is kept constant and it is similar to the First case. The active power transferred by the MMC-HVDC system is unchanged, while the MMC2 injects the reactive power into the onshore power grid in order to improve the grid voltage as illustrated in Fig. 7(b). Consequently, the grid voltage at the PCC2 is regulated to the nominal value of 154 kV and it is stable during the operating time while the output power of the OWF is variable as shown in Fig. 7(e). This demonstrates the effectiveness of the proposed method. The ability of regulating grid voltage of the



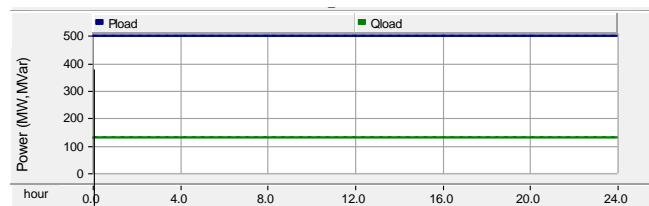
(a) DC-link voltage



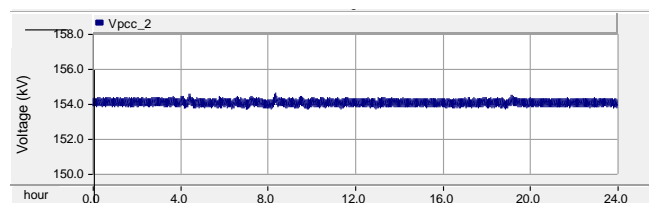
(b) Active and reactive powers of MMC2



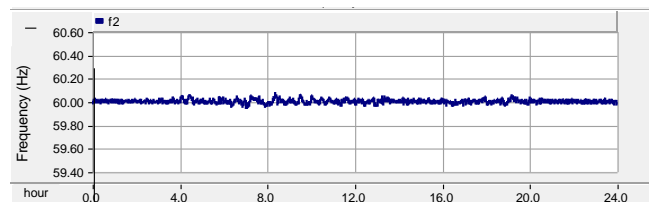
(c) Active and reactive powers of onshore power grid



(d) Load demand



(e) Grid voltage at PCC2



(f) Grid frequency at PCC2

Figure 7: Operations of the MMC2 and the onshore power grid – Second case

MMC-HVDC system depends on its rated reactive power. If the required reactive power is higher than the rated value of the MMC-HVDC system, the MMC-HVDC system will inject the maximum reactive power into the power system. Then, a compensation of reactive power is required to support the grid voltage.

Conclusions

This paper has proposed an analysis on the effect of OWF to the onshore power grid based on MMC-HVDC system. The output power fluctuation of OWF causes the voltage fluctuation at the PCC of onshore power grid. A MMC-HVDC system with the advantages such as low THD, low switching frequency, high capacity, and high availability can control the active power and the reactive power independently. Based on these performances, the MMC-HVDC system is implemented a voltage controller in order to improve the grid voltage at the PCC. The simulation results have demonstrated that the MMC-HVDC system can regulate the grid voltage and reduce the voltage fluctuation at the PCC by injecting the reactive power into the onshore power grid. This can compare to the operation of STATCOM. While the MMC-HVDC system and the OWF is the promising systems in the near future, a perfect control structure can save the costs as well as improving the stability and reliability of the power system.

Acknowledgement

This research was financially supported by The Project Management Center Cultivating Smart Grid & Clean Energy Manpowers(CK-I), JNU.

References

- [1] GWEC Global Wind Energy Council. (2015). *Global wind report 2015*. Retrieved from <http://www.gwec.net/?s=Global+wind+2015+report>
- [2] Young, E. (2015). Offshore wind in Europe: walking the tightrope to success. *Ernst & Young, Paris*.
- [3] Kundur, P., Paserba, J., Ajarapu, V., Andersson, G., Bose, A., Canizares, C., ... & Van Cutsem, T. (2004). Definition and classification of power system stability IEEE/CIGRE joint task force on stability terms and definitions. *IEEE transactions on Power Systems*, 19(3), 1387-1401.
- [4] Wang, L., & Hsiung, C. T. (2011). Dynamic stability improvement of an integrated grid-connected offshore wind farm and marine-current farm using a STATCOM. *IEEE Transactions on power systems*, 26(2), 690-698.
- [5] Bresesti, P., Kling, W. L., Hendriks, R. L., & Vailati, R. (2007). HVDC connection of offshore wind farms to the transmission system. *IEEE Transactions on energy conversion*, 22(1), 37-43.
- [6] Liu, H., & Chen, Z. (2015). Contribution of VSC-HVDC to frequency regulation of power systems with offshore wind generation. *IEEE Transactions on Energy Conversion*, 30(3), 918-926.
- [7] Saeedifard, M., & Iravani, R. (2010). Dynamic performance of a modular multilevel back-to-back HVDC system. *IEEE Transactions on power delivery*, 25(4), 2903-2912.
- [8] Quach, N. T., Ko, J. H., Kim, D. W., & Kim, E. H. (2014). An Application of Proportional-Resonant Controller in MMC-HVDC System under Unbalanced Voltage Conditions. *Journal of Electrical Engineering & Technology*, 9(5), 1746-1752.
- [9] Quach, N. T., Lee, D. H., Kim, H. C., & Kim, E. H. (2015). Analyzing stability of jeju island power system with modular multilevel converter based HVDC system. *Journal of Electrical Engineering & Technology*, 10(1), 47-55.
- [10] Vidal-Albalade, R., Beltran, H., Rolán, A., Belenguer, E., Peña, R., & Blasco-Gimenez, R. (2016). Analysis of the Performance of MMC Under Fault Conditions in HVDC-Based Offshore Wind Farms. *IEEE Transactions on Power Delivery*, 31(2), 839-847.
- [11] Wang, P., Zhang, X. P., Coventry, P. F., & Zhang, R. (2016). Start-up control of an offshore integrated mmc multi-terminal hvdc system with reduced dc voltage. *IEEE Transactions on Power Systems*, 31(4), 2740-2751.
- Scott, N. C., Atkinson, D. J., & Morrell, J. E. (2002). Use of load control to regulate voltage on distribution networks with embedded generation. *IEEE Transactions on Power Systems*, 17(2), 510-515.

ECBA-17

Status of High Temperature Superconducting Motor for Electric Ship Propulsion

Jae Hyung Moon¹, Chang Ju Hyeon², Seho Kim³, Ho Min Kim^{4*}

^{1,2,3,4} Department of Electrical Engineering Jeju National University, South Korea

Abstract

Nowadays, ship propulsion system equipped with various electrical motors is replacing the mechanical ship propulsion using diesel engines in the worldwide to improve the power density and efficiency of ship operation. For maximization of the advantages of electric propulsion system, many research and developments for high temperature superconducting (HTS) motor are underway. Electric propulsion system applied HTS motor, which allows the volume and weigh reduction of propulsion motor due to high current density of HTS conductor, can obtain high driving force because of its compactness. This paper will describe the fundamentally technical explanations of HTS motor and a summary of recent development trends of large scale HTS motor for electric ship propulsion systems in the worldwide.

© 2017 The Authors. Published by Academic Fora. This is an open access article under the CC BY-NC-ND license

(<http://creativecommons.org/licenses/by-nc-nd/4.0/>)

Peer-review under responsibility of the Scientific & Review committee of ECBA- 2017.

Keywords— Electric Propulsion, High Temperature Superconducting, Electric Motor, High Current Density

Introduction

The propulsion of merchant shipping has, during the last century, undergone a significant transformation. It is now dominated by diesel propulsion machinery with the cost of fuel accounting for a large proportion of the running costs of the ship. Against this background, recent developments have led many things in the industry to question whether the present modes of ship propulsion are sustainable due to three main factors:

- Rising fuel costs as a result of the escalating price of oil
- Environmental regulations introduced to mitigate the effects of climate change
- The potential introduction of carbon taxes

Conventional propulsion systems to generate the required force are using diesel engines. And in scientific investigation about electrical propulsion systems, the shipping companies do not have any interest to order the electrical ships. So aim of this paper, by showing the advantage of electric propulsion systems, is encourage them to use electrical ships. As we can see in the Table 1, it shows that the international shipping is estimated to contribute some 6% of UK emission CO₂ [1].

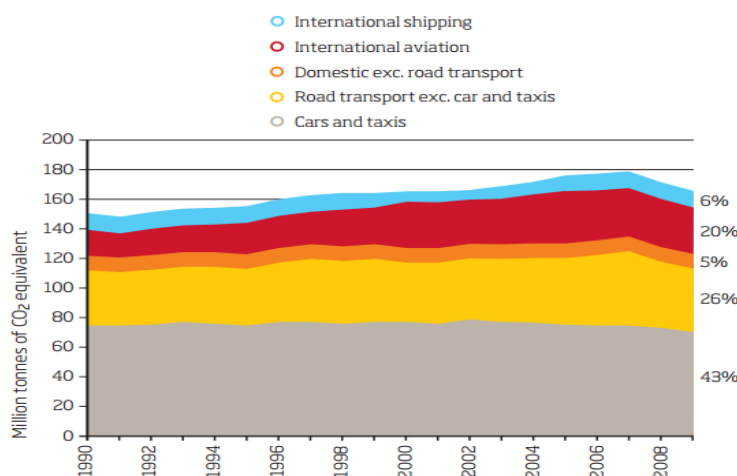


Figure 1: Total UK transport greenhouse gas missions: 1990-2009

*All correspondence related to this article should be directed to Ho Min Kim, Jeju National University, South Korea

Email: borissan@naver.com, gcw1031@naver.com

© 2017 The Authors. Published by Academic Fora. This is an open access article under the CC BY-NC-ND license

(<http://creativecommons.org/licenses/by-nc-nd/4.0/>)

Peer-review under responsibility of the Scientific & Review committee of ECBA-2017.

Study for using of superconductivity technology have been started since 1970th and 1980th by manufacturing some generator that they used low temperature superconductors (LTS) this project reached new borders. At first this technology implement in DC machines, although this project never reached the industrial level but this was a good start point. Main problem of LTS technology is low operating temperature that needs complicated cooling system.

With the advent of high-temperature superconductor (HTS) materials, hopes of commercialization of superconducting motors, because of high operating temperature of used material and consequently use of liquid nitrogen in cooling system, have been increased. Since the electric propulsion motors in terms of volume and power consumption have significant part, designers tend to increase compression and efficiency of electric propulsion motors. For these goals HTS motors are the best choice because besides those two advantages, the ability to control the speed of HTS motors are the same as conventional electric motors, and HTS propulsion motors can be used in any types of ships and vessels. Main advantages of HTS motors are [2, 3];

- The density of the HTS motor torque is three times more than conventional motors. It was far less weight and volume that makes transport, installation and positioning of them easier.
- HTS motors have high efficiency from low speed up to rated speed.
- Noise of HTS motors are less than conventional motors.

Principle and Configuration of the Hts Motor

Motor refers to a power unit for converting electrical power to mechanical power generating rotational torque generated by the interaction of the field with the Fleming's left-hand rule based armature to produce the mechanical power. In general, a runner in the field to produce a rotary system is used in a designated shape corresponding to the armature and stator to produce a rotating magnetic flux in the rotor. Existing normal-motors have become an obstacle to the output capacity and performance because of the high magnetic saturation characteristic of an iron core. In contrast, superconducting motors, the energy density is raised by action of copper and a permanent magnet used in the field of conventional motor with a superconducting wire with no electric loss, lower size, weight, high output and high efficiency.

Figure 2 shows a comparison of the efficiency and size of the 4 MW class motor with the same motor production capacity of the German SIEMENS Corporation. If the motor to replace the traditional high-temperature superconducting motor normal-contrast weight for the same motor output is about 33% lighter in size, it can increase the efficiency of 1.5 to 2.3% at the same time reduced by 40% [4].

Figure 3 shows a schematic diagram of a 5 MW-class American AMSC's superconducting motor. Superconducting field winding (Super-conductor Rotor Coil) is an integral part of the rotor, the supply is received to superconducting electromagnet from an electric exciter (Exciter). Damper (Electromechanical shield) is installed for the purpose of shielding corresponds to block the disturbance applied to the superconducting field coil by the external magnetic fields change. Armature (copper stator coil) is responsible for generating the alternating magnetic field to produce an alternating current flows through the rotational torque. Cryogenic and cryogenic cooling system for cooling the environment maintained for other superconducting field winding is constructed of a vacuum cooling tank (vacuum chamber).

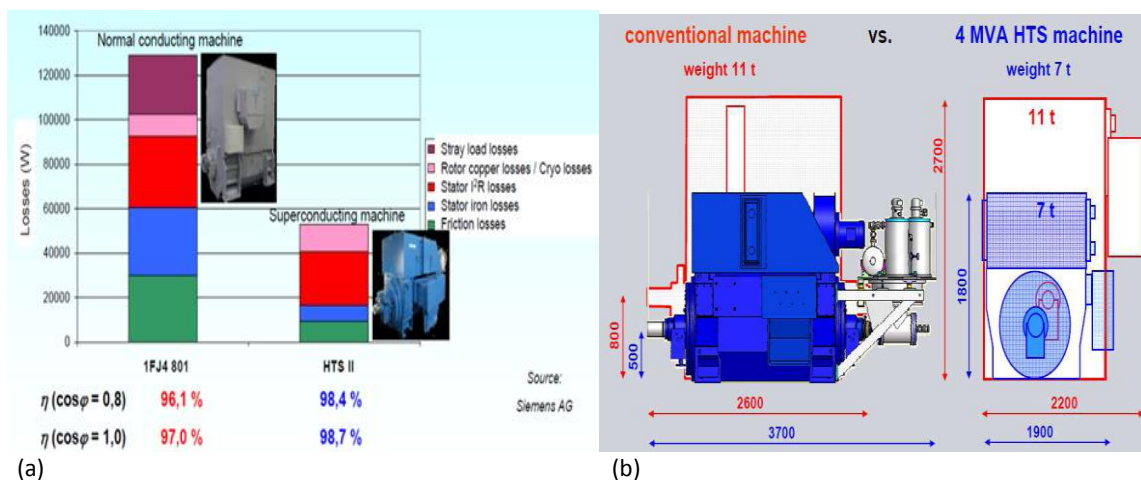


Figure 2: A 4 MW class superconducting and normal conducting motor (a) efficiency and (b) size comparison

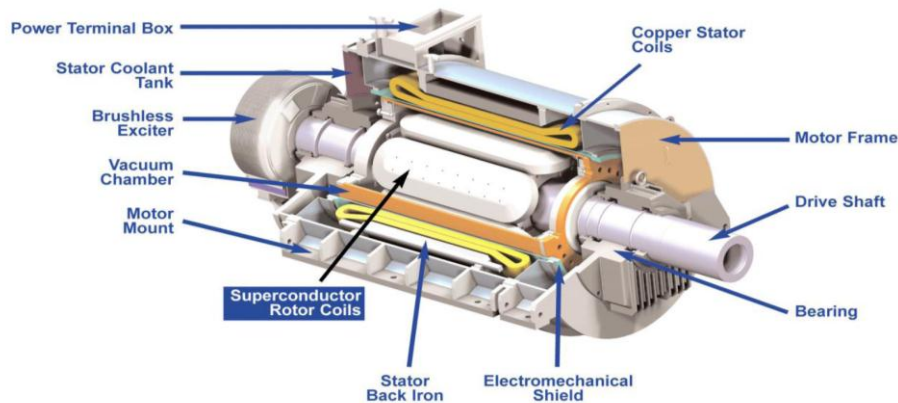


Figure 3: A schematic diagram superconducting motor [AMSC 2009]

Hts Motor Skills Development Trends

Many countries have developed since the early 1990s and has demonstrated the 1~ 100 MW class superconducting rotating machines. Recently Global Major suppliers of SIEMENS and AMSC own proprietary technology focused mainly on generator and marine generator, motor development for wind power generation concentrating. Figure 4 shows the superconducting rotating machine development trend.

High-temperature superconducting motor is currently under development for industrial-MW. And more large ship propulsion and electric motor for the purpose of the majority and the small-capacity motor for electric vehicle research and development are being made in some companies aim to improve efficiency. Recently, there is a purpose of the research and development to be applied to the aircraft based on the conventional superconducting electric motor development and manufacturing technology is attempted.

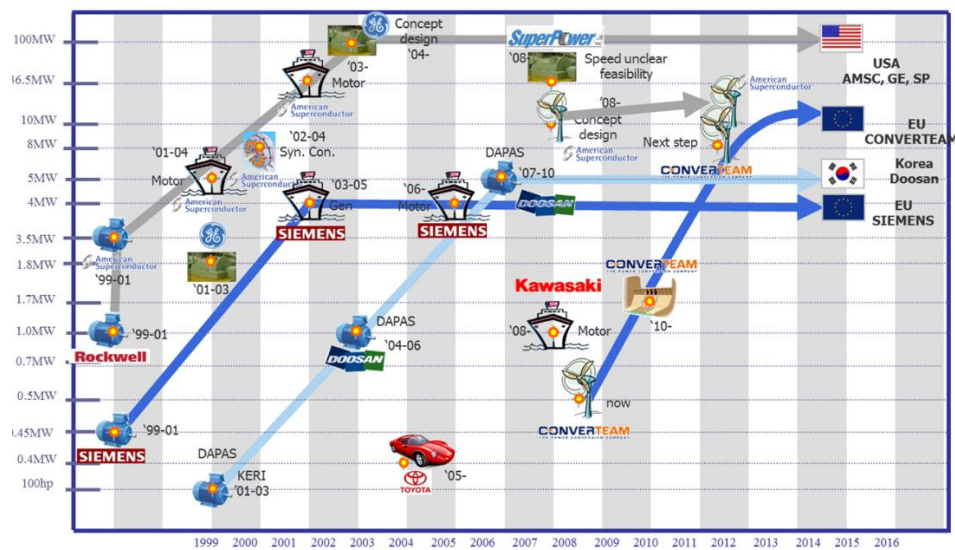


Fig. 4. Superconducting rotating machine development trend around the world

Hts Ship Propulsion Sector

At present, because of their high efficiency, most ship engines are diesel; however, given the above environmental situation in the field of maritime transport, future ship propulsion systems are envisaged to be quite different from those of the present. Electric ship propulsion using various available energy sources is one of the prospective substitutes for conventional ship propulsion systems. In order for its use to expand, innovative technologies for the reduction of electric power transmission loss are required. Using high-temperature superconducting (HTS) technology has the potential for a drastic reduction of electric power transmission loss. Electric pod propulsion has recently become popular for large cruisers and platform supply vessels because of the increased flexibility of the equipment arrangement and the stern hull design, leading to better maneuverability. For this reason, HTS motors for pod ship propulsion are being developed [5].

American Superconductor – AMSC (America)

High temperature superconducting motor which is the first marine electric propulsion system is the most influential in the field applied to mention, AMSC, SIEMENS, perceiving the development trend of the advanced developer, such as IHI This can be clearly seen that in the electric propulsion system by replacing an existing vessel and a generator motor to a superconducting device, the loss rate is lowered to 10% or less. The expected benefit of increasing propulsion efficiency of a ship, weight and energy loss in the size of the propulsion system is reduced than the conventional diesel engine, it is possible to increase the flexibility and shipping space utilization of the ship design. Also part of the warships and cruise lines promote high value-added objectives [6]-[7].

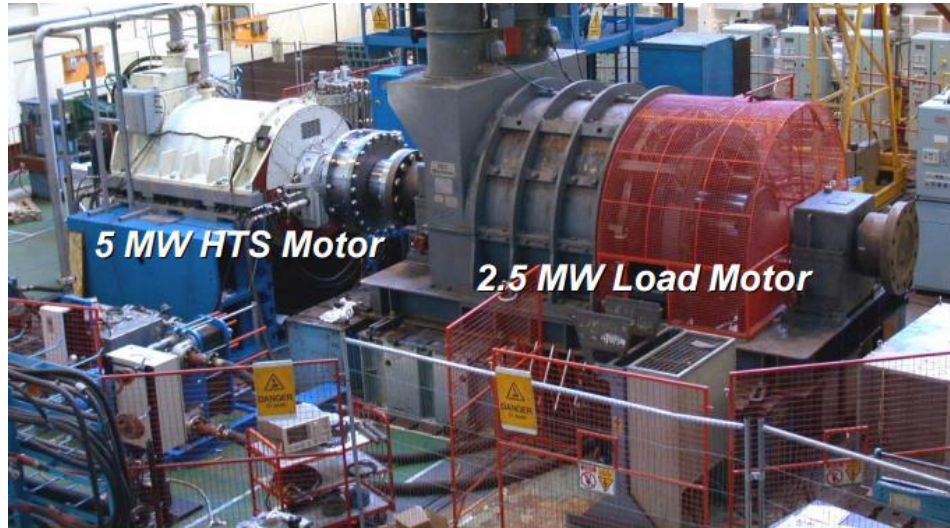


Figure 5: MW ship propulsion motor test results

In 2001 using a first-generation high-temperature superconducting wire in BSCCO wire on the field winding 30 K at an operating temperature of refrigerant neon with SIEMENS of Germany in Europe, first in class 400 kW / 1500 rpm succeeded in making a superconducting motor. During the six-month test motor mode via UPS devices combined generator mode tests were successfully carried out in connection with the power grid. For ship propulsion in 2005 with the support of the BMBF grade 4 MVA / 3600 rpm to complete the development of superconducting generators were currently 16 MVA.

It has developed for the class generator. In addition, during the load test developed grade 4 MW / 120 rpm motor ships, the motor has been used by a high-temperature superconducting wire in a superconducting system with 45 km, 8-pole, outputs of 4 MW and the rated efficiency of 96.2%.

Research is underway in the United States most active in this field, it holds the world leading technology. Developer of superconducting wire and AMSC live by DOE's support SPI (Superconductivity Partnership Initiative) program through Phase 2 hp 5000 and succeeded in developing high-temperature superconducting motor mounted on a ship from the ONR (Office of Navy Research) of the US Navy in February 2002 to 5 MW. It signed a contract to supply high-temperature superconducting motor 230 rpm to \$ 8,000,000 in the United Kingdom after the performance evaluation as ALSTOM Inc. in 2003, the state delivered to the US Navy. Figure 5 shows a picture of the performance test of 36.5 MW class high-temperature superconducting synchronous motor. It has the large capacity of 36.5 MW of the superconducting rotating machine with efficiency of 97%, 3.4m (length) × 4.6m (width) × 4.1m in size and has a weight of 75 tons. If the motor has been applied, it will be estimated fuel saving of 1 million dollars annually.

Japan

In 2005 Japan superconducting motors for ships (liquid nitrogen cooled) was developed by the Academic Group, including Sumitomo majors. In addition, the double reverse, connected the two superconducting motors in series propulsion system were also designed test. Liquid nitrogen-cooled motor is developed by the motor with a capacity of 400 kW up to now. Subsequently, the gas was cooled to develop a superconducting motor of the New Energy and Industrial Technology with the support of the development of energy-saving energy innovations Development Organization (NEDO) as Kawasaki Heavy fuel economy improvement of about 20% 3 MW in 2013. Here, the coil windings by Sumitomo major DI-BSCCO-type was used as a race track [8].



Figure 6: 1 MW class superconducting motor for ship propulsion of Kawasaki

Kawasaki Heavy Industries Ltd has been undertaking prototype development of an HTS motor with a low rotating rate for commercial use since 2007. The motor's output reached 450 kW at 190 rpm with an outstanding efficiency of 98% in 2010. Subsequent development of a 3MW HTS technical demonstrator is being conducted. The testing of the long-term operation and endurance of the HTS motor against varying external loads is planned from the fiscal year 2013 to fiscal year 2014. After that, final verification will be needed via an actual ship test for practical use.

Korea

Korea's Doosan Heavy Industries & Construction is developing 75 kW class in the first step under the Institute of Electrical and Cooperation to participate in superconducting applications technology development project (DAPAS) / 1800 rpm the motor development was succeed in 2004 with the first-generation high-temperature superconducting wire, which promoted from second step 1 MW class.

Its 3600 rpm superconducting motor development were successful (2007). In the final third step completed in March 2011, to develop high-performance / low-cost superconducting motors the 5 MW class superconducting 213 rpm motor development were completed for ship propulsion.

Doosan Heavy Industries & Construction business move through the gap between the foreign advanced technology companies and has been evaluated as significantly narrowed reach the leading group level by securing the various techniques for the commercialization of superconducting motors.

Doosan Heavy Industries & Construction has been building a long-term reliability testing and evaluation of various possible load and test facilities to house up to 6 MW [9].

China

Supported by China Ministry of Science & Technology and designed by WIMEP, the project of 1MW, 500rpm HTS motor was initiated in Dec. 2008. The main technical parameters include the following:

- a) Power: 1000kW
- b) Speed: 500rpm
- c) Efficiency: 95%

And also the project needs to finish the following goals a) HTS magnet technology b) Topology structure of the rotor c) Air gap armature d) Cryogenic refrigeration system.

The test of the demonstration 1MW HTS motor was finished in April 2012 at WIMEP as shown in Fig 7. The test indicated that the performance reached design requirements. The demonstration motor was validated both the overall design and component design for large capacity HTS motor [10].

Table 1:

Parameters for 1MW HTS Motor

Parameter	Value	Units
Nominal rating	1	MW
Rated Voltage	690	V
Rated current	950	A
Power factor at rated load	0.9~1	
Rated speed	500	r/min
Frequency at rated speed	16.67	Hz
Exciting current of field winding	85	A
Air-gap flux density	0.85	T



Figure 7: 1MW HTS motor test bed

Conclusion

In the field of maritime transport, international environmental regulations are tightening. Against these regulation changes, an HTS motor with the characteristics of high torque and compactness can become the key device for a high-performance and low-emission electric ship propulsion system. One example of such high-performance and low-emission electric ship propulsion is the pod ship propulsion system. Pod ship propulsion with an HTS motor becomes more slender than that with a conventional motor.

Acknowledgement

This research was financially supported by The Project Management Center Cultivating Smart Grid & Clean Energy Manpowers(CK-I), JNU

References

- [1]. Carlton, J., Aldwinkle, J., & Anderson, J. (2013). Future ship powering options: exploring alternative methods of ship propulsion. *London: Royal Academy of Engineering*.
- [2]. Barnes, P. N., Sumption, M. D., & Rhoads, G. L. (2005). Review of high power density superconducting generators: Present state and prospects for incorporating YBCO windings. *Cryogenics*, 45(10), 670-686.
- [3]. Maki, Naoki, Tomoaki Takao, Shuichiro Fuchino, Hiromichi Hiwasa, Masazumi Hirakawa, Kagao Okumura, Minoru Asada, and Ryuukichi Takahashi. "Study of practical applications of HTS synchronous machines." *IEEE transactions on applied superconductivity* 15, no. 2 (2005): 2166-2169.
- [4]. Frank, M., Van Habelt, P., Kummeth, P., Masek, P., Nick, W., Rothfischer, H., ... & Fraunhofer, J. (2006). High-temperature superconducting rotating machines for ship applications. *IEEE transactions on applied superconductivity*, 16(2), 1465-1468.
- [5]. Nishijima, S., Eckroad, S., Marian, A., Choi, K., Kim, W. S., Terai, M., Deng, Z., Zheng, J., Wang, J., Umemoto, K. & Du, J. (2013). Superconductivity and the environment: A roadmap. *Superconductor Science and Technology*, 26(11), 113001.

- [6]. Snitchler, G., Gamble, B., & Kalsi, S. S. (2005). The performance of a 5 MW high temperature superconductor ship propulsion motor. *IEEE Transactions on Applied Superconductivity*, 15(2), 2206-2209.
- [7]. Gamble, B., Snitchler, G., & MacDonald, T. (2011). Full power test of a 36.5 MW HTS propulsion motor. *IEEE Transactions on Applied Superconductivity*, 21(3), 1083-1088.
- [8]. Ueno, E., Kato, T., & Hayashi, K. (2014). Race-track coils for a 3MW HTS ship motor. *Physica C: Superconductivity and its Applications*, 504, 111-114.
- [9]. American Society of Cinematographers. (2014). *Introduction to DOOSAN HTS motor*.
- [10]. Jun, Z., Feng, X., Wei, C., Yijun, D., Jin, C., & Wenbin, T. (2012). The study and test for 1MW high temperature superconducting motor. In *Proc. IEEE/CSC ESAS Eur. Supercond. News Forum* (No. 22, pp. 1-4)

ECBA-17

The Plan and the Present Status Constructing Chargers to Promote Ev Penetration in the Jeju Island

Hee-Jeong Ko¹, Su-Wan Kim², Ankhzayabaatarbileg³, Kyu-Ho Park⁴, Hoonkwon⁵, Gae-Myoung Lee^{6*}

^{1,2,3,5,6} Jeju National University, 102 Jejudaehak-ro, Jeju-si63243, South Korea

⁴ Korea Electric Vehicle Charging Services, 61, Yeonsam-ro, Jeju-si, Jeju-do 63148, South Korea

Abstract

The provincial government of the Jeju Island made the plan realizing the Jeju Island into a carbonfree region by the 2030 year and has been trying to carry it. An important sub-plan in order to construct the carbon-free island is to penetrate EVs(electric vehicles) in the island. The EV penetration plan is scheduled to replace 30% of the vehicles with EVs by the 2020 year and 100% of the vehicles with EVs by the 2030 year. In order to penetrate EVs smoothly in the island based on the plan, providing EV chargers in many places must precede. In this paper, we will introduce the plan constructing EV charging infrastructure of the Jeju provincial government and the present status of chargers provided in the respective regions, and discuss the recent change of the policy constructing the EV charging infrastructure and its reasons.

© 2017 The Authors. Published by Academic Fora. This is an open access article under the CC BY-NC-ND license (<http://creativecommons.org/licenses/by-nc-nd/4.0/>)

Peer-review under responsibility of the Scientific & Review committee of ECBA- 2017.

Keywords— Electric Vehicle Charger, Electric Vehicles(EV), Carbon-Freejeju

Introduction

In 2012, the provincial government of the Jeju Island made the plan for the project that is "carbon-free Island Jeju by 2030". The aim of this project is to change Jeju city into smart grid one of Jeju by 2030, to achieve energy independence through the supply of new and renewable energy and to convert all vehicles into electric vehicles. The provincial government of the Jeju Island plans to replace the vehicle with electric vehicle to 10% by 2017, 30% by 2020, and 100% by 2030.

In order to achieve the electric vehicle supply project, the charger must be provided. Therefore, in this paper, we will report on the plan and the present status constructing chargers to promote EV penetration in the Jeju Island.

Table 1:

Types and Features of Ev Chargers

Types/Item	Home	Standard	Quick
Power level	≤3[kW]	≤7.7[kW]	≤50[kW]
Charging voltage	AC 220V	AC 220V	<DC 500V
Location	Home garage	Apartment, Public parking lot	Public parking lot, Electric Vehicle Only
real-time payment	Impossible	Possible	Possible

Types of Electric Vehicle Charger

Depending on the using purpose, there are three types of chargers: a home charger, a standard charger, and a quick charger. The home charger has output of 3kw and the charging voltage is AC 220V. The majority of the provided sites are houses and company's parking lots and the home charger occupies more than 90% of the estimated share of total electric vehicle charger. Unlike standard charger and quick charger, real-time payment is not provided in the home charger.

The standard charger has an output of about 7.7kW and has a charging voltage of AC 220V as well as a home charger. It is common in public roads and public parks, and estimates to be 7 to 8% of electric vehicle chargers. In addition, unlike home chargers, real-time payment is available.

*All correspondence related to this article should be directed to Gae-Myoung Lee, Jeju National University, 102 Jejudaehak-ro, Jeju-si63243, South Korea

Email: myoungik@jeju.ac.kr

© 2017 The Authors. Published by Academic Fora. This is an open access article under the CC BY-NC-ND license




(<http://creativecommons.org/licenses/by-nc-nd/4.0/>)

Peer-review under responsibility of the Scientific & Review committee of ECBA-2017.

Finally, the quick charger has an output of about 50kW and has a charging voltage of less than DC 500V, unlike the mentioned chargers earlier, it also has a exclusive charging station and expects to be a share of 1 to 2% of total electric vehicle chargers.

Table 2:

Charger Classification According To Installation Types

Fixed Charger		Portable Charger
Wall-mounted charger	Stand type charger	
		

Charger Classification According to Installation Types

Electric vehicle charger can be divided into mobile type and fixed type depending on the types of installation and use, and the fixed type chargers can be divided into the wall type and the stand type depending on the type of installation.

Table 3:

Types and Features of Ev Quick Charging

	DCCHAdEMO	DC combo	3 phase AC
Features	<ul style="list-style-type: none"> It is possible to distinguishing between standard and quick socket. Low radio interference. 	<ul style="list-style-type: none"> It is possible to emergency quick charge. 	<ul style="list-style-type: none"> Technology to protect battery and power grid from electrical disturbance (galvanic) is applied.
Disadvantage	<ul style="list-style-type: none"> Charger bulky It takes a long time to charge. 	<ul style="list-style-type: none"> In case of standard charging it takes longer time than the others. 	<ul style="list-style-type: none"> Difficult to raise charger output more than 20kW. Charger installation cost high.

Electric Vehicle Quick Charging Types

There are three types of quick charging :DC CHAdEMO, DC combo and 3 phase AC in Korea. In the DC CHAdEMO, CHAdEMO is a compound word of 'charge' which means charging and 'move' which means movement. The shape of the plug changes with these charging types. Table 3 shows the features and disadvantages of them.

Current Status of Supplied EV Chargers in Korea 337 quick chargers is nationwide operating on September 2015 and the plan to install about 600 quick chargers by 2017 is executed.

Table 4:

Types of Quick Charger that are Provided by Ministry of Environment to the Jeju Island

Charge type/ Company Name	Quick	
	DC CHAdEMO+ 3 phase AC	DC CHAdEMO+ 3 phase AC+ DC Combo
Ministry of Environment	20	29

Current Status of the EV Quick Chargers that are Provided by Ministry of Environment to Jeju Island

Recently, when looking at the direction of penetration of chargers in South Korea, it focuses on penetration of quick chargers rather than standard chargers. Central government (Ministry of the Environment) is providing for quick chargers and standard chargers in Jeju area, that is provided to electric vehicle purchasers. Applicants who purchase electric vehicles can be received one of 3 charger types :wall-mounted type, stand-type and mobile type standard chargers. By 2016, the Ministry of Environment provided 20 quick charger that is composed of DC CHAdEMO and 3 phase AC, 29 multi-type quick chargers including 3 phase AC, DC CHAdEMO and DC combo. But the Ministry of Environment didn't provide Jeju with quick charger during 2016 year.

Table 5:

Status of Chargers that are Provided by Private Enterprises to Jeju Island

Charger Type Company Name	Quick					Standard
	1. DC CHAdEMO	2. 3 phaseAC	3. DC Combo	1+2+3	1+3	Standard
Biggins Jeju	0	0	0	5	0	4
KEPCO	2	0	0	1	0	15
KEVCS	0	0	0	43	0	37
POSCO ICT	0	0	0	2	0	64
total	2	0	0	51	0	120
	53					120

Current Status of EV Chargers that are Provided by Private Enterprises to JeJu Island

Private enterprises that supply chargers to Jeju Island include Begins Jeju, KEPCO(Korea Electric Power Corporation), Korea Electric Vehicle Charging Service Co., Ltd. and POSCO ICT and so on. At the time of October 2016, as shown in Table 5, chargers to be installed by private enterprises mainly are standard chargers. Looking at the overall figures, Biggins Jeju has been providing 4 standard chargers and 5 multi-type quick chargers including DC CHAdEMO, 3 phase AC and DC combo plug type.

KEPCO is providing 2 quick chargers of DC CHAdEMO type, 1 multi-type quick charger and 15 standard chargers. In Korea's Electric Vehicle Charging Service, it occupies the most penetration rate among private enterprises. It has 37 standard chargers and 43 multi-type quick chargers. Finally, the POSCO ICT is providing 64 standard chargers and 2 multi-type quick chargers. Therefore, the overall supply status of the charger in the private enterprises has been providing 53 quick chargers and 120 standard chargers.

Table 6:

Status of Chargers that are Provided by Private Enterprises to Jeju Island

Yearly	Quick				Standard				Remarks
	Test-bed Project	Public Institutions	Private Operator	Total	Public Institutions	Private Operator	Private Operator	Total	
~13	23	39	4	66	154	101	157	412	-
14	-	10	4	14	19	25	481	525	-
15	-	-	31	31	19	32	1,481	1,469	-
16	-	-	65	65	25	3,924		3,989	During Statistical Analysis (Planning)
Total	23	49	104	176	217	6,201		6,395	-

The Overall Current Status of The EV Charger Supplied to Jeju Island

By 2013, there were 66 quick chargers and 412 standard chargers in JeJu. In 2014, 14 quick chargers and 525 standard chargers were installed, and in 2015, 31 quick chargers and 1469 standard chargers were provided. In 2016, it plans to provide 65 quick chargers and 3,989 standard chargers, and is currently under statistical analysis.

Table 7:

Status of Chargers That Are Provided By Private Enterprises To Jeju Island

Yearly	Standard				Quick		
	Public Institutions	Individual	Private Fee	Total	Public Institutions	Private Fee	Total
2017	25	13,906	40	13,971	-	40	40
~2020	75	17,803	7,646	25,524	-	1,079	1,079
~2030	322	33,397	7,882	41,601	-	3,011	3,011

Supply Plan of EV Charger In JeJu Island

There is a plan to expand the electric vehicle charger as the electric vehicle expands. The plan's chargers are planned mostly a home charger(slow charger) that is provided electric vehicle buyers. However, recently, it is expected that the charger supply plan will need to be changed as the policy decision that it is necessary to construct a charging infrastructure focused on quick charger is agreed. A total of 41,601 chargers will be installed by 2030, when the current project is to complete the carbon-free Jeju island project.

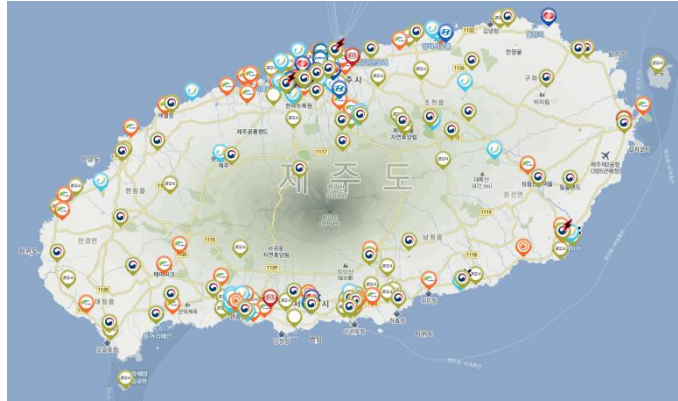


Figure 1: .Locations of EV charger in Jeju Island(2017/01/03)



Figure 2: Locations of EV quick charger in Jeju Island(2017/01/03)

Locations of EV Charger In Jeju Island

Figure 2 shows the position where the quick charger is provided. A new special plan is to build a centralized charging stations to supply effective charging service. They have 5 quick chargers in a place, and are being constructed at 4 places in Seongsan Ilchulbong, Seongsan Port, Yongmeori Beach parking and Hallim Gymnasium in Jeju. This plan which was scheduled to be completed in 2016 is delayed until 2017. Currently, on Jeju Island, 2 concentrated charging stations are set up at the government office building of Jeju Special Self-Governing Province and Jeju Stadium.

Conclusion

The provincial government of the Jeju Island made the plan realizing the Jeju Island into a carbonfree region by the 2030 year. An important sub-plan, in order to construct the carbon-free island, is to penetrate EVs(electric vehicles) in the island. The EV penetration plan is scheduled to replace 30% of the vehicles with EVs by the 2020 year and 100% of the vehicles with EVs by the 2030 year.

According to current “Electric Vehicle Comprehensive Plan of Jeju Special Self-Governing Province”, a total of 41,601 chargers will be provided by 2030.

The plan was formulated so that the penetration of electric chargers will be expanded. It was made at the assumption that a standard charger will be provided to an electric vehicle purchaser. However, currently, constructing charging

infrastructure focused on quick chargers in the public areas is recognized to be more effective and economic than installing a lot of standard chargers. It is judged that it is necessary to change the penetrating plan of the chargers.

Acknowledgment

This research was financially supported by The Project Management Center Cultivating Smart Grid & Clean Energy Manpowers(CK-I), JNU

References

- [1] EVCIS, (n.d). *Electric Vehicle Charging Information System* Retrived from , <http://www.ev.or.kr/portal/main>
- [2] Jeju Special Self-Governing Province, (n.d). *Electric vehicle comprehensive plan*, Retrived from, www.jeju.go.kr
- [3] Jeju Special Self-Governing Province, (n.d). “*Second half of 2016 EV supply business occasional recruitmentcollusion*”, Retrived from, www.jeju.go.kr
- [4] Son, S.H .(2016) *Jeju Electric Vehicle Supply Policy and Industry Trend*.
- [5] U.S. Environmental Protection Agency (n.d), *Fuel economy datafiles 2011-2013*. Retrieved from www.fueleconomy.gov
- [6] Choi, D.Y., Park, C.G., Kim, S. I., Joe, E. J., & Won, D. W. (2012). *Analysis of energy supply and demand for electric vehicle supply*. Korea Energy Economics Institute, South Korea
- [7] Bak,H.B. (2009). Effects of electricity supply and demand on electric vehicle supply and implications, KPX Report, Korea
- [8] Kim, M.S & Hong, S,G. (2014).Smart panel board for ev standard chargers and its control method. *The Transactions of the Korean Institute of Power Electronics*. 19(6),511-521

ECBA-17**Status of High Temperature Superconducting Motor for Electric Vehicles Propulsions**Kyu Seong Song¹, Ji Hyung Kim², Ho Min Kim³, Se Ho Kim^{4*}^{1, 2, 3, 4} *Department of Electrical Engineering, Jeju National University, S. Korea*

Abstract

Nowadays, the rapid development of electric energy storage system and motors has promoted the use of electric vehicles (EVs). As a result, a huge contribution of researches about EV has proceeded to reduce volume of machines and increase electrical efficiency in a variety of fields. Therefore, superconductivity technology is spotlighted for the high potential to improve the field of EVs. In this paper, the technology development trend on EVs system applied superconducting motors was researched and discussed.

© 2017 The Authors. Published by Academic Fora. This is an open access article under the CC BY-NC-ND license (<http://creativecommons.org/licenses/by-nc-nd/4.0/>)

Peer-review under responsibility of the Scientific & Review committee of ECBA- 2017.

Keywords— Dc Motor, Electric Vehicle, High Temperature Superconducting, Synchronous Motor

Introduction

The fossil fuels had been served as a cheap and a fundamental resource in the world before 1970s. However, after the oil crisis in 1973, it caused the international oil prices to surge [1]. Furthermore, to reduce the carbon emissions which are the result of using fossil fuels in the air, The Kyoto Protocol and Convention on Climate Change were adopted [2].

Moreover, the rapid development of electric energy storage system and motors has promoted the use of electric vehicles (EVs). As a result, a huge contribution of researches about EV has proceeded to reduce volume of machines and increase electrical efficiency in a variety of fields. Therefore superconductivity technology is spotlighted for the high potential to improve the field of EVs.

Comparing superconducting machines with conventional machines, their advantages are listed as follows [3].

- Higher power density
- Reduced mass
- Increase in machine efficiency beyond 99% by reducing power losses by as much as 50% over conventional machines
- High efficiency at all loads – down to 5% of full load
- Low noise
- Superior negative sequence capability
- Excellent transient stability
- Low synchronous reactance – small load angle
- Enhanced grid stability
- Low harmonic content
- Reduced acoustic noise

From this point, this research will consolidate the technology development trend analysis on EVs system applied superconducting motors.

Conventional Evs

Fig. 1. illustrates a conventional electric vehicle (EV) system. It is easily seen that each EV system composes of batteries, electrical traction motors, and transmission. The EVs are operated only by the traction motor such as permanent magnet synchronous motor (PMSM), induction motors (IMs), and etc. Furthermore, the battery system which supplies current to traction motors is chargeable from an external electric power grid.

*All correspondence related to this article should be directed to Se Ho Kim, Jeju National University, Korea

Email: hosk@jeju.ac.kr

© 2017 The Authors. Published by Academic Fora. This is an open access article under the CC BY-NC-ND license (<http://creativecommons.org/licenses/by-nc-nd/4.0/>)

Peer-review under responsibility of the Scientific & Review committee of ECBA-2017.

Nowadays, EVs have important strengths that are high fuel efficiency and no pollution than automobile with mechanical engine. Therefore, conventional EVs technology in the development of large EVs has the high potential on transportation development in the future [4]. However, conventional EVs have a few challenges such as motor's low efficiency at a low speed, large size and heavy weight of conventional traction motor which lead to short driving distances. The traction motors for EVs must respond to a wide range of operations from low speed driving to high speed driving and from low torque output for constant-speed cruising to high torque output for acceleration [5]. However, in case of PMSMs and IMs for traction motors, efficiency of them is poor at low driving speed. It makes difficult to manage the battery systems. So, novel material or technology are required to overcome above challenges. Superconductivity technology can be a good solution and alternative.

Superconducting Evs

Superconducting Motors

The high-efficiency motors such as superconducting motors will be a solution in energy saving of EVs system. There are two types of superconducting materials that can be used in motor applications. First, one is low temperature superconductor (LTS) operated in temperature between 4 and 18 K, the other is high temperature superconductor (HTS) operated in temperature between 20 and 77 K [6]. Superconducting coil which is fabricated by LTS or HTS wire is a key difference with conventional motor. It can be equipped with field or armature winding of motor. Superconducting coil is possible to overcome magnetic flux density over 2 T in motor's air-gap which is limitation of conventional motors because superconducting wire has zero resistance characteristic at specific cryogenic temperature which leads to high current capacity. In conclusion, it can be achievable to manufacture motors that have a compact volume and lighter weight than conventional motors. Moreover, it is possible to achieve low loss and high efficiency by reducing the excitation loss [5].

The limitation of this study will only focus on HTS motor, and a typical HTS motor is shown in Fig. 2. Technically, its rotor is composed of HTS field coils to generate the torque, a torque tube, and a rotating shaft. Torque is delivered from the torque tube to the rotating shaft and from the rotating shaft to the external propellers. Additionally, a flux damper and vacuum insulation layer for electromagnetically protecting the HTS field coil and preventing heat intrusion from room temperature, respectively, are installed. In addition, the air-core stator of the HTS motor consists of armature coils that are wound by conventional copper conductors such as Litz wire, stator supporters manufactured with fiberglass-reinforced plastic (FRP), and a magnetic shield that prevents the rotating magnetic field generated by the three-phase armature coils from leaking to the outside [7].

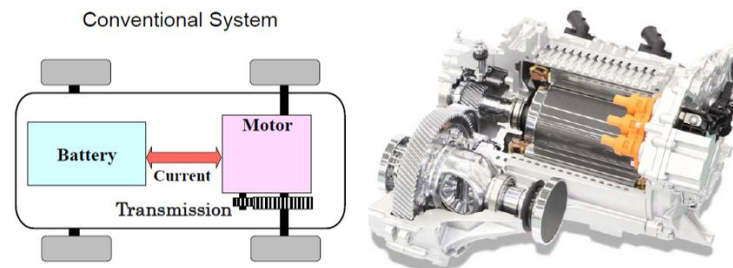


Figure 1: A conventional EV system

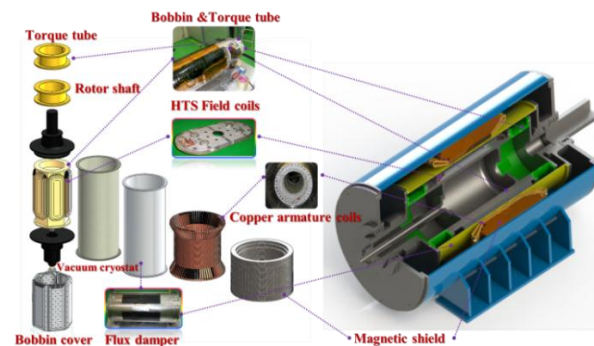


Figure 2: A cross-sectional structure of a typical HTS synchronous motor

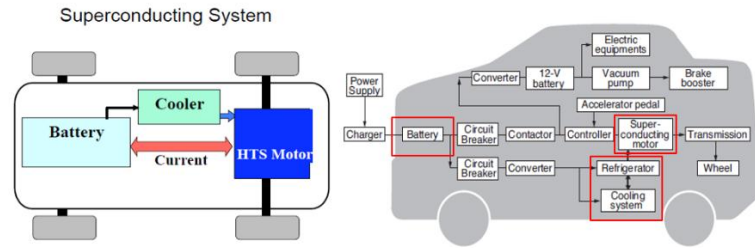


Figure 3: Configuration of superconducting EV system

EVs System with Superconducting Motor

Generally, the EVs system applying HTS motors is illustrated in Fig. 3. It basically consists of battery, HTS motor and cooling system including refrigerator. In addition, Fig. 4 shows the key advantage of HTS motors, we can easily see that HTS motors provide high efficiency over a wide torque-speed range. Moreover, the HTS coils provide a high magnetic flux density to air-gap in motor, and therefore, deliver much higher torque than conventional motors in same size. Furthermore, HTS motor can be used without copper loss, and HTS motor with air-core type may be developed in the future to reduce iron loss and increase motor efficiency. The high torque feature caused by high energy density of motors leads to the development of a system in which the motor directly drives a shaft without variable speed gears, and thus, results in the reduction of transmission loss caused by mechanical gear system [5]. It lets EVs without transmission to depart in slope and off-highway.

By using HTS motors in EVs, EVs make it easier to constantly get large torque and use energy from the battery efficiently, therefore, contributing to energy saving compared with conventional EVs.

Technology Development Trend Of Hts Evs

Superconducting EV by Sumitomo electric industries, Ltd.

Sumitomo Electric Industries, Ltd. (SEI) in Japan developed the small size superconducting motor first time in the world in 2008. It was successfully demonstrated to drive the electric passenger car as seen in Fig. 5. Fig. 6 shows configuration of HTS propulsion system for SEI' EV. Maximum motor power and torque was around 31 kW at 3100 rpm and 120 Nm at 1500 rpm, respectively. Moreover, This EV can drive to cruising distance of 60 km with constant speed of 30 km/h and maximum speed of EV was 85 km/h. The test driving results of HTS EV system is shown in Table 1 [5], [8].

Fig. 7 shows 31 kW class HTS DC motor mounted in EV system of SEI. The superconducting coils of motor were manufactured by DI-BSCCO HTS conductor as first generation HTS wire and were operated in liquid nitrogen with 77 K.

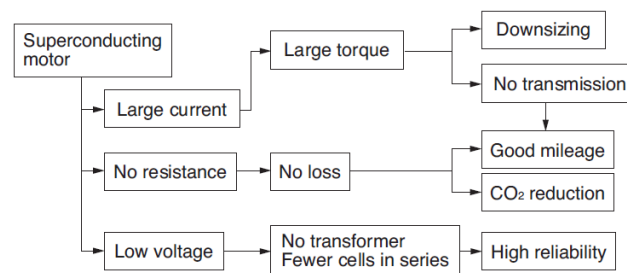


Figure 4: Advantage of superconducting motor in EVs system



Figure 5: Test drive of Sumitomo EV

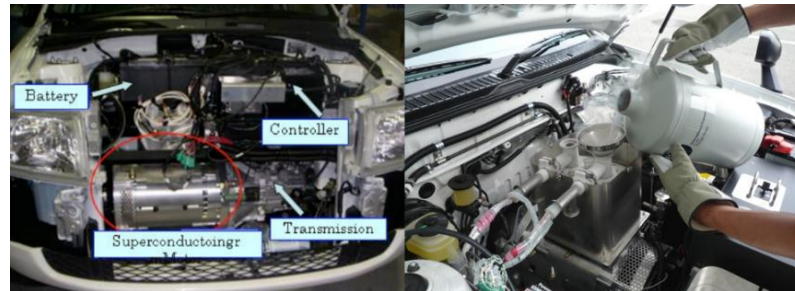


Figure 6: Configuration of HTS propulsion for EV system by Sumitomo

In 2012, HTS motor with a refrigerator is mounted on a Toyota Crown Athlete vehicle to verify its feasibility in a vehicle environment [5]. Fig. 8 shows an exterior view of the HTS motor with a refrigerator and configuration of HTS propulsion system for Toyota Crown Athlete vehicle. The HTS coil is immersed in liquid nitrogen in cryostat. Liquid nitrogen reservoirs are placed on the top of the motor. In operation, liquid nitrogen is provided first for pre-cooling, and then the refrigerator starts to cool down liquid nitrogen. When the temperature of liquid nitrogen is cooled below the boiling point (77 K), the evaporation of liquid nitrogen stops. Therefore, liquid nitrogen does not need to be refilled during the refrigerator operation [5]. Fig. 9 shows test drive of Toyota Crown Athlete EV equipped with SEI's HTS propulsion motor and Table 2 lists performance results of test driving. The maximum speed was 80 km/h, which is suitable for use in normal driving. As for the refrigerator cooling test result, the lowest temperature of 73 K was measured in HTS coils even though in a transition condition of EV [5].

Table 1:
Text Driving Result Of Hts Ev System By Sei

Quantity	Value
Maximum torque (1,500 rpm)	120 Nm
Maximum output (3,100 rpm)	31 kW
Maximum speed (3 rd gear)	85 km/h
Cruising distance (at 30 km/h)	60 km

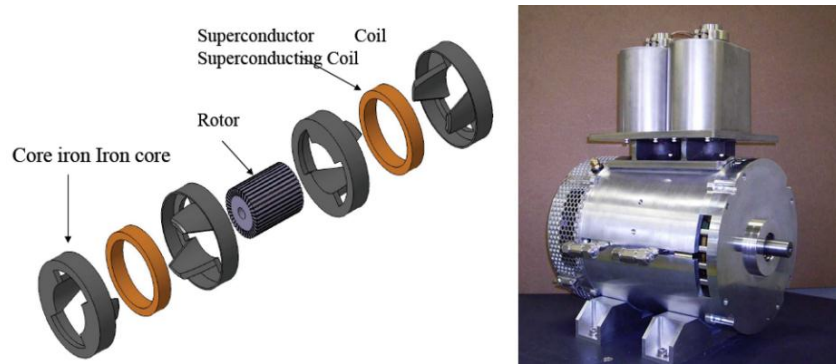


Figure 7: HTS DC motor for Sumitomo EV system

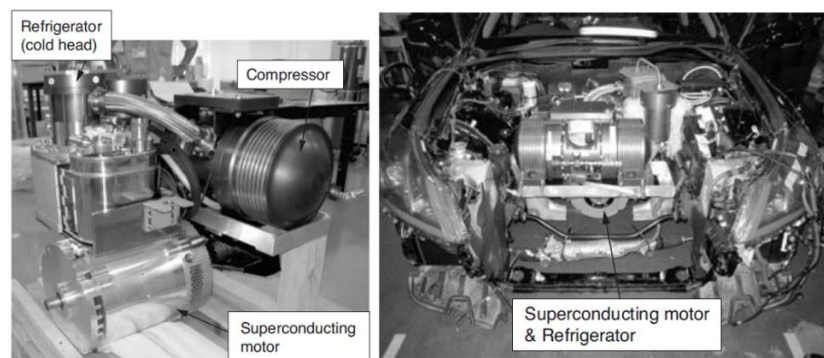


Figure 8: HTS motor with a refrigerator (left) and configuration of HTS propulsion system for Toyota Crown Athlete EV (right)



Figure 9: Test drive

Table 2:

Performance Test Result Of Toyota Crown Athlete Vehicle Of Hts Ev System By Sei

Quantity	Value
Maximum torque (1,540 rpm)	136 Nm
Maximum output (2,200 rpm)	30 kW
Maximum speed (4th gear)	About 80 km/h

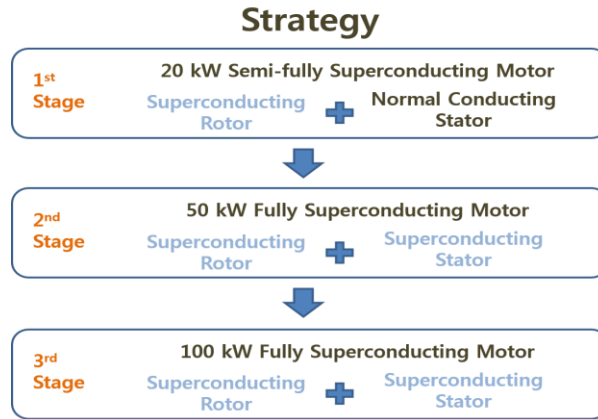


Figure 10: Development strategy of HTS motor by JST group

Superconducting Motor for EV by Japan Science and Technology Group (JST)

The JST is unification of Kyoto University, IMRA, AISIN, AIST and Niigata University. Fig. 10 shows strategy for superconducting motor for EVs system by JST group. They have total three stage for development of HTS motor and are finally planning to develop 100 kW class fully superconducting motor of EVs for large transportation. Moreover, technically, they focus on development of HTS induction-synchronous motor (HTS-ISM) because it has robustness against overload application by switching from the synchronous mode to slip mode [9]. In first stage of its research, the JST successfully developed 20 kW semi-fully superconducting motor that composes of superconducting rotor and conventional copper stator as seen in Fig. 11. According to [10], the purpose of first generation motor is the verification of JST's design technology. And they try to reduce the magnetic volume at 70% with the same power in second generation. Table 3 shows specification of 20 kW class HTS motor by JST group. Fig. 12 shows Final fabricated motor and test bench for 20 kW class HTS-ISM. The drive shaft of the fabricated motor is connected to the no-contact torque transducer and the load (permanent magnet) motor. The generated power due to the braking goes back to the HTS-ISM through the free-wheel diodes of the PWM inverter [10].

Fig. 13 shows the load test result of 2nd generation 20 kW class HTS-ISM at 77 K operating temperature. As can be clearly seen, rated power at synchronous speed of 1800 rpm reaches for the full load of 20 kW. Moreover, further application of the load (overload) transits the rotation mode of the HTS-ISM from the synchronous to the slip mode, and maximum output power at slip speed reaches for 26.8 kW. Namely, it can realize the overload tolerance with this motor. The power density is 1.38 kW/kg (this is calculated for the volume of the stator core).

From these results, it could be possible to realize the ultimate enhancement of the torque/power density for the next generation power-train system without any mechanical losses in transmission gears [9], [10].

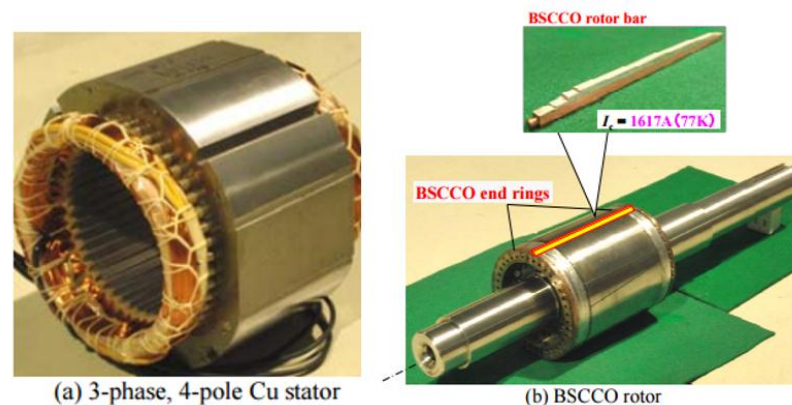


Figure 11: Photographs of Cu stator and BSCCO rotor for 20 kW class HTS-ISM by JST group in first stage

Table 3:
Specification of 20 Kw Class Hts-Ism By Jst Group

Items	1 st generation	2 nd generation
Output power	20 kW	20 kW
Rated voltage	400 V	200 V
Pole number	8	4
Maximum speed	1800 rpm	1800 rpm
Rotor's diameter	159.4 mm	119.3 mm
Stator's diameter	265.0 mm	200.0 mm
Length	200.0 mm	106.0 mm
Gap	0.60 mm	0.35 mm
Magnetic volume	11100cm ³	3330cm ³
Weight	83.9 kg	29.6 kg
Critical current of one rotor bar (stack number of BSCCO tapes)	2090 A (11)	1617 A (11)

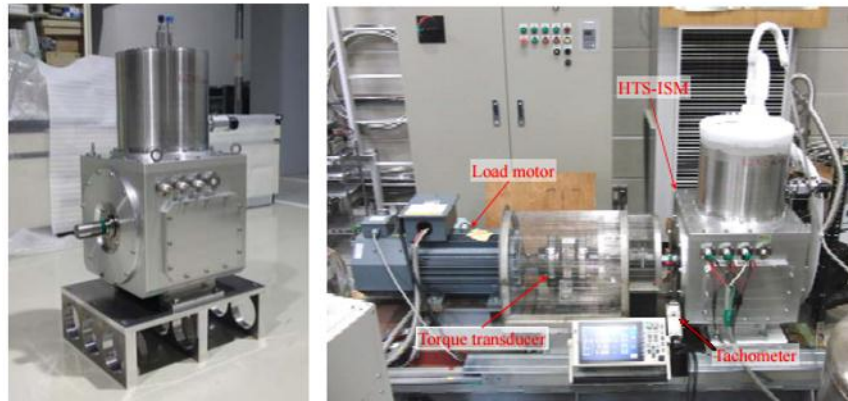


Figure 12: Final fabrication (left) and test bench for 20 kW class HTS-ISM (right)

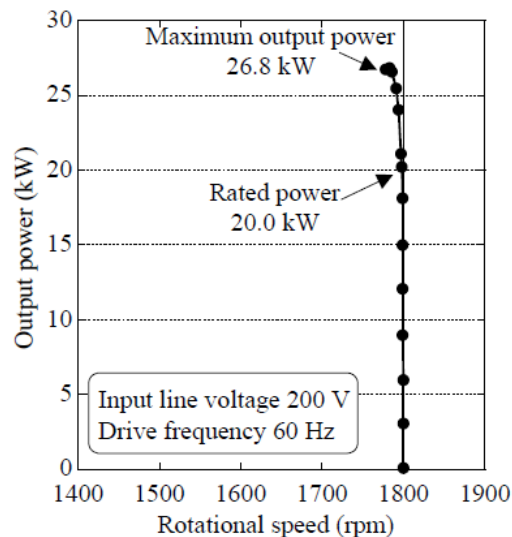


Figure 13: Load test results of 2nd generation 20 kW class HTS-ISM

Superconducting Motor for EV by Moscow Aviation Institute and Electro Power

Moscow Aviation Institute in Russia is focusing on development of 200 kW class HTS synchronous motor for electric bus. Fig. 14 shows construction of HTS rotor and conventional stator. Before the development of a 200 kW

HTS motor, they already have developed and successfully tested a 50 kW class synchronous motor. In 2016, they are planning to mount 200 kW class HTS motor to electrical bus for driving test [11].

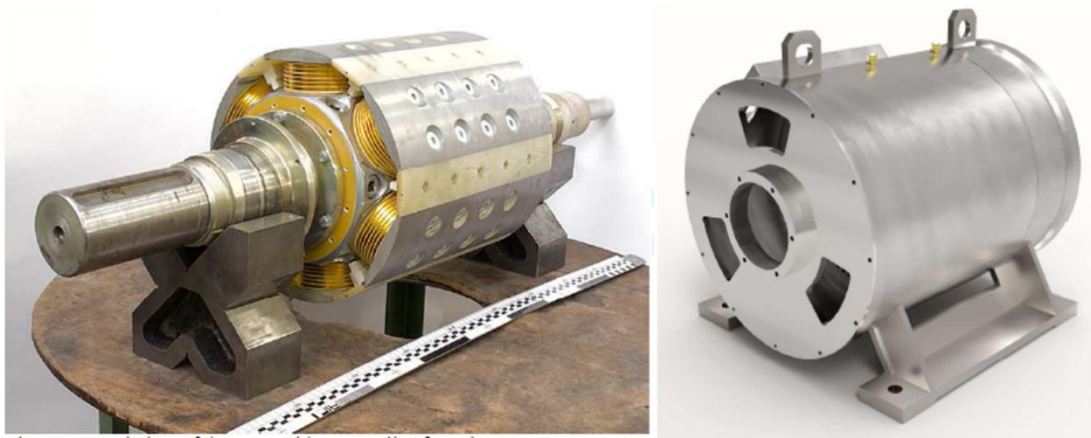


Figure 14: HTS rotor (left) and conventional stator (right) of 200 kW HTS motor by Moscow Aviation Institute

Conclusion

Superconducting EVs with the characteristics of high torque and efficiency become good alternative to overcome limitation of current EVs system with PMSM and IMs because it has a lot of advantages such as lighter weight, lower losses and etc. than that of. In near future, conventional EVs can be replaced with superconducting EVs system. Therefore, the EVs applied to superconductivity technology must be studied actively.

Acknowledgement

"This research was financially supported by The Project Management Center Cultivating Smart Grid & Clean Energy Manpowers(CK-I), JNU".

References

- [1] Pieprzyk, B., Kortlüke, N., & Hilje, P. R. (2009). The impact of fossil fuels. *Greenhouse gas emissions, environmental consequences and socio-economic effects* (pp. 98p): *Energy Research Architecture (ERA)*.
- [2] Secretariat, R. (2014). Renewables 2014 global status report. *REN21, Paris, Tech. Rep.*, 13-17
- [3] Gieras, J. F. (2009). Superconducting electrical machines-state of the art. *Organ*, 12, 1-20.
- [4] International Energy Agency. (2013). *Global EV outlook*.
- [5] Shinzato, T., Arakaw, S., Oyama, H., Saka, H., & Hayashi, T. (2012). Development of high-temperature superconducting motor for automobiles. *SEI Tech. Rev.*, 75, 62-65.
- [6] Zheng, L., Jin, J., Guo, Y., & Zhu, J. (2006). Technical and theoretical analysis of hts machines and their development. *Nature Sciences*, 1(1), 33-41.
- [7] Kim, J. H., Park, S., Le, T. D., Jo, H. C., Jo, Y. S., Choi, Y. H., ... & Kim, H. M. (2015). Analysis of the mechanical characteristics of a 17-MW-class high-temperature superconducting synchronous motor. *J. Supercond. Novel Magn.*, 28(2), 1671-679.
- [8] Hayashi, K. (2009, January). Development of HTS motor: Present status and future prospect. In *IEEE/CSC & ESAS European Superconductivity News Forum* (No. 7).
- [9] Li, Q. , Nakamura, T. , Shimura, H. , Nishimura, T. , Kitano, H., Misawa, S., Amemiya, N., Itoh, Y., Yoshikawa, M., Terazawa, T., Okumura, N., Furuse, M., & Fukui, S. (2013). Strategy and progress of fully superconducting induction/synchronous motors for environmental-friendly electric vehicles. Paper presented at the *23rd Int. Conf. Magnet Technol., Boston, MA, USA*.
- [10] Nakamura, T., Itoh, Y., Yoshikawa, M., Nishimura, T., Ogasa, T., Amemiya, N., ... & Furuse, M. (2015). Tremendous enhancement of torque density in HTS induction/synchronous machine for transportation equipments. *IEEE Transactions on Applied Superconductivity*, 25(3), 1-4.
- [11] Dmitry, D., Kovalev, K., Verzhbitskiy, L., Kozub, S., & Firsov, V. (2015). Design and testing of 200 kW synchronous motor with 2G HTS field rotor coils. Paper presented at *European Conference on Applied Superconductivity (EUCAS 2015)*.

ECBA-17**Contributiveness of PV Plants on Electric Power during Summer Peak Times in the Jeju Island**Suk-Young Ko¹, Su-Wan Kim², Ankhzaya Baatarbileg³, Gae-Myoung Lee^{4*}^{1,2,3,4} *Jeju National University, 102 Jejudaehak-ro, Jeju-si, South Korea*

Abstract

Both of introducing the RPS(Renewable Energy Portfolio Standard) system into the electric energy market in the 2012 year and reduction of the cost constructing PV(photovoltaic) power plants increased the number of MW PV plants in the South Korea. The Jeju Island is located at the center of South Korea, China and Japan and its provincial government declared that the island will be a clean region in which greenhouse gas do not emit by the 2030 year. And the Jeju provincial government is doing their best to penetrate the PV plants and wind farms. There are times in which electric energy cannot be generated by renewable energy sources such as solar and wind energies, though the power grid need the electric energy, because they change greatly according to weather conditions. It is important to know how much electric energy can be generated by the PV plants during the electric power peak times. In this study we investigated contributiveness of the MW PV plants on the power of the electric grid during the summer peak times in the Jeju Island. The biggest mountain in the South Korea, Mt. Halla, is located in the center of the Jeju Island and we divided the island into the 4 regions and analyses of total 24 PV plants carried out. The average contributiveness of the PV plants in the respective region on the electric power during the summer peak times was investigated and it compared with those of the other regions. The best contributiveness obtained in the PV plants of the west region and the value was 33% of the electric power capacity of the plants for recent 2 years

© 2017 The Authors. Published by Academic Fora. This is an open access article under the CC BY-NC-ND license
(<http://creativecommons.org/licenses/by-nc-nd/4.0/>)

Peer-review under responsibility of the Scientific & Review committee of ECBA- 2017.

Keywords— Photovoltaic Power Plants, Renewable Energy, Summer Peak Time, Contributiveness, Jeju

Introduction

In Korea, 97% of energy depends on the import. In the present situation of Korea, when we think about the future, electric power generation by renewable energy sources is important.

In the case of electric generation facilities, using renewable energy, such as solar and wind, they depends on weather. Therefore, they can't output as much as installed capacity during electric power peak time.

In the case of solar energy generation, it was not long PV power plants that started penetrating. But, its promotion from the country has been showing a sharp increase in supply because it receives more government support than other energy sources. Electric energy generated by a solar power plant is decided by the effect of weather and solar radiation. For this reason, the power supply may not be smooth. Solar power generation uses pollution-free energy, unlike other energy sources. For this reason, it does not produce wastes, and it doesn't cost big amount of money for fuel and doesn't cause air pollution as well. Also, it isn't noisy and its life is at least 20 years and maintenance is not difficult to sustain. However, the disadvantage of this is that its operation may be impossible depending on the weather and sun's own properties. Also, it has technological limitations. For example, non-uniform current generation occurs due to the intensity of solar radiation and if it dust accumulates, people should clean the solar generator.

In this study, knowing the contribution of PV power plants during summer power peak time, we investigated the amount of electric energy generated by them and electric power peak time during summer season. We analyzed the daily peak demand and electric power peak time of Jeju and the whole country from 2014 to 2016. And we tried to analyze of contributiveness of PV power plants in 4 regions of Jeju on the electric power of the electric grid during summer peak time.

Classification of Solar Power Plant in JEJU

We have classified solar power plants from north, south, east and west that close to Jeju Meteorological Observatory.

*All correspondence related to this article should be directed to Gae-Myoung Lee, *Jeju National University, 102 Jejudaehak-ro, Jeju-si, South Korea*
Email: myounglk@jeju.ac.kr

© 2017 The Authors. Published by Academic Fora. This is an open access article under the CC BY-NC-ND license

(<http://creativecommons.org/licenses/by-nc-nd/4.0/>)

Peer-review under responsibility of the Scientific & Review committee of ECBA-2017.

Table 1:

Current Status of Selection of Solar Power Plants in Jeju Region

Region classification	power plant	Capacity(MW)
Northern region of Jeju (Jeju meteorological observatory)	Northern A power plant	1.098
	Northern B power plant	1.208
	Northern C power plant	0.460
	Northern D power plant	0.990
	Northern E power plant	0.506
Eastern region of Jeju (Seongsan meteorological observatory)	Eastern A power plant	0.988
	Eastern B power plant	0.998
	Eastern C power plant	0.950
	Eastern D power plant	0.647
	Eastern E power plant	0.490
	Eastern F power plant	0.500
Southern region of Jeju (Seogwipo meteorological observatory)	Southern A power plant	0.995
	Southern B power plant	1.703
	Southern C power plant	0.500
	Southern D power plant	0.490
Western region of Jeju (Gosan meteorological observatory)	Western A power plant	0.998
	Western B power plant	0.998
	Western C power plant	0.450
	Western D power plant	0.546
	Western E power plant	0.518
	Western F power plant	0.599
	Western G power plant	0.556
	Western H power plant	0.500
	Western I power plant	0.900

The Daily Maximum Power of the JEJU Region

In the summer of 2014 and 2015 the electricity demand wasn't high because the cool weather continued. On the other hand, in the summer of 2016, over 30 degrees of hot weather lasted more than 20 days. And it has renewed the maximum power demand three times and that made the maximum power demand higher.

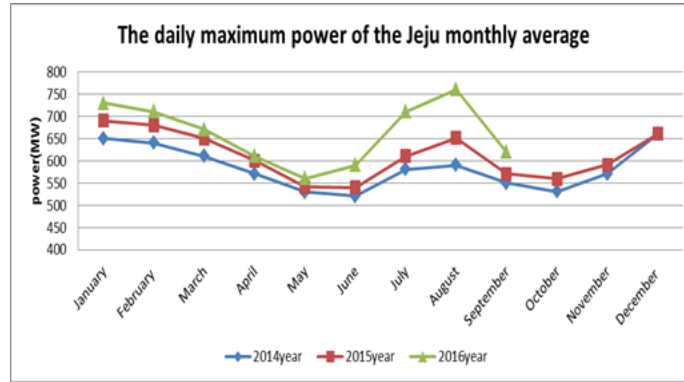


Figure 1: The daily maximum power of the Jeju(monthly average)

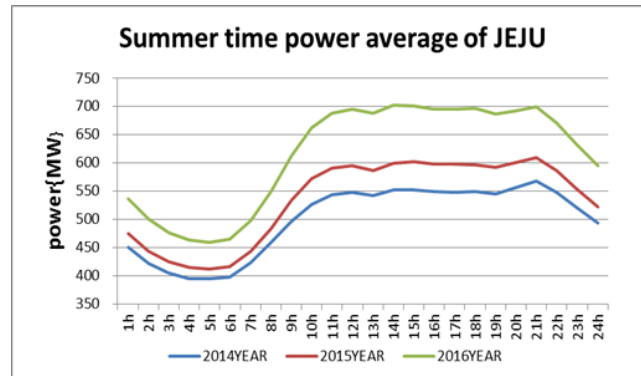


Figure 2: Average power demand during summer in Jeju

Table 2:

Classification of Maximum Load Time in Jeju Area in Summer Power Peak in 2016

Time	Demand (MW)	Note		
14hour	703	Maximum load 10%	Maximum load 20%	Maximum load 30%
15hour	701			
21hour	700			
12hour	696			
17hour	696			
18hour	696			
16hour	695			
20hour	692			
19hour	687			

Jeju Power Peak Time Analysis for 2 Years

As a result of analyzing the power peak of July and August in summer from 2014 to 2016, we can see that demand for summer power peak increases within the years.

For this reason, as the global warming progresses, the average temperature of our country rises as the year passes. So electricity usage continues to increase. The summer peak time remains to electricity usage constant until the evening.

We analyzed power demand in Jeju by time zone that the peak power was the highest in 2016. Looking at Fig.1, In Korea, power peak occurs in summer or winter. So, we investigated the average of each time zone to decide the top 10%, 20%, and 30% load times. And 14:00, 15:00, and 21:00 are included in the top 10% time zone, and 12:00,

17:00, 18:00 are included in the top 20% time zone, and finally 16:00, 20:00, 19:00 are included in the top 30% time zone.

Average Power Generation of Solar Power Plants in the Northern Part of Jeju during the Summer Period of two Years

We obtained the data of Fig. 3 by comparing and analyzing the power generation data of the five power plants in the northern part of Jeju in 2015 and 2016 in July and August.

Table 3 shows the contribution of the solar power plant in the northern part of Jeju to top 10%, 20%, and 30% of peak power in the Jeju region from 2015 to 2016 in July and August.

Summer power peak contribution on the table 3 is saying the value which is contribution of generated electric power for self-generation capacity of solar power plants. In 2015, they contributed 27% for the top 10%, and 26% for the top 20% and 12% for the top 30%. In 2016, they contributed 28% for the top 10%, and 27% for the top 20% and 12% for the top 30%.

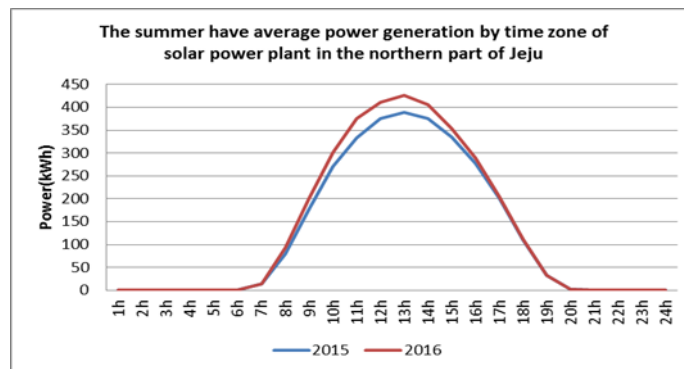


Figure 3: Average power generation by time zone of solar power plant in the northern part of Jeju during summer

Table 3:

POWER PEAK CONTRIBUTION OF SOLAR POWER PLANT IN THE NORTHERN PART OF JEJU Maximum load division	Summer power peak contribution (%)		
	2015 year	2016 year	average
10%	27	28	28
20%	26	27	27
30%	12	12	12

Average Power Generation of Solar Power Plants in the Eastern part of Jeju During the Summer Period of Two Years

We obtained the data of Fig. 4 by comparing and analyzing the power generation data of the six power plants in the eastern part of Jeju in 2015 and 2016 in July and August.

Table 4 shows the contribution of the solar power plant in the eastern part of Jeju to top 10%, 20%, and 30% of peak power in the Jeju region from 2015 to 2016 in July and August.

Summer power peak contribution on the table 4 is saying the value which is contribution of generated electric power for self-generation capacity of solar power plants. In 2015, they contributed 27% for the top 10%, and 27% for the top 20% and 12% for the top 30%. In 2016, they contributed 28% for the top 10%, and 28% for the top 20% and 12% for the top 30%.

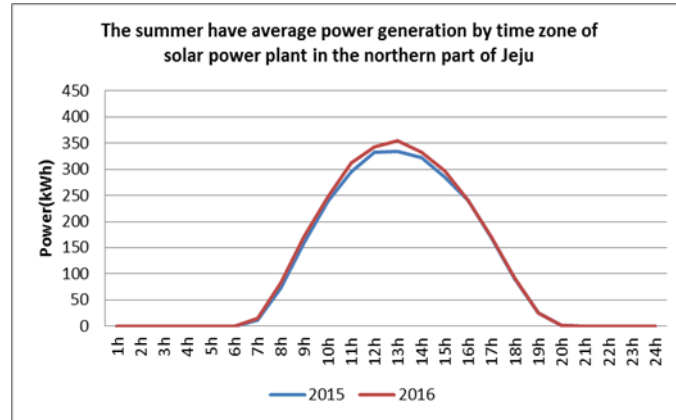


Figure 4: Average power generation by time zone of solar power plant in the eastern part of Jeju during summer

Table 4:

Power Peak Contribution of Solar Power Plant in the Northern Part of Jeju

Maximum load division	Summer power peak contribution(%)		
	2015year	2016year	average
10%	27	28	28
20%	27	28	28
30%	12	12	12

Average Power Generation of Solar Power Plants in the Southern Region of Jeju during The Summer Period of Two Year

We obtained the data of Fig. 5 by comparing and analyzing the power generation data of the four power plants in the southern part of Jeju in 2015 and 2016 in July and August.

Table 5 shows the contribution of the solar power plant in the southern part of Jeju to top 10%, 20%, and 30% of peak power in the Jeju region from 2015 to 2016 in July and August.

Summer power peak contribution on the table 5 is saying the value which is contribution of generated electric power for self-generation capacity of solar power plants..

In 2015, they contributed 27% for the top 10%, and 27% for the top 20% and 12% for the top 30%. In 2016, they contributed 28% for the top 10%, and 27% for the top 20% and 12% for the top 30%.

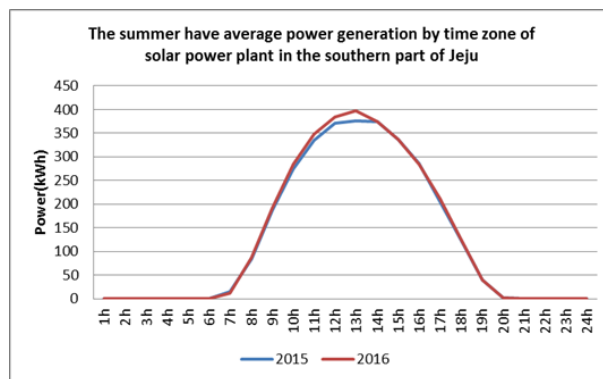


Figure 5: Average power generation by time zone of solar power plant in the southern part of Jeju during summer

Table 5:

Power Peak Contribution of Solar Power Plant in the Southern Part of Jeju

Maximum load division	Summer power peak contribution(%)		
	2015year	2016year	average
10%	27	28	28
20%	27	27	27
30%	12	12	12

Average Power Generation of Solar Power Plants in Thewestern Part of Jeju During the Summer Period of Two Years

We obtained the data of Fig. 6 by comparing and analyzing the power generation data of the eight power plants in the western part of Jeju in 2015 and 2016 in July and August.

Table 6 shows the contribution of the solar power plant in the western part of Jeju to top 10%, 20%, and 30% of peak power in the Jeju region from 2015 to 2016 in July and August.

Summer power peak contribution on the table 6 is saying the value which is contribution of generated electric power for self-generation capacity of solar power plants.

In 2015, they contributed 33% for the top 10%, and 33% for the top 20% and 15% for the top 30%. In 2016, they contributed 33% for the top 10%, and 34% for the top 20% and 15% for the top 30%.

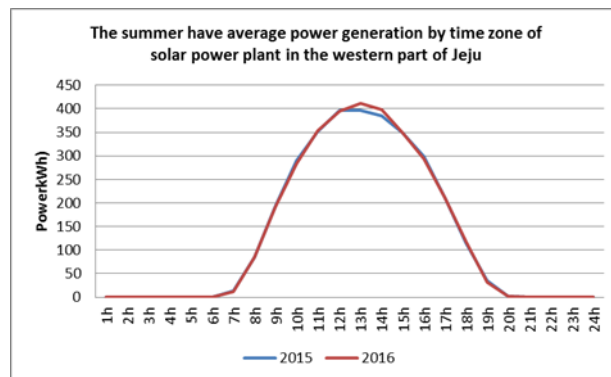


Figure 6: Average power generation by time zone of solar power plant in the western part of Jeju during summer

Table 6:

Power Peak Contribution of Solar Power Plant in the Western Part of Jeju

Maximum load division	Summer power peak contribution(%)		
	2015year	2016year	average
10%	33	33	33
20%	33	34	34
30%	15	15	15

Conclusion

We categorized 24 solar power plants based on the meteorological stations where weather information of 4Jeju areas can be obtained. Moreover, we also studied how much of the electric energy there is contributing to the summer power peak time.

The electric power peak was analyzed in 2015 and 2016 in July and August. As a result, the power peak was the highest in 2016, and the power peak was found to increase as the year progressed. Electric power demand was the wide highest range in summer time from 11:00 to 21:00 in Jeju, and solar power plants produced the bell shape pattern of electric power centered at 13:00.

In Jeju, solar power plants have a high contribution because electricity demand is higher in summer. And in the past two years, the PV plants in the western area of Jeju Island has the highest contribution rate of 33.47%.

Acknowledgement

This research was financially supported by The Project Management Center Cultivating Smart Grid & Clean Energy Manpowers(CK-I), JNU

References

- [1]. The Meteorological Administration. (n.d.). *Ground observation data*. Retrived from http://www.kma.go.kr/weather/observation/past_cal.jsp
- [2]. Lee, G. M. (2015). Contributiveness of a solar power plant on the electric power at summer peak time. Paper presented at *Smart grid research society academic conference*, South Korea (pp 20-23).
- [3]. Shin, Y. S. (2010). Analysis of solar power and wind power status and utilization rate in korea. Paper presented at *academic conference, Korean Institute of Electrical Engineers*.
- [4]. Lee, G. D. (2010). Analysis of power generation efficiency of photovoltaic system applying solar power contribution. Paper presented at *academic conference, Korean Institute of Electrical Engineers*, South Korea.
- [5]. Lee, G. M. (2014). Analysis of power generation of 1mw solar power plant using roof of building. Paper presented at *Smart grid research society academic conference*, (pp 151).
- [6]. New renewable energy researcher. (2016). *New renewable energy year book*.

ECBA-17**Power Generation Characteristics of MW Photovoltaic Power Plants in the Jeju Island**

Hyeon-seong Yoon¹, Seung-beom Kim², Su-wan Kim³, Ankhzaya Baatarbileg⁴, Hoon Kwon⁵, Gae-myung Lee^{6*}

^{1,2,3,4,5,6} Jeju National University, 102 Jejudaehak-ro, Jeju-si, South Korea

Abstract

After introducing the RPS(Renewable Energy Portfolio Standard) system into the Korean electric energy market in the 2012 year in order to promote usage of renewable energy, many MW-scale PV(photovoltaic) plants were actively built nationwide in the South Korea. Also, the recent cost-down for constructing PV plant contributed greatly to increase of PV plants. The government of the Jeju Island has the plan making the island the carbon-free one by the 2030 year. And she is trying to penetrate electric power plants using renewable energy sources such as wind and solar energies in the island. Because many MW-scale PV plants will be constructed in the future in the Jeju Island, we need references on generation characteristics of the MW-scale PV plants on operating in the island. In this research, the Jeju Island is divided into 4 regions according to weather similarity. The generation characteristics of MW PV plants were investigated and analyzed. And the relationship of the sunshine duration and the generated electric energy of the PV plant is almost linear and the sunshine durations in the 4 regions for the past 20 years were investigated. The relation between the sunshine duration and the utilization rates of the PV plants was analyzed.

© 2017 The Authors. Published by Academic Fora. This is an open access article under the CC BY-NC-ND license

(<http://creativecommons.org/licenses/by-nc-nd/4.0/>)

Peer-review under responsibility of the Scientific & Review committee of ECBA- 2017.

Keywords— Photovoltaic Power Plants, Renewable Energy, Generation Characteristics, Sunshine Duration

Introduction

More than 95% of the energy we are currently using is fossil fuels such as petroleum, coal and natural gas. When fossil fuel is burned, it releases the heat simultaneously with carbon dioxide and water vapor, causing global warming. As a result, the whole world is developing inexpensive and environmentally-friendly alternative energies to prevent global warming.

Now, the world has cooperated to deal with global warming. As a follow-up to the treaty, the penetration rate of renewable energy to each country was allocated. In accordance with this, the Korean government also will reduce fossil fuel dependency to 33% by executing the plan “Energy Vision 2030”. The Korean government announced to raise the penetration rate of renewable energy to 11%,”Law for promoting of Development, Utilization and penetration of New and Renewable Energy was established to raise the penetration rate of renewable energy and to revitalize the related industry, and government subsidized projects are being implemented.

After, the Renewable Portfolio Standard (RPS) system was enforced from January 1, 2012 in South Korea, large-scale PV plants were built nationwide and also in Jeju Island many photovoltaic power plants were built.

In this paper, Jeju Island is divided into four regions, east, west, south and north, and the power generation characteristics of the large scale PV plant distributed in the regions are compared and analyzed. The average utilization rates of the PV plants in each of the four regions were determined and compared with each other. Influences of the sunshine hours and the average temperature on the utilization rate of PV plants were examined.

*All correspondence related to this article should be directed to Gae-myung Lee, Jeju National University, 102 Jejudaehak-ro, Jeju-si, South Korea

Email: myounglk@jejunu.ac.kr

© 2017 The Authors. Published by Academic Fora. This is an open access article under the CC BY-NC-ND license

(<http://creativecommons.org/licenses/by-nc-nd/4.0/>)

Peer-review under responsibility of the Scientific & Review committee of ECBA-2017.

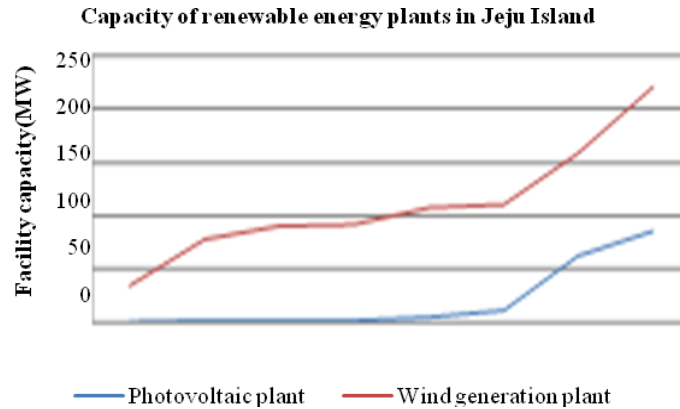


Figure 1. Current status of PV and wind electric generation facilities constructed in Jeju Island

Current Status of Renewable Electric Power Plants in Jeju Island

Fig. 1. shows capacity of renewable energy plants in Jeju Island, until 2015, the capacity of PV plant is about 72.7MW and the capacity of wind generation plant is about 215.6MW.

We can see from Fig. 1. that after the introduction of the RPS system into the Korean electric energy market in 2012, many PV plants and wind generation plants were constructed in Jeju Island.

Table 1:

Classification of the PV Plants In Jeju Island

Region classification	Photovoltaic plants	Capacity(MW)
Northern region of Jeju	Northern A power plant	1.098
	Northern B power plant	1.208
	Northern C power plant	0.460
	Northern D power plant	0.990
	Northern E power plant	0.506
Eastern region of Jeju	Eastern A power plant	0.988
	Eastern B power plant	0.998
	Eastern C power plant	0.950
	Eastern D power plant	0.647
	Eastern E power plant	0.490
	Eastern F power plant	0.500
Southern region of Jeju	Southern A power plant	0.995
	Southern B power plant	1.703
	Southern C power plant	0.500
	Southern D power plant	0.490
Western region of Jeju	Western A power plant	0.998
	Western B power plant	0.998
	Western C power plant	0.450
	Western D power plant	0.546
	Western E power plant	0.518
	Western F power plant	0.599
	Western G power plant	0.556
	Western H power plant	0.500
	Western I power plant	0.900

Classification of the PV Plant Constructed in Jeju Island

Among the PV plants built in the Jeju Island, Table 1 shows the PV plants that have been operating for more than two years.

The Jeju Island meteorological office provides weather forecast for 4 regions in Jeju Island. They are divided according to climate similarity. In this study we also classified Jeju Island into 4 regions: Eastern region, Western region, Southern region and Northern region.

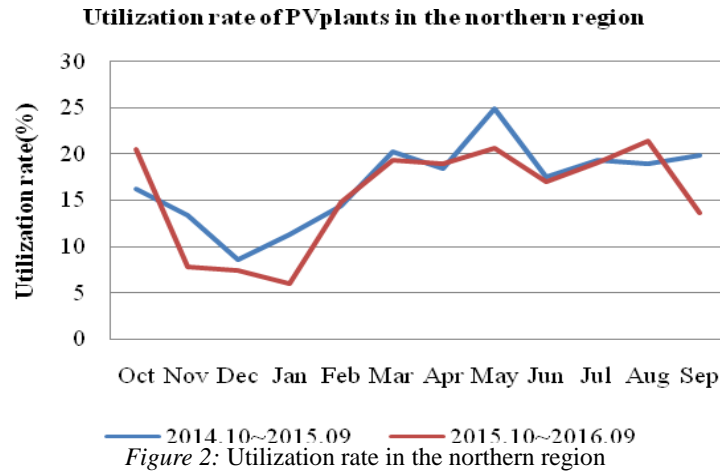


Figure 2: Utilization rate in the northern region

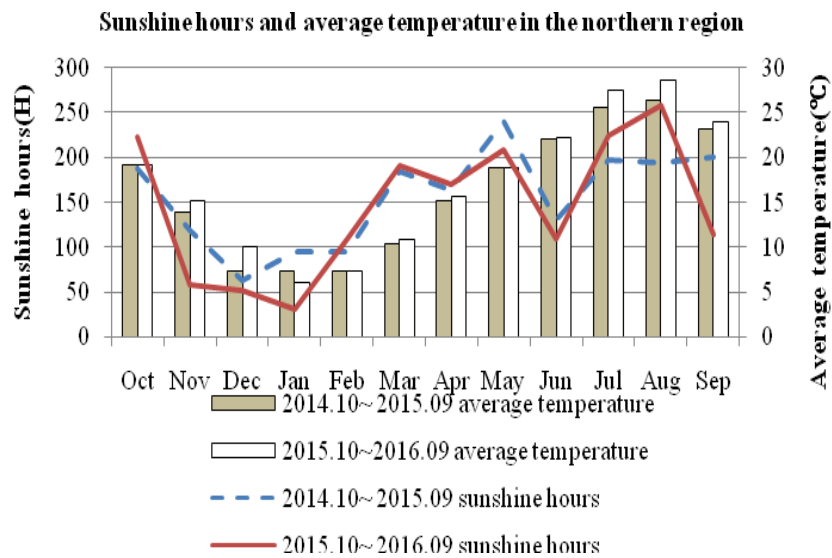


Figure 3: Sunshine hours and average temperature in the northern region

Utilization Rate of PV Plants in the Northern Region

The utilization rate of the northern region of Jeju Island is the monthly average value of five PV plants for 2 years from October 2014 to September 2016.

From analyzing Fig. 2 and Fig. 3, it can be seen that the utilization rate is high in May and August when the sunshine hours is long and the utilization rate is low when the sunshine hours is short in December, January, and February. In June, when it was rainy season, utilization rate is low because the sunshine hours is short.

In the case of the northern region of Jeju, the highest utilization rate of about 25% was shown in May 2015.

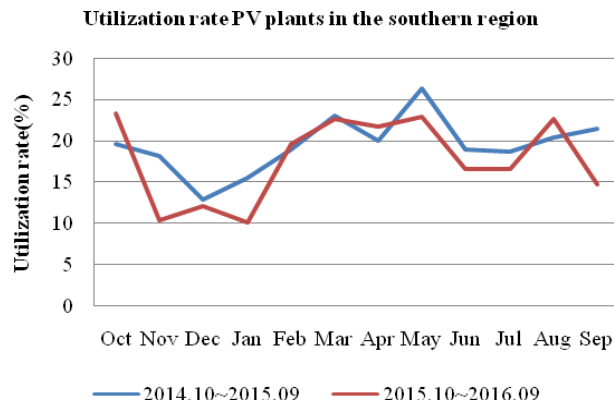


Figure 4: Utilization rate in the southern region

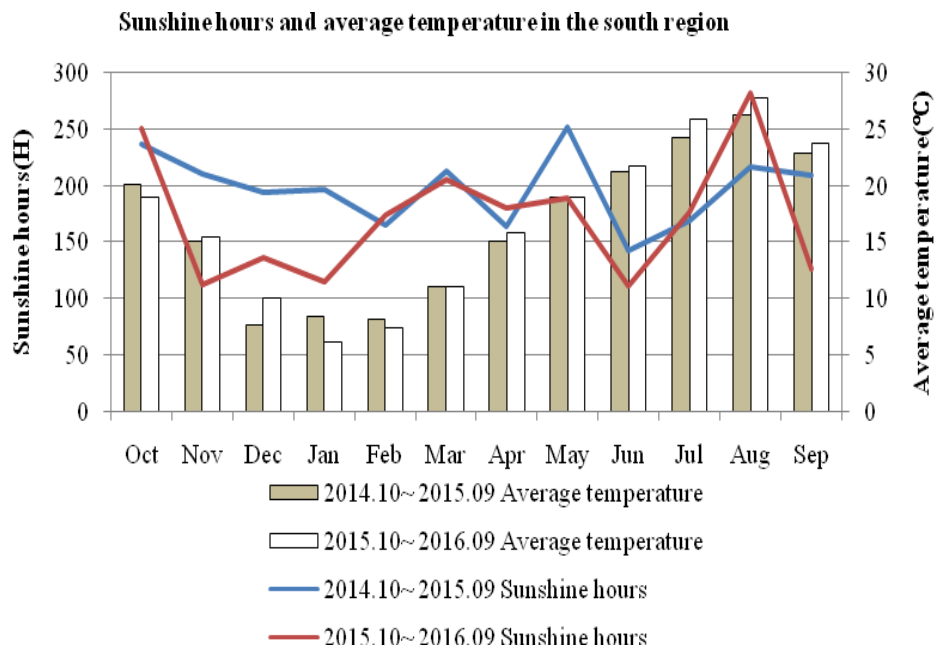


Figure 5. Sunshine hours and average temperature in the southern region

Utilization Rate of The PV Plants in The Southern Region

The utilization rate in the southern region of Jeju Island is the monthly average value of four PV plants for 2 years from October 2014 to September 2016.

From analyzing Fig. 4 and Fig. 5, it can be seen that the utilization rate is high in May when the sunshine hours is long and the utilization rate is low when the sunshine hours is short in November and January. In June, when it was rainy season, utilization rate is low because the sunshine hours is short

In the case of the southern region of Jeju, the highest utilization rate of about 26% was shown in May 15, 2015.

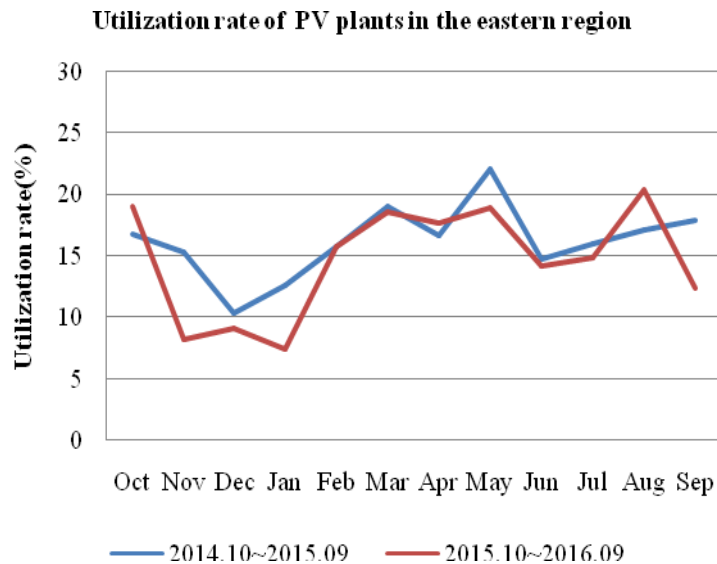


Figure 6: Utilization rate in the eastern region

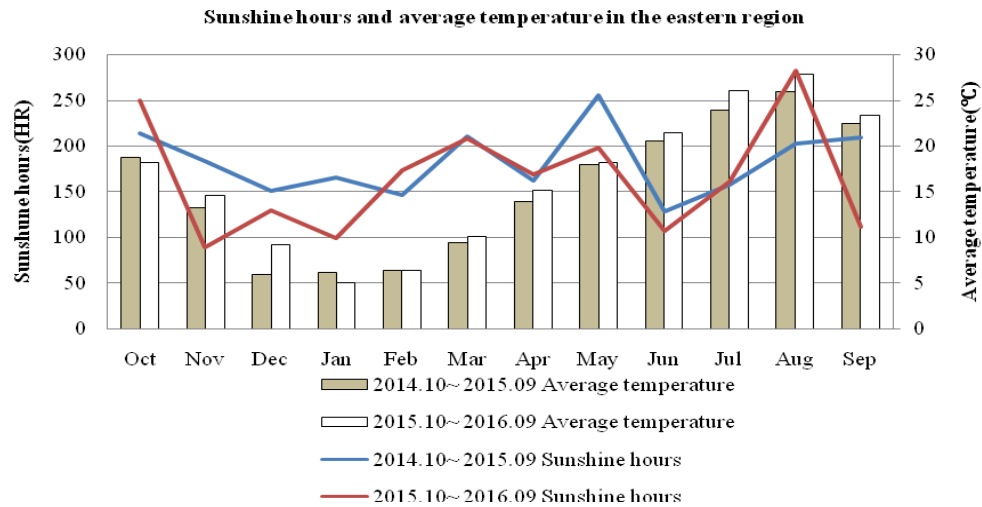


Figure 7: Sunshine hours and average temperature in the eastern region

Utilization Rate of The PV Plants in The Eastern Region

The utilization rate in the eastern region of Jeju Island is the monthly average value of six PV plants for 2 years from October 2014 to September 2016.

From analyzing Fig. 6 and Fig. 7 it can be seen that the utilization rate is high in May and August when the sunshine hours is long and the solar photovoltaic utilization rate is low when the sunshine hours is short in November and January. In June, when it was rainy season, utilization rate is low because the sunshine hours is short.

In the case of the eastern region Jeju, the highest utilization rate of about 22% was shown in May 2015.

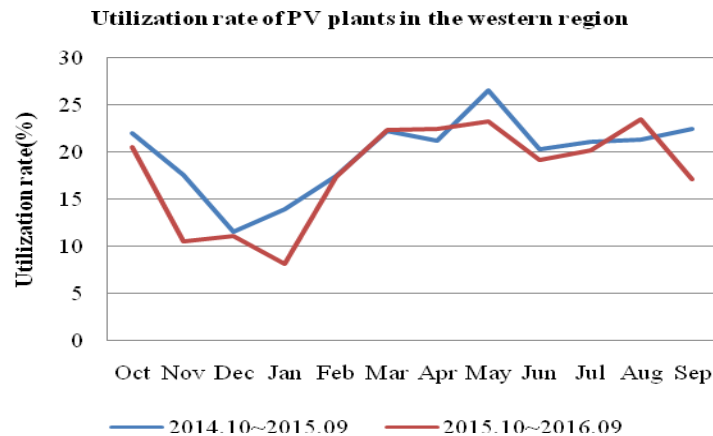


Figure 8: Utilization rate in the western region

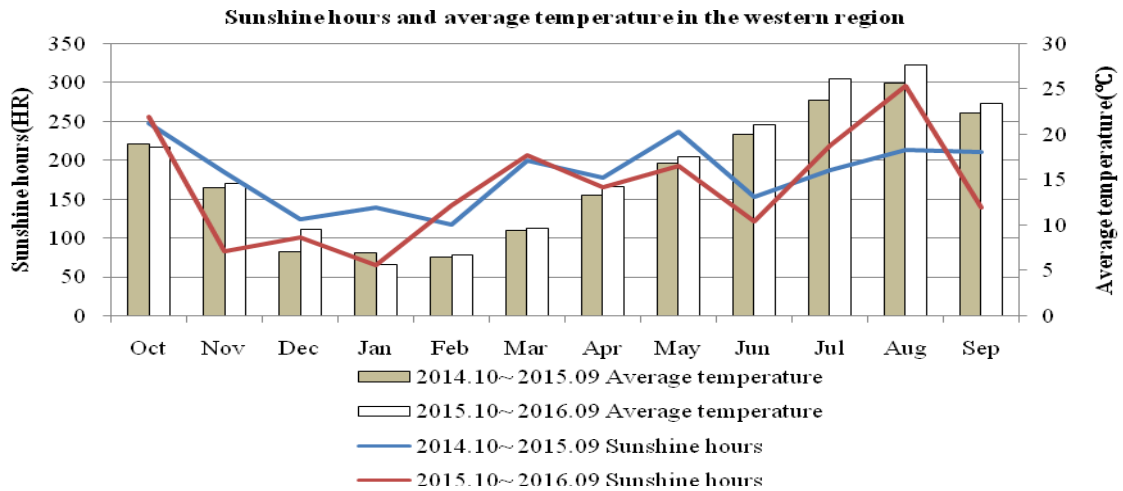


Figure 9: Sunshine hours and average temperature in the western region

Utilization Rate of PV Plants in the Western Region

The utilization rate in the western region of Jeju Island is the monthly average value of nine PV plants for 2 years from October 2014 to September 2016.

From analyzing Fig. 8 and Fig. 9, it can be seen that the utilization rate is high in May and August when the sunshine hours is long and the utilization rate is low when the sunshine hours is short in November and January. In June, when it was rainy season, utilization rate is low because the sunshine hours is short.

In the case of the western region Jeju, the highest utilization rate of about 26% was shown in May 2015.

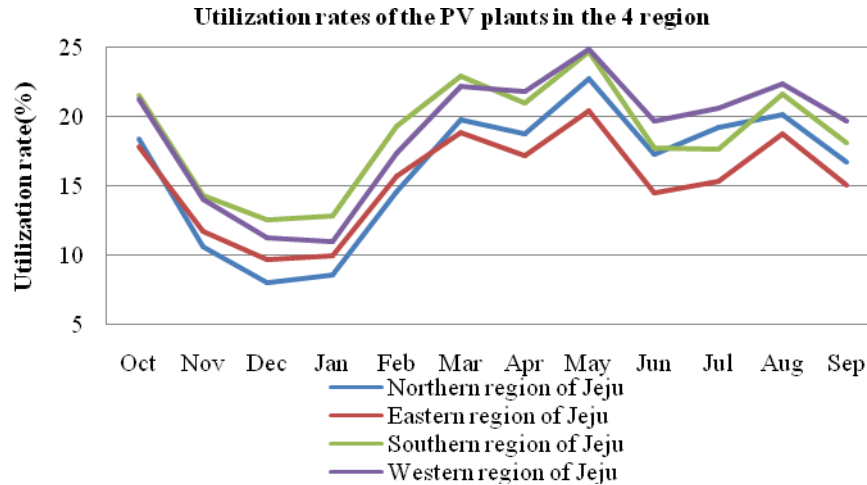


Figure 10: Comparison of average utilization rates of the PV plants in the 4 regions

Comparison of Average Utilization Rates of The PV Plants of The 4 Regions

Fig. 10 shows the comparison of the average utilization rates of the PV plants in the 4 regions from October 2014 to September 2016.

In all regions the highest utilization rate is shown in May, is monthly and its value is about 25% in the southern and western regions, about 23% in the northern region and about 20% in the eastern region. Because of the effect of rainy season in June, sunshine hours is short. So, all regions show the same phenomenon that the utilization rates get lower in June.

Conclusion

This study showed that the utilization rates was high in southern and western regions, and low in the eastern and northern region.

Before this study, we estimated that the highest utilization rate will be obtained at the PV plants in the southern region in Jeju Island, because the southern region is warm and has long sunshine hours. But from this study we can see that the highest utilization rate, 21% of average annual value was obtained at the PV plants in the western regions of Jeju Island.

We, in this study, obtained the value of utilization rate ofPV plants in the specified region using data only for two years. Climate changes every year and sunshine hours change every year,so we need long time data to obtain more correct value of utilization rate ofPV plantswhich can be used as reference value.

Acknowledgement

This research was financially supported by The Project Management Center Cultivating Smart Grid & Clean Energy Manpowers(CK-I), JNU

References

- [1]. Korea Power Exchange. (n.d). *Jeju, EMS Public data*.
- [2]. Korea Meteorological Administration. (n.d). *Ground observation data*. Retrieved from http://www.kma.go.kr/weather/observation/past_cal.jsp
- [3]. Lee,G.M.(2015). Comparison of power generation characteristics of domestic MW photovoltaic power plants. Paper presented at *Smart Grid Group association Autumn Symposium Conference*. (pp 69-72).
- [4]. Shin,Y.S. (2010). Analysis of the current status and utilization rate of Korea solar energy and wind power generation. Paper presented at *Autumn Conference of Electric Power Technology Ministry Society, The Korean Institute of Electrical Engineers*.

ECBA-17**An Experimental Study on the Mechanical Properties of Lightweight Aggregate Concrete Using Ultra High Performance Concrete and Expanded Polystyrene Beads**Yujin Ha¹, Sung-gul Hong^{2*}^{1,2}Seoul National University, South Korea**Abstract**

The mechanical properties of lightweight aggregate concrete using ultra-high performance concrete (UHPC) and expanded polystyrene beads (EPS) has been studied. The objective of experimental program is to measure the compressive strength of lightweight aggregate concrete using ultra high performance concrete and expanded polystyrene beads. The mix rate of EPS has an effect on the unit weight, slump flow and strength enhancement. Unit weight and slump flow decrease when the replacement rate of EPS increases. Compressive strength also decreases if the specimen contains more EPS. The study demonstrated the possibility of various type of lightweight aggregate concrete for different purpose. Thus, practical use and application of EPS beads can be improved and new type of lightweight aggregate concrete is possible to use.

© 2017 The Authors. Published by Academic Fora. This is an open access article under the CC BY-NC-ND license (<http://creativecommons.org/licenses/by-nc-nd/4.0/>)

Peer-review under responsibility of the Scientific & Review committee of ECBA- 2017.

Keywords— Lightweight Aggregate Concrete, UHPC, EPS

Introduction

The demand for lightweight concrete in various applications of construction has been increased and still growing up, because of the advantage that lower density results in a significant benefit in terms of load-bearing element of smaller cross sections and a corresponding reduction in the size of the foundation.

Heat-insulation is another important component in house construction and the demand for buildings is increasing and it will grow more in the next years. There are several regulations covering different general guidelines that must be considered in order to decrease the energy demand in buildings. One of the main ones consists in increasing the insulation of the building envelope with the aim of minimizing heat losses. As a result, a proper treatment of heat loss becomes more relevant because their relative effect on the overall thermal demand of the building increases.

Expanded polystyrene (EPS) beads are artificial lightweight aggregate and It can be used for many applications e.g. trays, plates, bowls and fish boxes. Other uses include molded sheets for building insulation and packing material for cushioning fragile items inside boxes. According to its technical properties such as low weight, rigidity, and formability, EPS beads can be used to produce low-density concrete required for building applications like cladding panel, curtain walls, composite flooring systems, and load-bearing concrete blocks.

Expanded polystyrene concrete has economic and superior insulation properties. It is not as strong as stone-based concrete mixes, but has other advantages such as increased thermal and sound insulation properties, easy shaping and ability to be formed by hand with sculpturing and construction tools. But the low strength makes limit for use the material widely. So, if the strength of EPS can be complemented, the new material for structure can be invented. On the other hand, Ultra-high performance concrete has superior mechanical properties. Owing to its dense microstructure, UHPC has both a high strength and also a greater stiffness when compared with normal- and high-strength concretes. EPS beads can be used as light weight aggregate according to the combination method with UHPC. By incorporating the EPS beads at different volume percentages in UHPC, a wide range of concrete densities and properties can be achieved.

Earlier researchers studied EPS mostly in mortar with Ordinary Portland Cement as the binder. Other investigators also reported that EPS tends to float and can result in a poor mix distribution and segregation, necessitating the use of admixtures or special treatment for the beads.

The present study is an effort to develop structural lightweight concretes with the corresponding strengths. UHPC mixed with EPS beads were investigated. The investigations included parameters related to strength like compressive

*All correspondence related to this article should be directed to In Sung-gul Hong, Seoul National University, South Korea

Email: sghong@snu.ac.kr

© 2017 The Authors. Published by Academic Fora. This is an open access article under the CC BY-NC-ND license

(<http://creativecommons.org/licenses/by-nc-nd/4.0/>)

Peer-review under responsibility of the Scientific & Review committee of ECBA-2017.

and flexural strengths. This study offers the basic material for the utilization of EPS lightweight aggregate concrete by suggesting and evaluation the principal performance required by the structure and lightweight aggregate concrete.



Figure 1. Mixing and curing process

Methodology

The Insulation used in this study is EPS with bead method for building thermal insulation according to KS M 3808. EPS beads used in this study were selected according to result of experiment. To choose one type of EPS beads, compressive strengths of EPS concrete using EPS type A, B and C were compared. Specimens with type B show the highest and constant compressive strength.



Figure 1. Three type of EPS beads

The UHPC used in this study was a variation of the basic mix of UHPC with a water/binder ratio of 0.23 and it has flowability of concrete exceed more than 250mm diameter with measurement tools presented in KS L 5111. That mix is used in several research projects at the Seoul National University.

Experimental Investigations

The dimension of compressive strength experiment specimens was 50mm*50mm*50mm. Cubes were kept in a hot air oven at 60°C for 72hours. This is because at this temperature range of 100-110 °C, the EPS beads initially shrink and finally evaporate. These are then immersed in water and the weight gain is measured at regular intervals until a constant weight is reached.

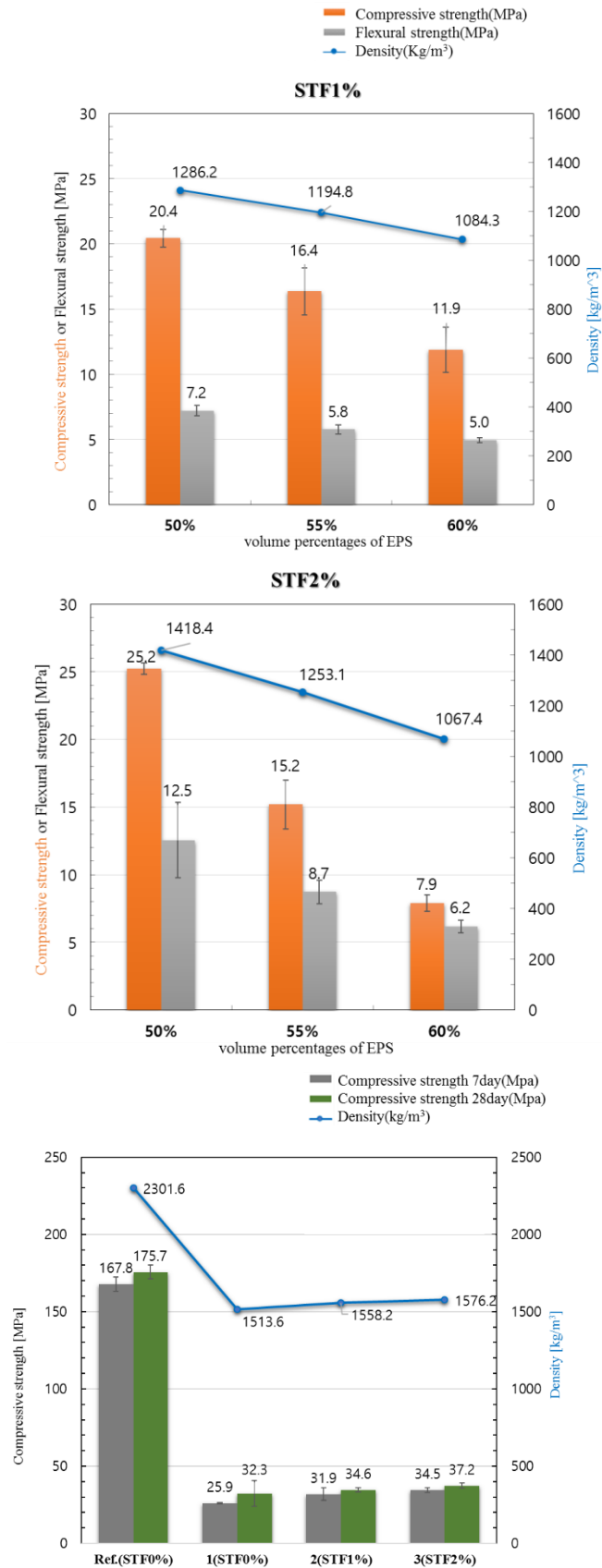
Compressive strength test was carried out in a testing machine of 2ton capacity at a loading rate of 2.5kN/s.

Results & Discussion

The failure observed was to be more gradual and the specimens were capable of retaining the load after failure without full disintegration.

Compressive Strength

The density of concrete was controlled by varying the EPS volume in the mix. The variation of compressive strength with the percent volume of EPS was ranged between 50% and 60%. The compressive and flexural strength of EPS concretes appears to increase linearly with an increase in concrete density, with a decrease in the EPS volume and with an increase in volume of steel fiber.



When the volume of EPS in mix was fixed with 50%, the compressive strength of EPS concretes appears to increase linearly with an increase in volume of steel fiber.

Table1.
Application of Lightweight Concrete According to Compressive Strength

Compressive Strength (MPa)	Application
0.69~6.86	Insulation
6.86~17.15	Filling concrete
17.15 above	Structural purpose

Regardless of the volume percentage of EPS or steelfiber, all EPS concrete using UHPC specimens experimented appear that can be used as filling concrete as the compressive strengths exceed 6.86MPa. And the EPS concrete with EPS that less volume percentage of 50 can be used for structural element because the compressive strengths observed exceed 17.15MPa.

Conclusion

- All the EPS concrete without any special bonding agents show good workability and could be easily compacted and finished. Due to the flow value of UHPC is high, fluidity of EPS concrete using UHPC was good.
- The rate of strength development of the concretes increased with decreasing percentage of EPS. The strength of EPS concrete using UHPC was found to be directly proportional to the concrete density.
- Controlling the percentage of EPS, various type of EPS concrete using UHPC could be produced for each demand. Combination method is understandable and easy to use.

Acknowledgement

This research was supported by a grant (13SCIPA02) from Smart Civil Infrastructure Research Program funded by Ministry of Land, Infrastructure and Transport (MOLIT) of Korea government and Korea Agency for Infrastructure Technology Advancement (KAITA).

References

- [1]. Babu, K. G., & Babu, D. S. (2003). Behaviour of lightweight expanded polystyrene concrete containing silica fume. *Cement and Concrete Research*, 33(5), 755-762.
- [2]. Short, A., & Kinniburgh, W. (1978). *Lightweight Concrete* (3rd ed). London, UK: Applied Science Publishers,
- [3]. Sussman, V. (1975). Lightweight plastic aggregate concrete. *ACI J*, 72, 321-323.

ECBA-17

Punching Shear Strengthening of RC Interior Flat Plate-Column Connections with UHPFRC Overlay on Concentric LoadingHyunsoo Youn¹, Sunggul Hong^{2*}^{1,2}*Department of Architecture and Architectural Engineering, Seoul National University, South Korea*

Abstract

The flat plate system is subjected to the combination of locally high negative bending moments and shear forces around the columns, which increases the susceptibility of this zone to brittle punching shear failure. As can be seen in many collapse accidents, it may eventually lead to a hazardous progressive collapse of the entire structure, accompanied by a truncated cone above the column. Therefore due to the brittle failure as well as the increasing number of aging structures, the necessity for strengthening of existing concrete flat plate against punching shear is significantly emphasized. One of effective methods to strengthen the punching shear strength is to place a thin overlay of Reinforced UHPFRC over the existing RC flat plate-column connections. Ultra-High Performance Fiber-Reinforced Concrete (UHPFRC), developed in the mid-1990s, is a new material which has attracted many researches and engineers for practical construction applications in structures, owing to its splendid mechanical performances. Additionally, it was demonstrated by previous researches that this method increases rigidity, and bending and shear strength of one-way RC members. In this experimental program, shear strength, behavior and crack pattern of RC two-way flat plate-column connections strengthened with a thin layer of UHPFRC with or without steel rebar would be investigated. The critical design variables are UHPFRC overlay thickness, and the amount of steel rebar placed in the UHPFRC overlay.

© 2017 The Authors. Published by Academic Fora. This is an open access article under the CC BY-NC-ND license (<http://creativecommons.org/licenses/by-nc-nd/4.0/>)

Peer-review under responsibility of the Scientific & Review committee of ECBA- 2017.

Keywords— UHPFRC, Flat Plate-Column Connection, Punching Shear Strength UHPFRC Overlay

Introduction

In the 1950s, reinforced concrete (RC) flat plate systems started to become prevalent because of its simplicity, functional benefits than other structural systems. In addition to parking garages, medium height residential and office buildings have been constructed in the form of flat plate systems⁷⁾. However, the flat plate systems are subjected to the combination of locally high negative bending moments and shear forces around the columns, which increases the susceptibility of this zone to brittle punching shear failure. As can be seen in many collapse accidents, it may eventually lead to a hazardous progressive collapse of the entire structures, accompanied by a truncated cone above the column. Additionally, many existing buildings constructed with flat plate systems are becoming obsolete. In this trend, it is significantly emphasized to investigate reinforcing the RC flat plate systems against punching shear failure.

To strengthen a RC flat plate with deficient resistance, it has been proposed to add on the surface a thin layer, 25-75mm in thickness, of Ultra-High Performance Fiber-Reinforced Concrete (UHPFRC) with small diameter steel rebars¹⁷⁾. This technique modifies the RC flat plate into an UHPFRC-RC composite flat plate. The UHPFRC layer with the small diameter steel rebars acts as a tensile reinforcement and increases both bending and shear resistances of the system^{10,11)}.

The main purpose of this experimental study is to investigate the effects of UHPFRC overlay with or without steel rebars. Focus is thus placed on the behavior of RC flat plates without transverse reinforcement submitted to concentrated loadings at center with a layer of UHPFRC acting as a two-dimensional tensile reinforcement.

Literature Review

Punching Resistance of RC Flat Plate Without Transverse Reinforcement

In order to predict the behavior of the UHPFRC-RC composite flat plate on punching shear, mechanisms which dominate the punching shear behavior of RC flat plate system should be thoroughly understood. According to several design codes^{3,4,5,6)}, influential variables about the punching shear resistance of a RC flat plate without transverse reinforcement are the ratio of tensile flexural reinforcement, flat plate and supporting column dimensions, and

*All correspondence related to this article should be directed to Sunggul Hong, Department of Architecture and Architectural Engineering, Seoul National University, South Korea
Email: berksmile@naver.com

© 2017 The Authors. Published by Academic Fora. This is an open access article under the CC BY-NC-ND license (<http://creativecommons.org/licenses/by-nc-nd/4.0/>)

Peer-review under responsibility of the Scientific & Review committee of ECBA-2017.

concrete compressive and tensile strengths. According to several previous studies, punching shear failure is typically governed when the ratio of tensile flexural reinforcement is greater than 0.75%7).

Strengthening Methods

To date, various methods have been proposed and used for strengthening existing flat plate systems against punching shear failure: enlargement of the column support area, post installed shear reinforcement, pre-stressing or increasing the amount of flexural reinforcement. This last method has been widely investigated to increase the punching shear resistance of flat plate system by attaching CFRP, GFRP, etc. to the tensile surface. However, these methods have a long construction process and a lot of labor. In addition, these methods are not capable of reducing permeability that causes cracks and corrosion of steel rebars placed in RC structures.

Alternatively, casting a thin layer of UHPFRC on the RC flat plate system can be employed9,10,11,12,17). It is possible to cast the UHPFRC overlay directly on the prepared existing concrete surface without any mechanical shear connectors or bonding materials, such as epoxy resin used to attach steel plates or FRP sheets. It is well known that when the substrate concrete surface is sandblasted, the interface between RC substrate and UHPFRC exhibits excellent adhesion performance. According to the existing researches, the bond strength at the interface between the sandblasted concrete surface and the UHPFRC overlay is generally much greater than the design strength proposed in current codes of practice15,19).

Methodology

Experiment Variables

In order to evaluate the punching shear resistance performance of UHPFRC-RC composite flat plate-column connections with UHPFRC overlay on the tension side of existing RC substrate, the punching shear test of two-way slabs was performed by setting the UHPFRC overlay thickness and steel rebar ratio in UHPFRC overlay as variables. The UHPFRC overlay thickness was set to 0, 30 and 50mm, which is recommended rehabilitating thickness by Hable et al.17) In addition, a small amount of steel rebars placed in UHPFRC overlay inhibits micro-cracks of the UHPFRC from propagating to the macro-cracks and even promotes distribution of the micro-cracks against external load, thereby ultimately increasing bending and shear resistance and improving strain hardening behavior of the system. Therefore, to investigate the effect of additional reinforcement in UHPFRC overlay, 0, D10@180 and D10@90 steel rebars were placed. The main parameters of the test specimens are detailed in Table 1

Table 1:

Main Parameters of Test Specimens

Specimens	Geometry					Steel in RC		Steel in UHPFRC	
	B (mm)	r_s (mm)	C (mm)	h_c (mm)	h_U (mm)	d_{sc} (mm)	Layout (mm)	d_{sU} (mm)	Layout (mm)
C0	2600	1250	420	150	0	114	D16@140	-	-
C30					30			-	-
C50					50			-	-
C50S								175	D10@180
C50L								175	D10@90

Note) B=specimen size, r_s = the distance from center to support, C = column width, h_c =height of RC section, h_U =thickness of UHPFRC overlay, d_{sc} = effective flexural depth from the extreme compression fiber to the centroid of tension steel rebars in RC section, d_{sU} = effective flexural depth from the extreme compression fiber to the centroid of steel rebars in UHPFRC overlay.

3.2 Test specimens

A total of five square UHPFRC-RC composite flat plate-column connection specimens without transverse reinforcement were planned and simply supported by steel plates of size of 200mm x 200mm x 40mm at 8 points equally spaced around circumference with radius of 1250mm from the center, which reflect the line of contraflexure points of radial bending moments. This type of setting is one of the flat plate-column connection test specimen settings adopted in a considerable number of existing studies.7,10,11,16) First of all, RC substrate of all specimens has a column with a square cross section of 420mm by 420mm. The size of the specimens was 2600mm by 2600mm with a total thickness of 150mm. Concrete cover of RC section was kept constant and equal to 20mm for all specimens. All presented specimens had same orthogonal reinforcement and a standard longitudinal reinforcement ratio in the RC section equal to 1.24% for tension side reinforcement and 0.435% for compression side reinforcement using 16mm bars and 10mm bars equally spaced at 140mm, respectively.

For RC members with UHPFRC overlay on the tension side, interface condition between the RC substrate and UHPFRC overlay should be carefully taken into account. In order to retain recommendable interfacial bond strength at the interface between the different types of concrete, the surface treatment method is the most important.



(a) Sand blasting



(b) Smooth(left) and roughened(right) surfaces

Figure 1: Preparation of roughened surface

Among the various surface treatment methods (left smooth, sand blasting, wire brushing, hammer chipping, etc.) proposed in current standard design codes, the sand blasting method which exhibits superior bond strength can reduce the loss of existing members to the utmost and effectively forms a rough surface^{15,19}. It is a mechanical treatment method which makes the surface rough by spraying sufficiently dried sand particles on the surface. In this study, size of 1.2~1.5mm sand particles were sprayed using an engine type compressor with discharge pressure of about 0.88~0.98MPa. The surfaces were cut by 2~3mm as shown in Fig 1. For efficient shear transfer, the sandblasted surfaces were washed with water to prevent latency, and the UHPFRC was casted after removing residual dust by wind pressure. In order to prevent the steel fiber balling, the UHPFRC was sufficiently mixed in a mixer and poured. After the pouring, no additional mechanical treatment such as vibrator was applied to prevent sinking of the steel fiber.

For the specimens with a 50mm thick UHPFRC overlay, three specimens were fabricated by setting the steel reinforcement ratio inside the overlay as a variable. In the case of specimens with steel reinforcement, the UHPFRC cover thickness was planned to be 15mm, which is smaller than that of ordinary RC. However, it is quite logical when considering the UHPFRC's homogeneous and tight material compositions. Detailed specification about the test specimens is schematically shown in Fig 2.

UHPFRC must follow the curing conditions according to the guidelines^{1,2}) to ensure a certain level of mechanical performances. After casting UHPFRC overlay on the specimens, the specimens were cured at $20\pm 2^{\circ}\text{C}$ for 24 hours, and then cured at a high temperature of $90\pm 5^{\circ}\text{C}$ with $95\pm 5\%$ humidity for 48 hours. RC substrates with UHPFRC overlay except for C0 were also cured under the same conditions during the curing period.

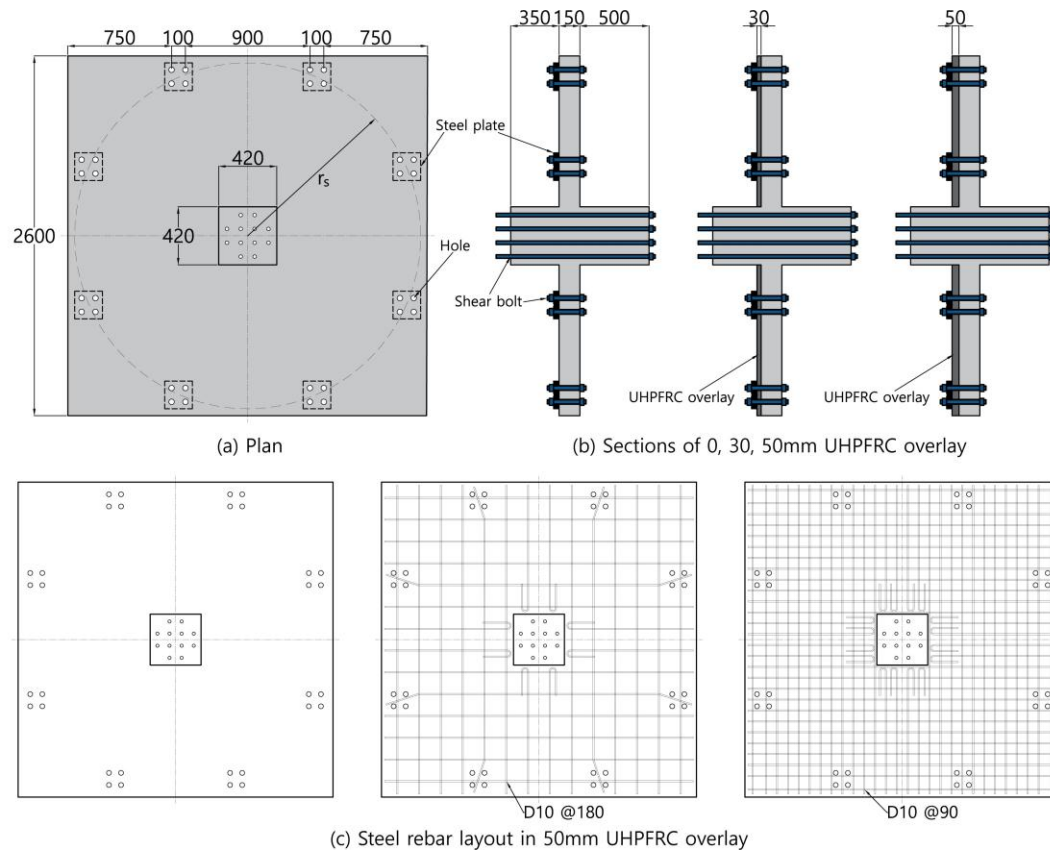


Figure 2: Plan and sections of specimens with 0, 30, 50mm UHPFRC overlay, and steel rebar layout in 50mm UHPFRC overlay

Material Properties

For the fabrication of test specimens, the whole RC substrates were casted using NSC with design strength of 30MPa. Since the amount of concrete used in the test specimens is large, the NSC has been poured twice in total. For the measurement of compressive strength of NSC, 3 of cylinder specimens with a diameter of 100mm and a height of 200mm were prepared in accordance with KS F 2403 and cured under the same conditions as the specimens. The compressive strength tests were carried out in accordance with KS F 2405 for strength measurements after 28 days from concrete casting days. Table 2 shows the mix proportions of the NSC mix design.

Table 2:

Mixture Proportions of NSC

Nominal strength	W/C (%)	Unit weight (kg/m ³)				
		W	C	S	G	SP
30	43.1	169	392	825	952	2.74

Note) Maximum aggregate size=25mm, Slump = 120mm.

UHPFRC is a new construction material that improves compressive strength, tensile strength and flexural toughness compared to existing SFRC (Steel Fiber-Reinforced Concrete) by mixing steel fiber with UHPC¹). Today, various types of steel fiber such as straight, hooked and twisted steel fiber have been developed, but in this study, straight steel fibers with yield strength of 2500MPa, an aspect ratio of 13mm/0.2mm were used in a volume ratio of 2%. To measure the compressive strength of UHPFRC, 3 of cylinder specimens were prepared by the same method as for NSC. For measurement of tensile strength of UHPFRC, 6 of specimens with notches of 2mm width and 12.5mm depth were prepared as explained in detail in K-UHPC APPENDIX 11). All the specimens were cured under the same conditions as the test specimens. Table 3 shows the material compositions of UHPFRC, and Table 4 shows the overall material properties of concretes and steel reinforcements. All the actual strengths are the average of the measured strength values.

Table 3:

Mixture Proportions of UHPFRC

Nominal strength	W/C (%)	Unit weight (kg/m ³)				
		Water	Premix binder	Fine aggregate	Super plasticizer	Air-entraining agent
180	0.2	197.1	1269.5	867.4	18.1	0.5

Note) Premix binder = cement, Zr, Bs, filler, expansion agent, shrinkage reducing agent premix, Slump flow = 740mm.

Table 4:

Material Properties of Concrete and Reinforcement

	Name	NSC	UHPFRC			Reinforcement(f_y)	
		f_{ck}	$f_{ck,U}$	f_{Ute}	f_{Utu}	D16	D10
Nominal strength	-	30	180	10	12	400	400
Actual strength (avg.value)	C0	33.8	-	-	-	433	400
	C30	31	184.9				
	C50	31	184.9				
	C50S	31	184.9				
	C50L	34.9	184.9				

Note) All units in MPa(=N/mm²), f_{ck} = NSC compressive strength, $f_{ck,U}$ = UHPFRC compressive strength, f_{Ute} = maximum tensile elastic strength of UHPFRC, f_{Utu} = tensile strength of UHPFRC, f_y = yield strength of steel reinforcement

Instrumentation and Test Set-Up

A total of 12 shear bolts in size of diameter of 24mm installed at the bottom of the actuator with a capacity of 2000kN and penetrated through the column of the test specimen and fixed to the lower part of the column. To consider the contraflexure points of radial bending moments of real flat plate system structures, the specimens were simply supported by steel plates of size of 200mm x 200mm x 40mm at 8 points located at 1250mm from the center. Experiment would be performed by pull-out the column using the actuator to the upward direction. However, the experiment has not yet been carried out due to the delay of test specimens production schedule and laboratory schedule.

Results

Comparison of Flexural and Punching Shear Strength

Flexural Strength

Typically, failure mode of a flat plate system is determined by the lesser of the flexural strength and the punching shear strength. Therefore, prior to the experiment, the flexural strength and the punching shear strength were predicted for each specimen.

The flexural strengths were predicted by using the most commonly used yield line analysis. According to the yield line analysis which is based on limit analysis and concrete plasticity, flexural strength is determined by the formation of yield line satisfying compatibility condition. The shape of yield line depends on the support conditions. As Koppitz et al.18) have well organized the form of yield line for the various support conditions, the results were directly used in this study as shown in Fig 3.

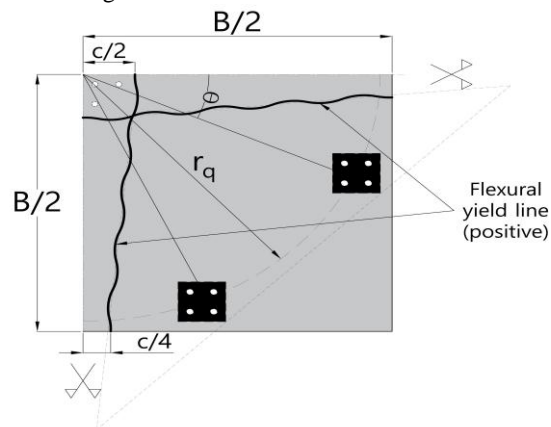


Figure 3: Flexural yield line of a quarter of a test specimen

To the next, the flexural strength can be calculated by the following equation (1) ~ (5). To simply calculate the flexural strength, similar approach as for RC section were also adopted to calculating the contribution of UHPFRC matrix and steel rebars embedded in UHPFRC. In this approach, all the rebars in tension side are assumed to yield. And UHPFRC matrix is assumed to reach the tensile strength, f_{Utu} , thus, the contribution of the UHPFRC matrix to the strength is calculated assuming that the average value of f_{Utu} and f_{Ute} is developed in the cross section. Fig 4 shows the section, and strain and stress distribution of the section of the test specimens to be analyzed. Some important symbols are schematically presented in Fig 4 as well.

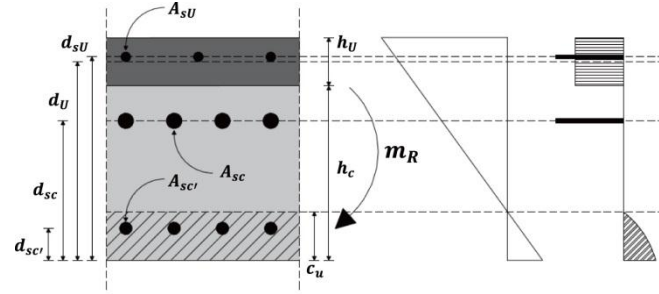


Figure 4: UHPFRC-RC composite section(left) and strain, stress distributions(right)

$$V_{flex} = \frac{4m_{R,total}}{B-c} \cdot \frac{B^2 - Bc - \frac{c^2}{4}}{r_q(\cos\theta + \sin\theta) - c} \quad (1)$$

$$m_{R,total} = m_{R,sc} + m_{R,sU} + m_{R,U} \quad (2)$$

$$m_{R,sc} = \rho_{sc} \cdot f_{y,sc} \cdot d_{sc}^2 \cdot \left(1 - \frac{\rho_{sc} f_{y,sc}}{2f'_c}\right) \quad (3)$$

$$m_{R,sU} = \rho_{sU} \cdot f_{y,sU} \cdot d_{sU}^2 \cdot \left(1 - \frac{\rho_{sU} f_{y,sU}}{2f'_c}\right) \quad (4)$$

$$m_{R,U} = \rho_U \cdot f_{Uta} \cdot d_U^2 \cdot \left(1 - \frac{\rho_U f_{Uta}}{2f'_c}\right) \quad (5)$$

Where,

V_{flex} = Calculated flexural strength

$m_{R,total}$ = Total unit flexural strength of section

$m_{R,sc}$ = Unit flexural strength of RC section

$m_{R,sU}$ = Unit flexural strength of steel embedded
in UHPFRC

$m_{R,U}$ = Unit flexural strength of UHPFRC

As presented in the above equations from (1) to (5), the total flexural strength can be obtained by simply adding the contribution of RC section, UHPFRC matrix and steel rebars in UHPFRC to the flexural strength.

Punching Shear Strength

Contribution of RC Substrate

The contribution of RC substrate to the punching shear strength can be calculated by adopting the Critical Shear Crack Theory (CSCT) proposed by Muttoni.⁷⁾ This theory has been applied to members without transverse reinforcement by adopting the hypothesis that a single critical shear crack localizes the strains in the critical shear region, which is directly related to the rotation (ψ) of the members.⁸⁾ According to the CSCT, the punching shear

strength is determined by the strength at the intersection of load-rotation curve (demand curve) and failure criterion curve (capacity curve). The load-rotation curve is based on multi-linear (or quadri-linear) moment-curvature(M- ψ) relationship of members, and the failure criterion curve is based on shear transfer by aggregate interlocking. Fig 5 graphically shows algorithm for determining the ultimate punching shear strength using CSCT. The meaning of indicators presented in the algorithm is described in detail in Muttoni,7) and Guandalini et al.16)

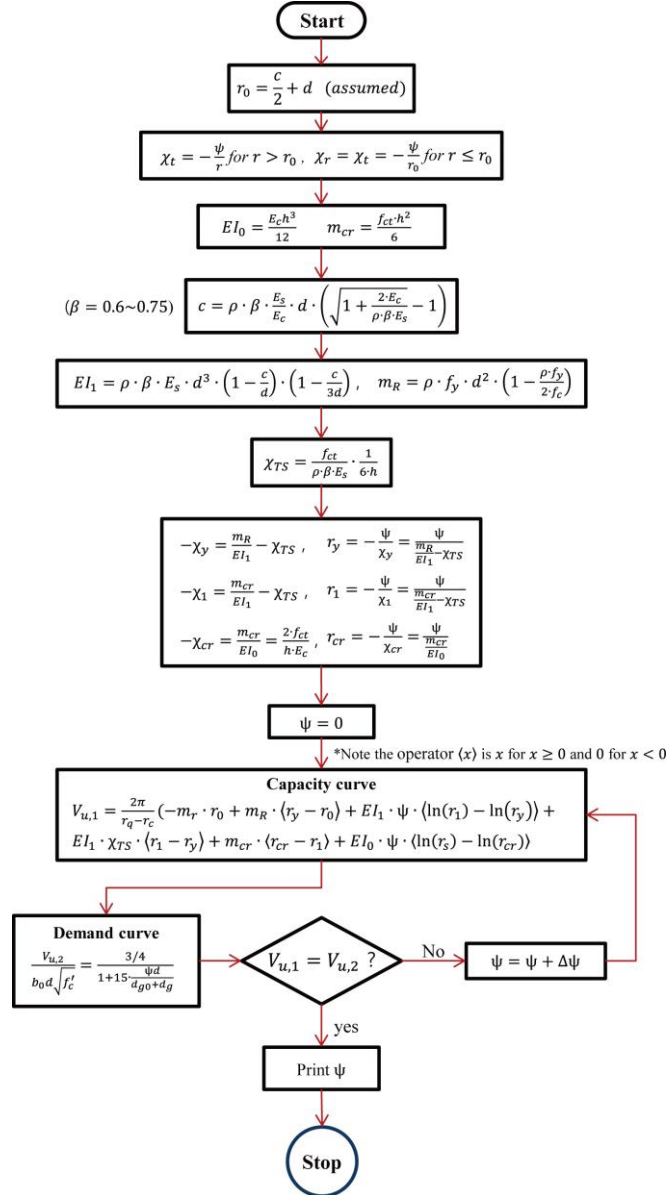


Figure 5: Schematic algorithm for CSCT

Contribution of UHPFRC Overlay

According to Bastien-Masse et al., the contribution of the UHPFRC overlay to the punching shear strength can be estimated from the tensile strength of the RC substrate. This is because the maximum flexural capacity of UHPFRC overlay is generally much greater than the bending moment resistance developed by the tensile strength of the concrete acting at bottom of the concrete cover. It can be also assumed that the interface debonding between the UHPFRC overlay and RC substrate does not occur until the specimen reaches the ultimate punching shear strength.

Governing Failure Mode

The expected governing failure mode is decided by the lesser of the flexural strength calculated by using the yield line theory and the punching shear strength. For all cases, the punching shear strengths are lower than the flexural strengths. In conclusion, the governing failure mode is considered to be the punching shear failure.

Discussion & Conclusions

In this study, a plan for an experiment is carried out to evaluate the punching shear performance of RC flat plate-column connection with UHPFRC overlay. The experimental parameters are the thickness of UHPFRC overlay and the steel rebar ratio placed inside the UHPFRC overlay. The conclusions of this study are as follows.

- A thin layer of UHPFRC on the RC flat plate system can be casted directly on the existing concrete surface without any mechanical shear connectors or bonding materials when the surface are sandblasted.
- Placing UHPFRC with or without steel reinforcement on RC flat plate-column connection is expected to drastically increase not only the punching shear strength but also the bending resistance of existing RC members.

References

- [1]. Korea Concrete Institute. (2012). *Design recommendations for ultra-high performance concrete K-UHPC*. Seoul, South Korea: KCI-M-12-003
- [2]. AFGC. (2013). *Ultra high performance fiber-reinforced concretes – Recommendations*. Paris, France :Association Française de Génie Civil.
- [3]. ACI Committee 318. (2015). *Building code requirements for structural concrete (ACI 318M-14) and commentary*. Retrieved from <https://www.concrete.org/store/productdetail.aspx?ItemID=31814>
- [4]. Korea Concrete Institute. (2012). *Concrete design code and commentary* (pp. 201-203). Seoul, South Korea: Kimoonang Publishing Company.
- [5]. FIB. (2010). *Model code 2010 final draft – volumes 1 and 2, fib bulletin 55 and 66*. Lausanne, Switzerland: Fédération Internationale du béton (fib).
- [6]. European Committee for Standardization. (2002). *EC 2, Design of concrete structures part 1: Code of practice for design and construction*, Brussels, Belgium.
- [7]. Muttoni, A. (2008). Punching Shear Strength of Reinforced Concrete Slabs without Transverse Reinforcement. *ACI Structural Journal*, 105(4), 440-450.
- [8]. Ruiz, M. F., & Muttoni, A. (2009). Applications of critical shear crack theory to punching of reinforced concrete slabs with transverse reinforcement. *ACI Structural Journal*, 106(4), 485.
- [9]. Noshirvani, T., & Brühwiler, E. (2013). Experimental investigation on reinforced ultra-high-performance fiber-reinforced concrete composite beams subjected to combined bending and shear. *ACI Structural Journal*, 110(2), 251.
- [10]. Bastien-Masse, M., & Brühwiler, E. (2016). Composite model for predicting the punching resistance of R-UHPFRC-RC composite slabs. *Engineering Structures*, 117, 603-616.
- [11]. Bastien-Masse, M., & Brühwiler, E. (2016). Experimental investigation on punching resistance of R-UHPFRC-RC composite slabs. *Materials and Structures*, 49(5), 1573-1590.
- [12]. Habel, K., Denarié, E., & Brühwiler, E. (2007). Experimental investigation of composite ultra-high-performance fiber-reinforced concrete and conventional concrete members. *ACI Structural Journal*, 104(1), 93.
- [13]. Koppitz, R., Kenel, A., & Keller, T. (2013). Punching shear of RC flat slabs—Review of analytical models for new and strengthening of existing slabs. *Engineering Structures*, 52, 123-130.
- [14]. Koppitz, R., Kenel, A., & Keller, T. (2013). Punching shear of RC flat slabs—Review of analytical models for new and strengthening of existing slabs. *Engineering Structures*, 52, 123-130.
- [15]. Tayeh, B. A., Bakar, B. A., & Johari, M. M. (2013). Characterization of the interfacial bond between old concrete substrate and ultra high performance fiber concrete repair composite. *Materials and structures*, 46(5), 743-753.
- [16]. Guandalini, S., Burdet, O. L., & Muttoni, A. (2009). Punching tests of slabs with low reinforcement ratios. *ACI Structural Journal*, 106(1), 87.
- [17]. Habel, K., Denarié, E., & Brühwiler, E. (2006). Structural response of elements combining ultrahigh-performance fiber-reinforced concretes and reinforced concrete. *Journal of Structural Engineering*, 132(11), 1793-1800.
- [18]. Koppitz, R., Kenel, A., & Keller, T. (2014). Effect of punching shear on load-deformation behavior of flat slabs. *Engineering Structures*, 80, 444-457.
- [19]. Lim, W. Y., & Hong, S. G., (2016) Slant shear test for determining the interfacial shear strength of concrete strengthened with ultra-high performance fiber-reinforced concrete, *Journal of the Korea Concrete Institute*, 28(6), 637-646.

ECBA-17**RC Column Retrofit with Ultra High Performance Concrete**

In Yeong Koo*

Seoul National University, South Korea

Abstract

Ultra-High Performance Concrete is a cementitious material that has a much higher compressive strength than normal concrete and also has a worthwhile tensional strength to some degree. There had been studies and experiments which tried to apply this material in strengthening or retrofitting structural elements such as beams, slabs or columns. This study particularly focuses on strengthening RC columns with ultra-high performance fiber reinforced concrete (UHPFRC) jacket. For this study, four identical column specimens were manufactured in half scale size (300×300mm). Among four columns, one was chosen as a control specimen and the rest were retrofitted with UHPFRC Jacket using thickness and stirrup as variants. Before retrofitting, surface treatment with sand blasting was applied to get integrated behavior between subjected columns and UHPFRC jackets. The result shows that UHPFRC could be a good alternative for column strengthening method, especially in enhancement of shear capacity.

© 2017 The Authors. Published by Academic Fora. This is an open access article under the CC BY-NC-ND license (<http://creativecommons.org/licenses/by-nc-nd/4.0/>)

Peer-review under responsibility of the Scientific & Review committee of ECBA- 2017.

Keywords— Ultra-High Performance Concrete(UHPC), Column, Retrofit

Introduction

Domestic seismic design criteria of Korea was first introduced in 1988, and most of the structures built before that do not satisfy the seismic design criteria. Structural members of these buildings are considered to have weak seismic performance due to the wide spacing of the stirrup reinforcements and use of 90° hooks.

There are three widely used techniques for retrofitting RC columns; Reinforced concrete jacketing, FRP wrapping, steel jacketing. Concrete jacketing method can increase overall structural capacities such as axial load capacity, shear strength, flexural strength and also deformation capacity. However, it requires jacket thickness higher than 70-100mm, leading to decrease architectural area while increasing total mass of structure. On the other hand, FRP wrapping and steel jacketing have advantages over concrete jacketing method such as much less thickness, lower weight and better constructability. However, strengthening performances are only limited to shear strength and deformation capacity. Axial load capacity can be increased by confinement effect, but is limited to some degree. Besides, durability matters like fire or corrosion resistance should come into consideration when applying these methods.

Recently, a new retrofit technique using UHPFRC jacket to complement the weak points of existing method has been researched and applied. UHPFRC is an ultra-high performance fiber reinforced concrete of which compressive strength can reach over 180MPa and tensile strength over 10MPa by included fiber. This high strength can make it possible to exhibit higher strengthening effect than using normal concrete jacket. Also, due to high fluidity of UHPFRC, jacket thickness can reduce less than 30~50mm, thus, minimize the main disadvantage of normal concrete jacketing method. There are other advantages of UHPFRC retrofit such as high durability, good adjustability with various situations.

Experimental Program

This experiment focuses on shear strengthening performance of UHPC jacket. For this purpose, column specimens were planned in double curvature. Among some factors for estimating seismic retrofit performances, this research and the experiments mainly concentrated to estimate strengthening lateral load resistance performance of UHPC jacket. Jacket thickness and additional stirrup reinforcement insert were planned as variables.

*All correspondence related to this article should be directed to In Yeong Koo, Seoul National University, Korea
Email: berksmile@naver.com

© 2017 The Authors. Published by Academic Fora. This is an open access article under the CC BY-NC-ND license

(<http://creativecommons.org/licenses/by-nc-nd/4.0/>)

Peer-review under responsibility of the Scientific & Review committee of ECBA-2017.

The dimensions adopted for the column cross section and height were 300×300mm and 1260mm, respectively. The longitudinal reinforcement consisted of eight 22mm diameter bars. These relatively small span to depth ratio and large reinforcement ratio were intended to make a shear failure mode both in before and after retrofitting. The transverse reinforcement comprised of 10mm diameter stirrups with 150mm spacing. The column has 500×500mm foundations at both upper and lower stubs to have double curvature experiment. Detail geometries and material properties of the RC column are described in **Error! Reference source not found.** and **Error! Reference source not found.**

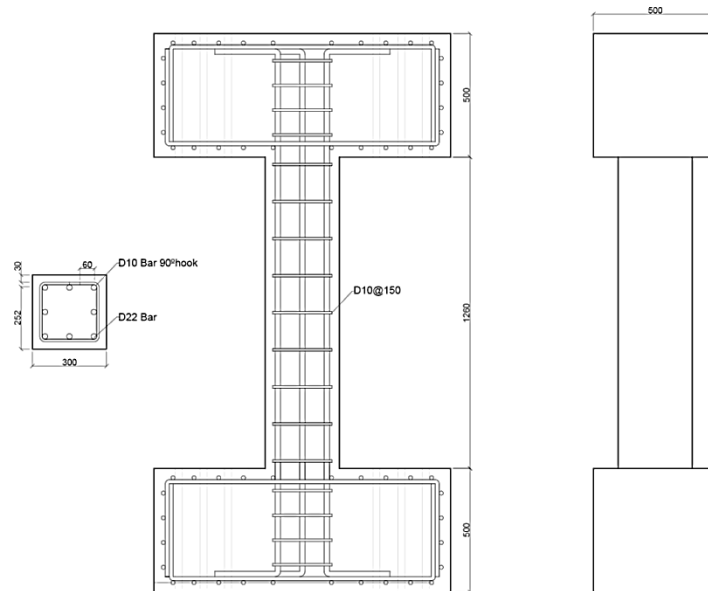


Figure 1: Geometry of RC column

Table 1:

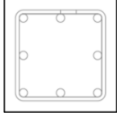
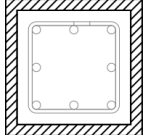
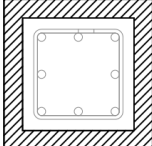
Properties of Retrofitting Target

Column Geometry	section	300mm× 300mm
	Height, h	1260mm
Longitudinal reinforcement		8 × HD22
Transverse reinforcement		HD10@150mm
Nominal Strength	Concrete	24 MPa
	Reinforcement	400 MPa (SS400)

Three RC columns were retrofitted in different ways. The jacket thickness was chosen as a main variable. R-0 remained unretrofitted as a reference specimen. R-30 and R-50 were retrofitted by 30mm and 50mm UHPC jacket, respectively. 30mm was chosen as it is 10% of the column width. 50mm was chosen, because this thickness was thought as the minimum thickness that could afford additional reinforcement in jackets. The details of the three specimens are summarized in Table 1

Table 1:

Test variables and Detail

	R-0	R-30	R-50
Retrofit Method	Reference	30mm jacket (10% thickness)	50mm jacket (16.7% thickness)
Section			

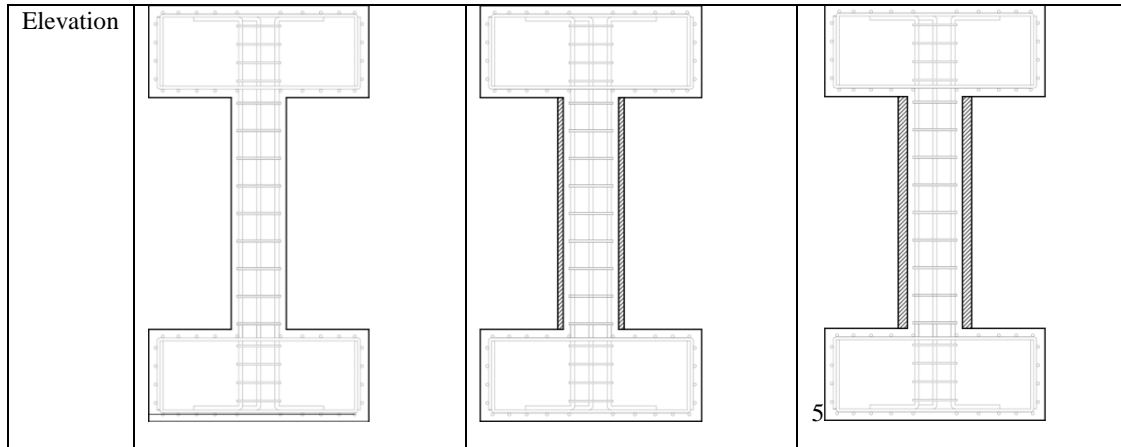


Figure 2: Test set-up

Test Results and Discussion

The load-displacement curves of four test results and crack patterns are presented in Fig. 4 and in Fig. 5 respectively. In specimen R0, initial cracks appeared as flexural crack around both end when the drift ratio was 0.46% and thereafter, cracks propagated in flexural shear crack patterns. However, as the drift ratio reached 1.16%, vertical splitting cracks at the locations of longitudinal reinforcements noticeably occurred, leading to sudden strength degradation. From these crack patterns, it is concluded that the column had failed by bond splitting failure between longitudinal reinforcements and cover concrete.

In specimen R3, no cracks had appeared before the large diagonal tension cracks occurred at 1.16% drift ratio. The subsequent loadings made the diagonal crack extend. As the cracks opened more than fiber's pull-out length, the strength drastically degraded leading to shear failure mode.

R5 specimen showed similar behavior with R3 except several things. The longitudinal reinforcement yielded before crack occurred and showed flexural yielding behavior. The first main crack appeared in diagonal tension cracks when the drift ratio was 2.20% and consequently resulted in flexural-shear failure. Unlike R3 specimen, there appeared two diagonal cracks in both directions.

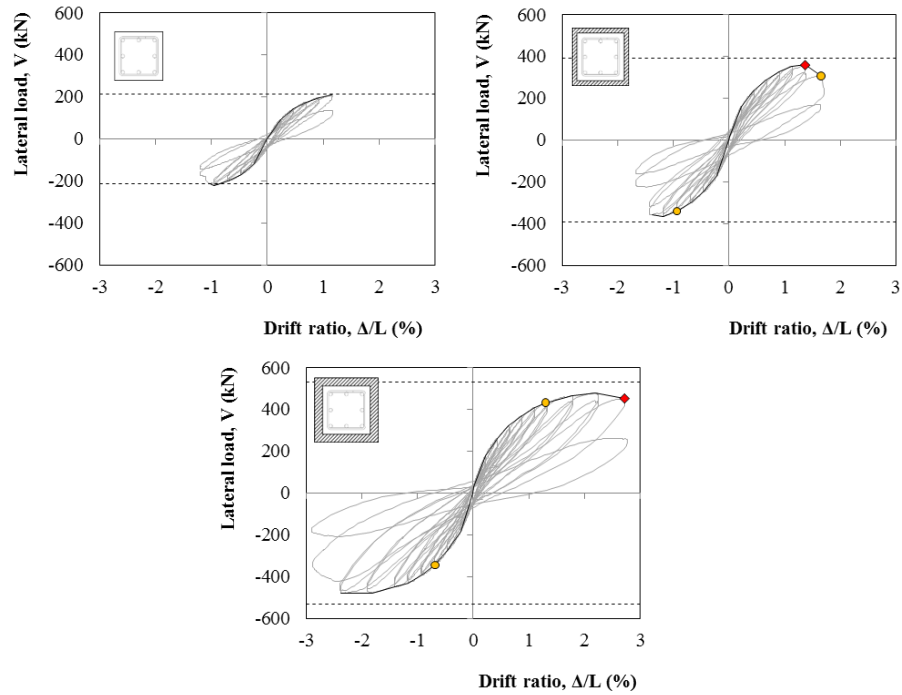


Figure 3: Load-drift curve for each specimen

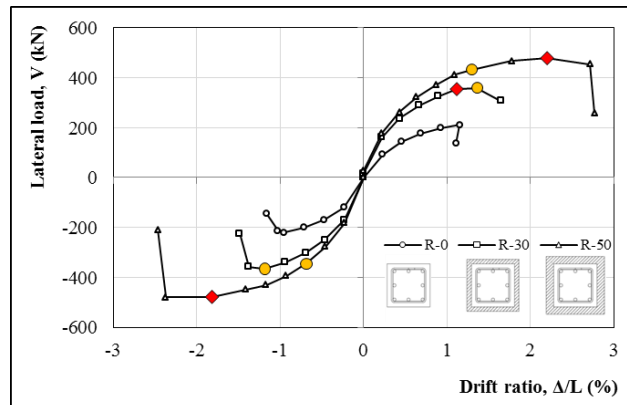


Figure 4: Load-drift curve envelop

Compared with the R-0 specimen, the maximum load capacities of R-30 and R-50 increased about 71% and 128%, respectively. The maximum strain increased about 42% and 134%, respectively. Considering that the column area increased 44% and 78%, the increase in strength was almost proportional to the increase in area. However, the maximum displacement of R-50 was superior to that of R-30. This is because in R-50, the re-bars has reached the yield points and R-30 has been fractured before yielding.

There are two types of diagonal cracks in RC structural members. One is shear compression crack and the other is diagonal tensile crack. Considering that the diagonal cracks in retrofitted specimen (R-30, R-50) start around the center of the column, not the point of load, and the shape of the cracks was far from compressive rupture, this crack is identified as a diagonal tensile crack.

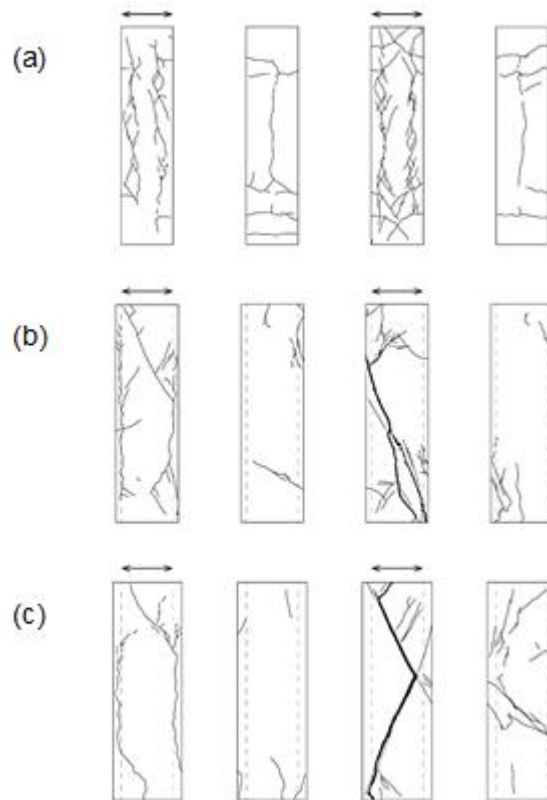


Figure 5: Crack pattern for each specimen (a) R-0 (b) R-30 (c) R-50

Conclusion

In this study, the lateral load resistance capacity of RC column retrofitted with ultra-high performance concrete (UHPC) jacket was estimated through an experiment and theoretical analysis. For interface treatment, only surface roughening process using sandblasting. Additional reinforcement was not applied in order to secure high constructability. This experimental and theoretical research is expected to be used as a reference for suggesting design method of UHPC jacketing for RC column.

The experimental result was analyzed. The lateral load capacities of the retrofitted columns have increased about 70~130% depending on jacket thickness. The columns reached their maximum strength when they got the diagonal tensile crack in the web of the jacket. The columns went to failure soon after crack occurred.

References

- [1]. Meda, A., Mostosi, S., Rinaldi, Z., & Riva, P. (2016). Corroded RC columns repair and strengthening with high performance fiber reinforced concrete jacket. *Materials and Structures*, 49(5), 1967-1978.
- [2]. C. Beschi, A. Meda, and P. Riva, "High Performance Fiber Reinforced Concrete Jacketing in a Seismic Retrofitting Beschi, C., Meda, A., & Riva, P. (2010). High Performance Fiber Reinforced Concrete Jacketing in a Seismic Retrofitting Application. In *Improving the Seismic Performance of Existing Buildings and Other Structures* (pp. 224-233).
- [3]. Minafò, G. (2015). A practical approach for the strength evaluation of RC columns reinforced with RC jackets. *Engineering Structures*, 85, 162-169.
- [4]. Takiguchi, K. (2001). Shear strengthening of reinforced concrete columns using ferrocement jacket. *Structural Journal*, 98(5), 696-704.
- [5]. Meda, A., Plizzari, G. A., Rinaldi, Z., & Martinola, G. (2009). Strengthening of R/C existing columns with high performance fiber reinforced concrete jacket.

ECBA-17**Analysis of the PV Module's Output According to Cloud Moving**Ankhzaya Baatarbileg^{1*}, Su-wan Kim², Gae-myung Lee³^{1, 2, 3} *Department of Electrical Engineering, Jeju National University, S. Korea*

Abstract

Renewablesources such as solar and windare becoming important energiesfor electric power generation. Frequently varying output of a photovoltaic(PV) plant is caused by passing clouds and weather conditions. The power output of a PVplant could be significantly influenced when cloud pass over the plant and temporarily block the incoming radiation from the sun. Variance of solar irradiation is the main cause of fluctuation of photovoltaic power. Further, fluctuations of the power fed to the electric grid can break its power balance and degrade quality of electric energy.This paper presents the simulations of the distributed equivalentcircuitof a PV module under partial shading condition according to cloud passing. The equivalent circuit is modeled from one-diode element and its simulation is implemented by using in LTspice IV program. The influences of different grades of shading on the current-voltage characteristics and the power output of the module are investigated. Also, different possible configurations of bypass diodes are evaluated. Finally, a time-dependent model of a PV module is constructed to simulate the modules' behavior when a cloud moves across it. The cloud's moving direction is also taken into consideration. It is observed that the choice of bypass diode configuration has a strong influence on the performance of a PV module under cloud moving and dynamic shading conditions.

© 2017 The Authors. Published by Academic Fora. This is an open access article under the CC BY-NC-ND license
(<http://creativecommons.org/licenses/by-nc-nd/4.0/>)

Peer-review under responsibility of the Scientific & Review committee of ECBA- 2017.

Keywords— Photovoltaic(PV) Plant, Cloud Moving Shadow, Circuit Model

Introduction

The evolution of renewable energy over the past decade surpassedall expectations. Power capacity of globally installed electric power plants using renewable energies has been increasingand the policies promoting utilization of renewable energies have continued to spread to morecountries in all regions of the world.Among various renewable energy sources, solar energy has gained more popularity than others because of its simple installations at low-voltage levels and the lowprice of PV module. However, the disadvantages of PV system is that its output (current, voltage and power) much relies on solar irradiation and cloud conditions.

PV cells are direct current (DC) generators. Their voltage level depends on the intrinsic cell characteristics,the number of cascaded cells and their temperature. And the available current depends on cellcharacteristics, the number of parallel strings (a string is a group of cascaded cells) and sunlight intensity[1].When one of the cells is partially shadowed, it will produce less current than the rest of the cells in the string.The other cells will try to push more current through the poorcell than it delivers.Another case, when cloud moving over the PV plants occurs, power output of the PV plant can be drop within a few seconds and during a few hours due to cloud size, cloud thickness and wind speed. These are main cause by whichthe power of the PV plant fluctuates. Furthermore, variance of the power is impact to stability, power balance of the grid and quality of electric energy.To reduce losses due topartial shadingby cloud moving, bypass diodes are typically used. However,the module behavior will then be more complex because thebypass diode can help save the operation of the unshaded solarcells and introduce another power peak in the lower voltagerregion under partial shading.

In this paper, the equivalent circuit of a single-diode model in PV cell is simulated by using in LTspice IV program. Thenthe electrical circuit of a PV model with bypass diode is built and power-voltage characteristicsand power output-timecharacteristicsare investigated underadistinct condition of cloud passing. The simulation for the models is implemented in case of cloud moving in two directions.

*All correspondence related to this article should be directed to Ankhzaya Baatarbileg, Jeju National University, Korea

Email: ankhzaya.jeju@gmail.com

© 2017 The Authors. Published by Academic Fora. This is an open access article under the CC BY-NC-ND license

(<http://creativecommons.org/licenses/by-nc-nd/4.0/>)

Peer-review under responsibility of the Scientific & Review committee of ECBA-2017.

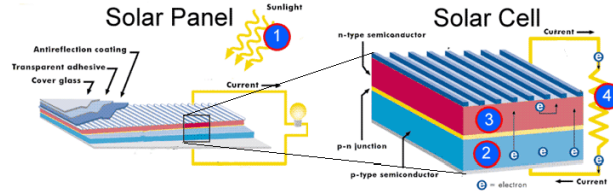


Figure 1: Components of solar panel and cell

Theory and Model of Solar Cell

Photovoltaic Energy

A photovoltaic cell is an electrical device that converts the energy of light into electricity. The photovoltaic effect is a physical and chemical phenomenon. It has suitable metal contacts, usually on the top and bottom, which collect the minority carriers crossing the junction under irradiation and serve as the output terminals [2]. Photovoltaic modules and arrays produce DC electricity. The components of a solar panel and cell are shown at Fig.1.

Single-diode Circuit Model

The single-diode circuit model is widely used and has acceptable result[4].The circuit model with series and shunt resistances,1M5P model (Single Mechanism, Five Parameters), is shown in Fig.2.

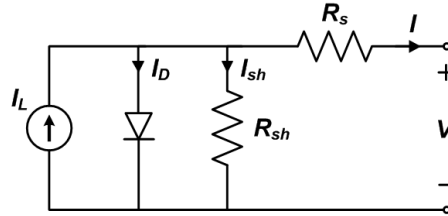


Figure 2: Equivalent circuit of single-diode model

The R_{sh} parallel shunt resistance takes into account the leakage current. The five parameters of this model are: I_L , I_D , n , R_s and R_{sh} .

The output current I through the load is given by equation (1).

$$I = I_L - I_D \left\{ \exp \left[\frac{q \cdot (V + IR_s)}{nkT} \right] - \frac{V + IR_s}{R_{sh}} \right\}, (1)$$

where I_L and I_D are the photocurrent and the inverse saturation current respectively. R_s and R_{sh} are the series and parallel resistance respectively, T and n are the temperature in Kelvin and the diode ideality respectively, k is Boltzmann constant (1.38×10^{-23} J/K) and q is electron charge (1.6×10^{-19} C).

The current I_D through the diode is called inverse saturation current given by equation (2).

$$I_s = \frac{I_{sc} - \frac{V_{oc}}{R_{sh}}}{\exp \left[\frac{q \cdot V_{oc}}{nkT} \right]} \quad (2)$$

where I_s and I_{sc} , V_{oc} are the saturation current, the short circuit current and open voltage of the PV cell respectively.

The light intensity has a dominant effect on current parameters. The short circuit current and the maximum current increase linearly with increasing light intensity. These effects can be calculated by equation (3).

$$I_{sc}(G, T) = I_{sc}(STC) \left\{ 1 + \alpha_{rel} \cdot [T - T(STC)] \right\} \frac{G(G, T)}{G(STC)} \quad (3)$$

where $I_{sc}(G, T)$ and $I_{sc}(STC)$ are the short circuit current of PV cell at certain time and nominal condition of the solar cell, respectively. α_{rel} is the relative current temperature coefficient and $G(G, T)$ and $G(STC)$ are the solar irradiation at certain time and nominal condition of the PV cell, respectively.

And $T(STC)$ is the temperature of the cell at nominal condition.

The open circuit voltage and maximum voltage decrease with increasing the cell temperature, calculated by equation (4)

$$V_{oc}(T) = V_{oc}(STC) \cdot \{1 + \beta_{rel} \cdot [T - T(STC)]\} \quad (4)$$

where $V_{oc}(T)$ and $V_{oc}(STC)$ are the open circuit voltage of PV cell at certain time and at nominal condition, respectively. β_{rel} is the relative voltage temperature coefficient.

Current of PV Cell under Partial Shading and Cloud passing

The cells are connected in series in order to collect higher voltage or in parallel to generate higher current, forming PV modules with the desired output. When one of the cells is partially shadowed, it will produce less current than the rest of the cells in the string. The other cells will try to push more current through the poor cell than it delivers. However that is impossible, since in this case the cell acts as a diode in the reverse direction. Then the current of this cell will limit the current of the whole string. The conventional solution to mitigate shading problem are the bypass diodes. There are some newer solutions for minimizing the impact of shading, as DC-DC optimizers or module inverters.

When cloud moves over the PV module, it will produce less current which is time-dependent. Also shaded area of a cell changes in time, the photocurrent of the cell is calculated by equation (5).

$$I_L = J_L (A_{cell} - A_{shade}(t)) \quad (5)$$

where I_L and J_L are the photocurrent and its density. A_{cell} and $A_{shade}(t)$ are the total area of solar cell and shaded area of solar cell at a certain time, respectively.

Simulation

Simulation of the PV cell

The PV cell selected to do the simulations is the real single-diode model of a solar cell (1M5P). First, we built the equivalent circuit of a PV cell which later used to create the desired PV module and PV array in the LTspice IV program. This software provides a variety of electronic components, such as constant current sources, constant voltage sources, resistors, diodes and capacitors.

In this simulation, all cell parameters were obtained by fitting the single-diode model to the current-voltage characteristics of a real solar cell. The cell parameters are shown in Table I. According to the equations (2), (3) and (4), I_s , I_{sc} and V_{oc} was calculated respectively, for changing of solar irradiance and temperature.

Table 1:
Specifications Of Pv Cell (Stc)

Parameter		Value
$P_{mpp}(W)$	maximum power	4.789
$I_{sc}(A)$	short circuit current	9.398
$V_{oc}(V)$	open circuit voltage	0.640
$I_{mpp}(A)$	maximum power current	8.893
$V_{mpp}(V)$	maximum power voltage	0.538
n	diode ideal factor	1.1
R_s	series resistor	0.005
R_{sh}	parallel resistor	1000
(W x H)	cell dimensions	156 x 156

Simulation of the PV module

The PV module is composed of 60 PV cells connected in series. In the simulation, in cases of the module with three bypass diodes, there are twenty cells under each bypass diode, the module with five bypass diodes, there are twelve cells under each bypass diode in the LTspice IV program. An equivalent circuit of PV module with bypass diodes is shown in Fig.3.

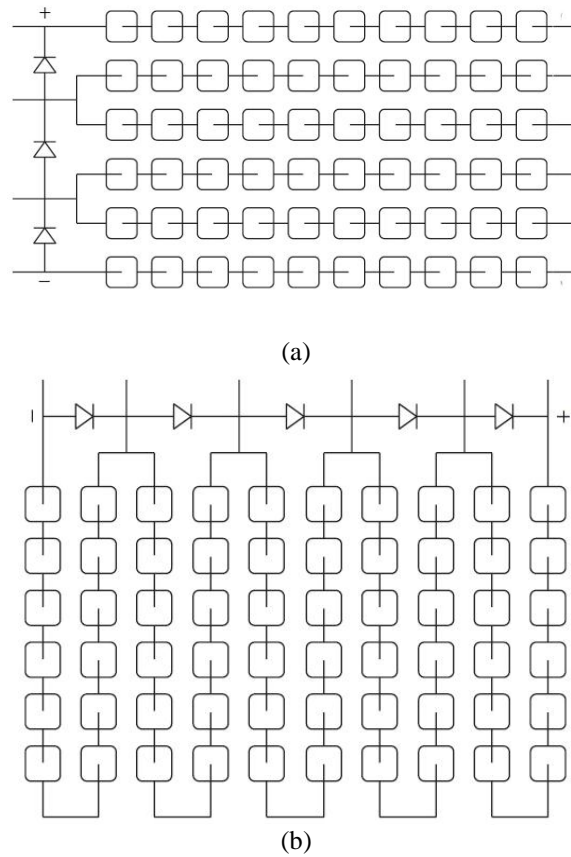


Figure 3: A schematic diagram of PV module (a) with 3 bypass diodes and (b) with 5 bypass diodes

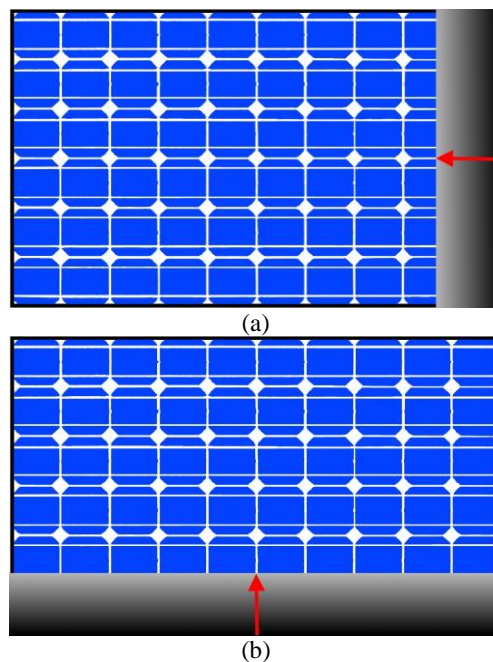


Figure 4: PV module under passing cloud vertically (a) the module with 3 bypass diodes (b) the module with 5 bypass diodes

Simulation cases

In order to investigate P-V characteristics of the presented models, different types of shading cases obtained as explained below.

Case.1: Cloud passing over the PV module to vertical direction

Case.2: Cloud passing over the PV module to horizontal direction

By using equation (5), the relation of photocurrent and time for each solar cell in the module can be obtained and implemented the time-dependent current source in that program. Using this approach, the PV module behavior depending time can be calculated by using a nonlinear transient analysis provided by the LTspice IV software [5]. Above all cases, we assumed that cloud type is thick and when the shaded occurs by cloud, minimum current is 0.93A at every cell in the PV module. We compared between passing two directions are shown in Fig.4(a) and (b). The influence of the cloud moving direction on the PV modules with different bypass diodes configurations was evaluated.

Results and Discussion

Case.1: Cloud passing over the PV module to vertical direction.

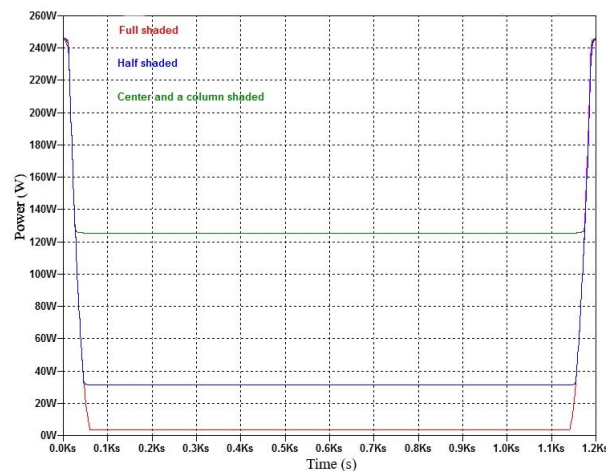
In this Section, a cloud passing to vertical direction over the PV module is taken into consideration. Types of cloud passing over the PV module are full, half, center-two column and edge-a column of the PV module.

We assumed that passing cloud step is one cell per 60 seconds. In the situation of Fig.5(a), the total passing time of the cloud was to be 1200 seconds (first 600 seconds are moving over the module and last 600 seconds are passing away, assuming that there is no space between two adjacent cells and total cloud length is equal to length or width of PV module). In the situation of Fig.5(b), the total passing time was 720 seconds.

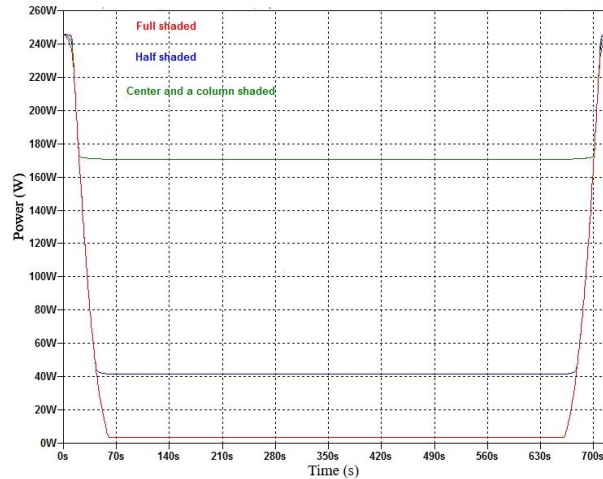
In Fig.5, the results show the relation between time and power output of the PV module with three bypass and five bypass diodes when cloud passing direction is vertical. In Fig.5, the electrical circuit was opened so power output is dropped within at first 60 seconds when the cloud moving over the first cells.

In Fig.5(a), to compare with full, half, center-two column and edge-a column of the PV module shaded by cloud passing, attracting attention is difference of the power output drop of the module. When parts of half, center-two column and edge-a column shaded, unshaded areas remained two columns, four columns and five columns respectively. However, according to bypass diodes configuration, when the center and a column shaded, unshaded area is four columns. The amount of dropped power output of the PV module depends on the number of unshaded columns. Also, the number of connected cells under each bypass diode influences greatly the limits of the power output dropping.

To consider that the module with five bypass diode configuration, when center and a column of the PV module are shaded, the power output is dropped to 170 Watts in Fig.5(b). Because, unshaded area is more than others. Due to the fact that when one cell of a string is completely shaded, the whole string will be inactive.



(a)



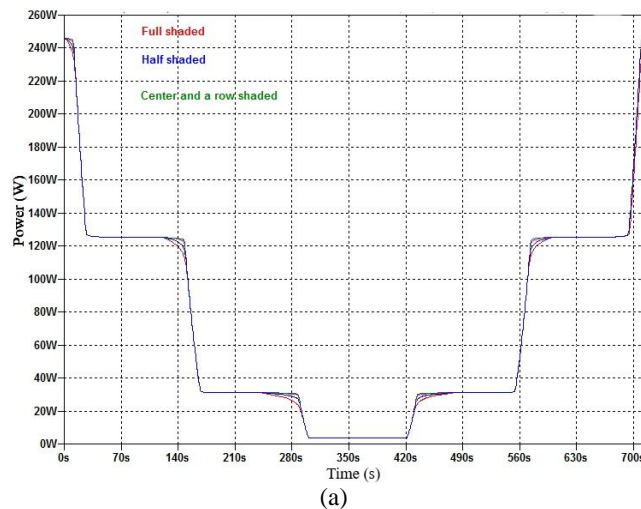
(b)

Figure 5: The relation between time and power output of the PV module in case.1 (a) three bypass diodes; (b) five bypass diodes.

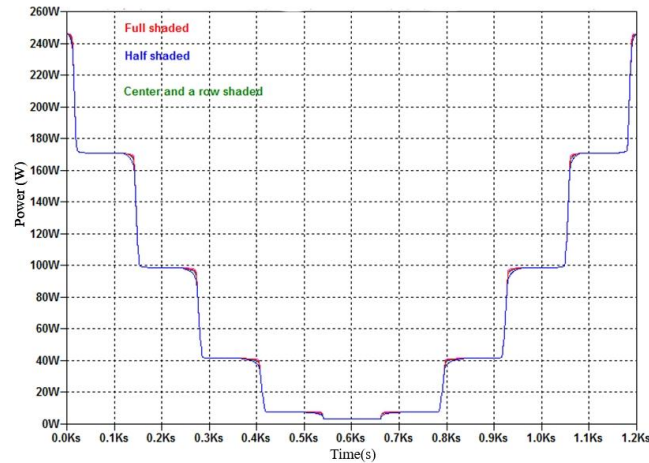
Case.2: Cloud moving over the PV module to horizontal direction.

In this Section, a cloud passing to horizontal direction over the PV module is taken into consideration. The simulation conditions are similar to case.1, but in Fig.6, total cloud passing periods are 720 seconds and 1200 seconds, the modules with three bypass and five bypass diodes respectively. In that case, the power output of the PV module was decreasing by step because bypass diodes take into effect during cloud passing period and help reduce power losses effectively. In Fig.6, in case of cloud passing away PV module, the power output was increasing gradually as shading area decreases. In horizontal direction, all shading types have similar results for the PV modules with both bypass diodes configuration. When the full, half, edge-a row and center-two row shade the PV module, the bypass diodes open sequentially and current flow drops. It is shown in Fig.6.

The investigation shows that, for cloud moving conditions, the choice of bypass configuration can be more important than the number of bypass diodes. It was observed that decreasing and increasing steps of the power output of the PV module depend on the number of cells connected with bypass diodes. Addition, if passing cloud is more larger than the PV module, the bottom period of the lowest power output will increase, which depends on cloud size and passing speed.



(a)



(b)

Figure 6: The relation between time and power output the PV module in case.2(a) three bypass diodes; (b) five bypass diodes.

Conclusions

In this study, the model of a PV module was created to investigate shading effects. Two different possible bypass diode configurations were considered. Also, a time-dependent model was developed and evaluated the performance of a PV module in the two cases of a cloud passing through the module. We found that the configurations of the bypass diodes have a strong influence on the performance of a PV module under cloud moving conditions. The PV modules with more bypass diodes are shown to perform better under the condition that only one string of a module is shaded. However, a certain direction of the cloud passing has a greater influence than the number of bypass diodes used. Also the number of connected cells of a string influenced powerfully the amount of the power output drop of the PV modules. The results of this study can be taken into account in order to generate more electric energy when installing PV modules.

Acknowledgment

This research was financially supported by the Brain Korea-21 (BK-21) project, Ministry of Education, Korea,

References

- [1] Abu-Rub, H., Malinowski, M., & Al-Haddad, K. (2014). *Power electronics for renewable energy systems, transportation and industrial applications*. John Wiley & Sons.
- [2] Messenger, R., & Abtahi, A. (2010). *Photovoltaic systems engineering*. CRC press.
- [3] Silvestre, S., Boronat, A., & Chouder, A. (2009). Study of bypass diodes configuration on PV modules. *Applied Energy*, 86(9), 1632-1640.
- [4] Ramakumar, R., & Bigger, J. E. (1993). Photovoltaic systems. *IEEE Journals & Magazines*, 81(3), 365-377.
- [5] Linear Technology. (n.d.). Design simulation and device models. Retrieved from <http://www.linear.com/designtools/software>

FUTURE EVENTS

You can find the Details regarding our future events by following below:

Business, Economics, Social Science & Humanities (BESSH) Conferences:

<http://academicfora.com/buisness-conference-home/>

Engineering & Technology, Computer, Basic & Applied Science

<http://academicfora.com/engineering-conference-home/>

Medical, Medicine & Health Science

<http://academicfora.com/medical-conference-home/>

For Publication Process please always Contact on:

Publication@academicfora.com

VISION

**“Our vision is to promote research
excellence through networking platform”**

ECBA-2017

Macao, China

**International Conference on
Society for Engineering & Technology,
Computer, Basic & Applied Sciences**

Organized By:



Academic Fora